

Inversion-Based Control Tools for High-Speed Precision Tracking/Transition in Emerging
Applications

by

Haiming Wang

A Dissertation submitted to the
Graduate School-New Brunswick

Rutgers, The State University of New Jersey

in partial fulfillment of the requirements

for the degree of

Doctor of Philosophy

Graduate Program in Mechanical and Aerospace Engineering

written under the direction of

Prof. Qingze Zou

and approved by

New Brunswick, New Jersey

May, 2013

ABSTRACT OF THE DISSERTATION

Inversion-Based Control Tools for High-Speed Precision Tracking/Transition in Emerging
Applications

by HAIMING WANG

Dissertation Director:

Dr. Qingze Zou

This dissertation work is motivated by the challenges in high-speed precision output tracking and transition in emerging applications, particularly for nonminimum-phase systems. On the feedforward control side, the stable inversion theory solved the challenging output tracking problem and achieved exact tracking of a given desired output trajectory for nonminimum-phase systems (linear and nonlinear). The obtained solution, however, is noncausal and requires the entire desired trajectory to be known a priori. This noncausality constraint has been alleviated through the development of the preview-based inversion approach. Therefore, the stable inversion framework provides an effective approach to output tracking of nonminimum-phase systems. Challenges, however, still exist in the existing stable-inversion theory for continuously more stringent control requirements. For example, the control problem of nonperiodic tracking-transition switching with preview for nonminimum-phase systems cannot be satisfactorily addressed by using the existing techniques. Another challenge is that as a feedforward control technique, it can be sensitive to the system dynamics uncertainties. Finally, the demanding on-line computation involved in the preview-based stable-inversion technique hinders the application of this approach in the presence of limited computation power. Therefore, these challenges, as magnified in applications of high-speed nano-manipulation and nano-fabrication, motivate the research work of this dissertation. First, the problem of nonperiodic tracking-transition

switching with preview is considered. In the proposed preview-based optimal output tracking and transition (POOTT) approach, the optimal desired output trajectory for the transition sections is designed, and the needed control input is obtained to maintain the smoothness of system state across all tracking-transition switching instants by using a preview-based stable-inversion approach. The needed preview time is quantified. Secondly, a B-spline-decomposition (BSD)-based approach to output tracking with preview is developed for nonminimum-phase systems, that not only substantially reduces the dynamics uncertainty effect on tracking performance, but also minimizes the online demanding computation. The BSD approach is illustrated through simulation study of a nanomanipulation application using a nonminimum-phase piezo actuator model, and then further demonstrated by a 2D nanomanipulation in experiments using AFM. Finally, a multi-axis inversion-based iterative control (MAIIC) approach is developed to compensate for the dynamics coupling in multi-axis motion during high-speed nanofabrication. By using this advanced control technique, the cross-axis dynamics coupling effect on the output tracking can be compensated for during the iterative learning process. The MAIIC approach is illustrated through probe-based nanofabricate experiments. The research work of this dissertation addresses the limits and further extends the inversion-based control techniques for high-speed precision tracking/transition in emerging applications, particularly, the challenges involved in output tracking with non-periodic tracking-transition switching, accounting for dynamics uncertainty and demanding computation requirements for nonminimum-phase systems, and cross-axis coupling in high-speed multi-axis motion. The experimental part of the work demonstrates and illustrates the efficacy of the proposed control techniques.

DEDICATION

This dissertation is dedicated to my wife Shu Lin, and my parents Jianjun Wang and Huiling Chen, without whose endless trust, support, encouragement, and love it would not have been possible, and to the memory of my grandmother Zuhua Li.

ACKNOWLEDGEMENTS

I would like to thank my advisor, Dr. Qingze Zou, for all of his support, encouragement and guidance throughout my four years graduate study and research. During my Ph.D. program, no matter what I experienced with the successes and failures in my research, Dr. Zou has been always to help, and make me confident. Without his support, encouragement and guidance, I would not complete this dissertation.

Thanks also to my other committee members Dr. Haim Baruh, Dr. Zoran Gajic, and Dr. Jingang Yi for their efforts and contributions to this work.

I also would like to thank my friends and classmates Ying Wu, Kyongsoo Kim, Yan Yan, Zhonghua Xu, Yan Zhang, Zhihua Wang, and Juan Ren. Their support, suggestion, and encouragement help me complete my graduate study.

Finally and utmost, I would like to thank my parents and my wife for all their endless love, great encouragement and unconditional support.

Table of Contents

Abstract	ii
Dedication	iv
Acknowledgements	v
List of Tables	vii
List of Figures	viii
1. Introduction	1
2. Inversion-based Optimal Output Tracking-Transition Switching with Preview for Nonminimum-Phase Linear Systems	6
2.1. Introduction	7
2.2. Problem Formulation: Preview-based Optimal Output Tracking-Transition	10
2.3. Stable-Inversion-Based Solution to the POOTT Problem	14
2.3.1. Output-Tracking Form	15
2.3.2. Design of the Optimal Output Transition Trajectory Within the Preview Window	16
2.3.3. Preview-Based Control Input for the Tracking-Transition Period	19
2.3.4. Optimal Estimation of the Unknown Boundary Value of the Unstable Internal Dynamics	23
2.4. Simulation Example: Nanomanipulation	25
2.4.1. Nonperiodic Output Tracking-Transition Switching with Preview in Nanomanipulation	25

2.4.2.	Output Tracking Form, Internal Dynamics, and Inverse Input	26
2.4.3.	Implementation of the POOTT Technique	27
2.4.4.	Simulation results and discussion	30
2.5.	Conclusions	34
3.	B-Spline-Decomposition-based Output Tracking with Preview for Nonminimum-Phase Linear Systems	36
3.1.	Introduction	37
3.2.	B-spline-Decomposition-Based Approach to Output-Tracking with Preview . .	39
3.2.1.	Problem formulation	40
3.2.2.	Decomposition-Synthesis-Based Output Tracking Approach	40
3.2.3.	B-spline-Based Desired Trajectory Decomposition	45
3.2.4.	Output Elements Extension and Input Elements Approximation	48
3.2.5.	Quantification of the Pre- and Post-Actuation Times	49
3.2.6.	ILC Approach to Construct the Library \mathcal{L}_e	60
3.3.	Nanomanipulation Simulation and Example	61
3.3.1.	Output tracking with preview in nanomanipulation	61
3.3.2.	Implementation of the B-Spline-Decomposition-based Output Tracking . .	62
3.3.3.	Simulation results and discussion	64
3.4.	Conclusions	67
4.	B-spline-Decomposition-Based Approach to Multi-Axis Trajectory Tracking: Nanomanipulation Example	70
4.1.	Introduction	71
4.2.	B-spline-Decomposition-Based Approach to Output Tracking with Preview . .	74
4.2.1.	Decomposition-Synthesis-Based Output Tracking	74
4.2.2.	Quantification of the Pre- and Post-Actuation Times	80
4.3.	Nanomanipulation Experimental Example	82
4.3.1.	Experiment Scheme	83
4.3.2.	Implementation of the Trajectory-Decomposition-Based Output Tracking . .	84

4.3.3. Experimental Tracking Results and Discussion	89
4.4. Conclusions	92
5. High-speed Probe-based Nanofabrication via an Iterative Control Approach for Multi-axis Precision Tracking	99
5.1. Introduction	100
5.2. MAIIC approach to probe-based nanofabrication	102
5.2.1. Cross-axis Coupling Effect on PBN Applications	102
5.2.2. Multi-axis Inversion based Iterative Control (MAIIC) Technique	103
5.2.3. Design of the MAIIC Law	104
5.3. Experimental Example	107
5.3.1. PBN Experiment via Mechanical Scratching	107
5.3.2. SPM Dynamics Modeling and Uncertainty Quantification	108
5.3.3. Experimental Tracking Results and Discussion	111
5.3.4. Nanofabrication Results and Discussion	114
5.4. Conclusions	114
6. Conclusion	120
References	122

List of Tables

- 4.1. Comparison of x -axis output tracking error by using the BSD and the PI feed-back methods, where $E_2(\%)$ and $E_\infty(\%)$ denote the in 2-norm error $E_2(\%)$ and infinity-norm $E_\infty(\%)$ 91
- 4.2. Comparison of X -axis output tracking error by using the BSD and the PI feed-back methods, where $E_2(\%)$ and $E_\infty(\%)$ denote the in 2-norm error $E_2(\%)$ and infinity-norm $E_\infty(\%)$ 91

List of Figures

2.1. The desired output trajectory consisting of tracking sections and transition sections, where the desired output trajectory is prespecified for the tracking sections only.	11
2.2. The frequency response of the piezo actuator mode	26
2.3. Comparison of the desired trajectory for the transition sections obtained by using the LQR technique with different weights.	28
2.4. (a) Comparison of the original command (“Original”) with the shaped command convolved by the input shaper (“Shaped”); and (b) comparison of the system response using the original command and that by using the shaped command, where the insert zooms-in one switching instant.	30
2.5. Comparison of (upper row) the output tracking at relatively low-speed by using (a, c) the proposed approach with (b, d) that by using the input shaping-PI control method, and (lower row) the corresponding tracking errors.	31
2.6. Comparison of (upper row) the output tracking at middle speed by using (a, c) the proposed approach with (b, d) that by using the input shaping-PI control method and (lower row) the corresponding tracking errors.	32
2.7. The output tracking at high speed by using the proposed approach (a) and the corresponding tracking errors (b).	33
2.8. Comparison of (upper row) the output tracking and (upper row) the tracking error obtained by using the optimal boundary POOTT method (“Optimal-Boundary”) with those obtained by using the zero-boundary POOTT method (“Zero-Boundary”) and no-preview for the preview time of (left column) $T_p = 0.08$ ms and (right column) $T_p = 0.15$ ms.	34

2.9.	Comparison of (upper row) the output tracking and (upper row) the tracking error obtained by using the optimal preview inversion method with those obtained by using the preview inversion method with the preview time of (left column) $T_p = 0.3$ ms and (right column) $T_p = 0.8$ ms.	35
3.1.	The proposed control scheme: The red-vertical lines and the big green arrows denote the decomposition instants (i.e., the time instants at which the decomposition–synthesis process occur). At each decomposition instant, the part of the previewed desired output trajectory to be decomposed is marked by the two right ahead adjacent purple-dashed lines, where $\mathbb{T}_{pa,j}$ s for $j = 1, 2, \dots$ denote the corresponding pre-actuation times, and T_p is the preview time. . . .	42
3.2.	The desired output elements in the library \mathcal{L}_e generated by using the 3^{rd} -degree uniform B-spline basis function and its truncated version.	48
3.3.	The pre- and post-actuation time, T_{pa} and T_{pst} for (2) the s^{th} -degree B-spline basis function, (1) the one truncated at the beginning, and (3) the one truncated at the end.	53
3.4.	Desired manipulation contour and previewed X-Y desired trajectories in simulation.	62
3.5.	The decomposition of the previewed desired trajectory by using the 7^{th} -degree uniform B-spline elements, where the pre-actuation time was chosen the same as 3 ms for the total preview time of 4 ms (for the ease of presentation).	64
3.6.	Comparison of (upper row) the y-axis output tracking and (lower row) the tracking error obtained by using the proposed technique with pre-actuation time of (left column) $T_{pa} = 3$ ms, (right column) $T_{pa} = 0.05$ ms. The post-actuation time was the same at $T_{pst} = 1$ ms for $j = 1$ to $j = 6$	65
3.7.	Comparison of (upper row) the y-axis output tracking and (lower row) the tracking error obtained by using the proposed technique with post-actuation time of (left column) $T_{pst} = 1$ ms, (right column) $T_{pst} = 0.05$ ms. The pre-actuation time was the same at $T_{pa} = 3$ ms for $j = 1$ to $j = 6$	66
3.8.	The 2-norm of the tracking error vs. pre-actuation time (left column) and post-actuation time (right column).	67

3.9.	Comparison of the manipulation contour tracking using the proposed technique with (left column) pre-actuation time of (upper row) $T_{pa} = 3$ ms and (lower row) $T_{pa} = 0.05$ ms, and (right column) post-actuation time of (upper row) $T_{pst} = 1$ ms and (lower row) $T_{pst} = 0.05$ ms.	68
3.10.	Comparison of the manipulation contour tracking using the proposed technique with (left column) pre- and post-actuation time $T_{pa} = 3$ ms and $T_{pst} = 1$ ms, and (right column) pre- and post-actuation time $T_{pa} = 0.05$ ms and $T_{pst} = 0.05$ ms.	69
4.1.	The seven ((a) to (g)) output elements generated by using the cubic uniform B-splines.	77
4.2.	The output decomposition in the BSD technique.	79
4.3.	(a) The desired pattern to track in the nanomanipulation experiment, and the corresponding (b) x -axis and (c) y -axis desired trajectory, where the colors and types of the line mark the decomposition instant (beginning point of each line segment) and the portion of the previewed output trajectory to be decomposed at that instant.	84
4.4.	Comparison of the frequency responses of the (a) x -axis and (b) y -axis piezo actuator dynamics and the related coupling dynamics.	85
4.5.	(a, b) Tracking of two of the output elements in the library \mathcal{L}_e and (c, d) the corresponding tracking error.	86
4.6.	The Bode-plot of the x -axis closed-loop feedback control system consisting of the PI-Notch-filter controller.	87
4.7.	The Bode-plot of the y -axis closed-loop feedback control system consisting of the PI-Notch-filter controller.	88
4.8.	Block diagram of the implementation of the BSD technique on a PI-Notch-Filter feedback system.	88
4.9.	x -axis output tracking (a) without and (b) with the PI-Notch filter.	89

4.10. Comparison of the x -axis ($5\ \mu\text{m}$) output tracking results obtained by using the BSD technique with those by using the PI control method at (a1) 1.1 Hz, (a2) 11 Hz, and (a3) 55 Hz, and comparison of the corresponding tracking errors at (b1) 1.1 Hz, (b2) 11Hz, and (b3) 55Hz, respectively.	90
4.11. Comparison of the RU pattern ($5\ \mu\text{m}$) tracking results obtained by using BSD method with those by using the PI control method at (a1) 1.1 Hz, (a2) 11 Hz, and (a3) 55 Hz, and comparison of the corresponding tracking errors at (b1) 1.1 Hz, (b2) 11 Hz, and (b3) 55 Hz, respectively.	94
4.12. Comparison of the x -axis ($80\ \mu\text{m}$) output tracking results obtained by using BSD method with those by using the PI control method at (a1) 1.1 Hz, (a2) 11 Hz, and (a3) 55 Hz, and comparison of the corresponding tracking errors at (b1) 1.1 Hz, (b2) 11 Hz, and (b3) 55 Hz, respectively.	95
4.13. Comparison of the RU pattern ($80\ \mu\text{m}$) tracking results obtained by using BSD method with those by using the PI control method at (a1) 1.1 Hz, (a2) 11 Hz, and (a3) 55 Hz, and comparison of the corresponding tracking errors at (b1) 1.1 Hz, (b2) 11 Hz, and (b3) 55 Hz, respectively.	96
4.14. Comparison of (upper row) the y -axis output tracking and (lower row) the tracking error obtained by using the proposed technique with post-actuation time of (left column) $T_{pst} = 1\ \text{ms}$ and (right column) $T_{pst} = 50\ \text{ms}$	97
4.15. Comparison of (upper row) the pattern tracking and (lower row) the tracking error obtained by using the proposed technique with post-actuation time of (left column) $T_{pst} = 1\ \text{ms}$ and (right column) $T_{pst} = 50\ \text{ms}$	98
5.1. The block diagram of the MAIIC law for the i^{th} -axis output.	105
5.2. The desired trajectories of the Chinese characters pattern: (a) the entire trajectory, (b) the z -axis trajectory, (c) the x -axis trajectory, and (d) the y -axis trajectory.	108
5.3. Comparison of the frequency responses of the x -axis piezo actuator dynamics and the related coupling dynamics.	109

5.4. Comparison of the frequency responses of the y -axis piezo actuator dynamics and the related coupling dynamics.	110
5.5. Comparison of the frequency responses of the z -axis piezo actuator dynamics and the related coupling dynamics.	111
5.6. The upper bounds of the iteration coefficients $\kappa_p(j\omega)$ and the iteration coefficients $\rho_{selected}(j\omega)$ used in the experiments for x -, y - and z -axes, respectively, where the vertical green-dashed line marked the upper bound of the practically tractable set Ω_G	116
5.7. Comparison of the lateral x tracking results obtained by using the MAIIC, MIIC and DC-gain methods with the original desired trajectory at (a) low speed, (b) high speed, and comparison of the corresponding tracking errors at (c) low speed, (d) high speed, respectively.	117
5.8. Comparison of the lateral y tracking results obtained by using the MAIIC, MIIC and DC-gain methods with the original desired trajectory at (a) low speed, (b) high speed, and comparison of the corresponding tracking errors at (c) low speed, (d) high speed, respectively.	117
5.9. Comparison of the vertical z tracking results obtained by using the MAIIC, MIIC and DC-gain methods with the original desired trajectory at (a) low speed, (b) high speed, and comparison of the corresponding tracking errors at (c) low speed, (d) high speed, respectively	118
5.10. Comparison of the nanofabrication images of the Chinese characters pattern obtained by (left column) using the MAIIC technique, by (middle column) using the MIIC method, and with (right column) those obtained by using the DC-gain method at (a1, a2, a3) 0.065 mm/s, (b1, b2, b3) 0.26 mm/s, and (c1, c2, c3) 1.3 mm/s, respectively.	119
5.11. The cross section image of the Chinese characters. The right image shows the depth of the fabricated groove	119

Chapter 1

Introduction

In the last decade, great efforts have been made in precision output tracking of nonminimum-phase systems. Fundamental performance limits to achieving precision output tracking with feedback control technique have been studied and quantified [1, 2]. For minimum-phase systems, exact output tracking of a given desired trajectory is possible. With nonminimum-phase systems, the exact output tracking cannot be achieved by using feedback control alone [1, 2], because the gain of the feedback controller is governed by the nonminimum-phase unstable zero dynamics. On the contrary, exact output tracking can be attained by using the stable-inversion theory [3, 4]. The obtained solution, however, is noncausal—the *unique* stable (bounded) control input (called the inverse input) depends on the entire future desired trajectory, thereby cannot be implemented to applications where the desired trajectory is generated online (e.g., robotics manipulation, or autonomous vehicle guidance). The dependence of the inverse input on the future desired trajectory has been quantified through the development of the preview-based stable-inversion techniques [5, 6, 7, 8]. Such a quantification enables stable-inversion techniques to be implemented to achieve precision output tracking with a quantified large enough preview time. The stable-inversion-based output tracking techniques have been implemented to various applications [5, 6, 9, 10, 11]. Therefore, the stable-inversion framework provides an effective approach to output tracking of nonminimum-phase systems.

Challenges, however, still exist in the stable-inversion theory for practical implementations. For example, the control problem of nonperiodic tracking-transition switching with preview for nonminimum-phase systems has not been considered. Such a control problem arises in many applications, including 2-D spatial mapping of material properties at nanoscale using scanning probe microscope (SPM) [12], track seeking and following in hard-disk drive read/writing

operation [13, 14], probe-based nanomanipulation and nanofabrication [15], and robotics manipulation [16]. In these applications, multiple switching between output tracking and output transition occur, and the control objectives are two folds: (1) During each tracking section, the desired trajectory shall be tracked accurately to meet the specific needs of the application; And (2) during the transition section immediately after, the output shall be rapidly transited, with no induced post oscillations, to the desired position where operation needs to be performed. The tracking-transition switching are, in general, nonperiodic, and in many applications such as nanomanipulation [15] and robotics operations [16], a finite preview of future tracking-transition switching is available for a finite amount of time (i.e., a finite preview).

Another challenge in practical implementation of the stable-inversion approach is that as a feedforward control technique, it can be sensitive to the uncertainties and variations of system dynamics [17, 18]. The sensitivity of the inverse input to the system dynamics uncertainty has been considered previously in [6, 17, 18, 19]. The central idea of [6, 17, 18, 19] is to account for the dynamics uncertainty during the inverse process, thereby trading-off the tracking performance with the precision of the system model (the inverse model, to be specific). The allowable uncertainty for the inverse input to be effective has been quantified in [17], and the trade-off between the tracking precision and the model uncertainty and input energy has been formulated in the LQR optimal control framework in the optimal inversion approach [6, 19], and the minimization of the inverse-based feedforward tracking error against model uncertainty (the worst case) has been considered in the development of the robust inversion approach in [18] for the single input single output (SISO) LTI system. Such a precision-uncertainty trade-off, however, might be avoided in applications where the desired trajectory is known a priori or previewed, provided that the variation of the system dynamics is slow. For example, in AFM systems, the variation of the system dynamics can be ignored during any particular operation, but becomes pronounced in day to day operations (due to, for example, the replacement of AFM cantilever probe). Therefore, for these slow-varying systems, current work on the stable-inversion theory needs to be further developed to achieve precision tracking.

Finally, the online computation involved in the preview-based stable-inversion can be demanding [8, 20, 21, 22]. Particularly, the convolution of the previewed desired output and the internal dynamics of the system need to be computed at each sampling instant. Although efforts

have been made to improve the numerical computation efficiency [20, 21]. The online computation load can be very demanding for high-dimension multi-input multi-output (MIMO) systems. The demanding online computation involved in the preview-based stable-inversion technique hinders the application of this approach with limited computation power. Therefore, efforts are needed to improve the online implementation efficiency of the stable-inversion techniques.

These challenges, as magnified in applications of high-speed nano-manipulation and nanofabrication, motivate the research work of this dissertation.

The rest of this dissertation is organized as follows.

In Chapter 2, an inversion-based approach is developed to achieve optimal tracking-transition switching with preview for nonminimum-phase linear systems. The optimal desired output trajectory for the transition sections is designed by directly minimizing the output energy, and the required control input is obtained by using a preview-based stable-inversion approach. At tracking-transition switching instants, the smoothness of not only output but system state is maintained even though discontinuity of the control input occurs switching. Moreover, the required preview time has been quantified in terms of the stable-inversion theory, and the recently-developed optimal preview-based inversion approach is incorporated to minimize the amount of preview time. The proposed approach is demonstrated by implementing it to a nanomanipulation application using a piezoelectric actuator model in simulation.

In Chapter 3, a B-spline-decomposition (BSD) approach to achieve precision output tracking with preview is proposed. The desired output trajectory is decomposed into a finite summation of desired B-splines basis functions and the corresponding desired input elements achieving precision output tracking are obtained by using iterative control approach, such as the recently-developed multi-axis inversion-based control (MAIIC) approach. Then, the control input is synthesized online by combining the selected input elements together with chosen pre- and post-actuation times. The pre- and post-actuation times of the combined input for given tracking precision is quantified by using the stable-inversion theory. The proposed approach is illustrated through simulation study of a nanomanipulation application using a nonminimum-phase piezo actuator model.

In Chapter 4, the BSD based approach described in Chapter 3 to output tracking with preview is utilized to achieve high-speed and large-range nanomanipulation in experiments. This Chapter demonstrates and evaluates the BSD technique for precision tracking with preview in experiments. The BSD technique avoids the demanding online computation when tracking an online-generated desired trajectory with preview (i.e., the future desired trajectory is known for a finite amount of preview time), by decomposing the previewed desired trajectory with a finite number of output elements based on B-splines, and synthesizing the control input by using the corresponding input elements via the superposition principle. The BSD technique retains the advantages of the ILC approach described above by using the ILC technique to construct a library of pairs of input-output elements *a priori*, while extending the ILC framework to non-repetitive tracking via online decomposition. The stable-inversion theory [3] is utilized to quantify the pre- and post-actuation times [23] involved in the input synthesis. The BSD technique is implemented to track a planar trajectory in 2D nanomanipulation. First, a feedback loop consisting of a proportional-integral (PI) controller followed by a notch filter is employed to account for mainly the drift and hysteresis effects. Then, by applying the BSD technique to the closed-loop system, the experimental results show that the precision of output tracking with preview can be substantially improved over feedback control only, particularly at high-speed. The effect of the finite post-actuation time on the tracking precision has also been studied and demonstrated in the experiment. This chapter demonstrates the efficacy of the BSD technique in high-speed precision tracking of preview in nanopositioning control applications in practices.

Finally in Chapter 5, the recently-developed multi-axis inversion-based iterative control (MAIIC) approach is employed, for the first time in experiments, to achieve probe-based high-speed nanofabrication at large range using AFM. Particularly, the MAIIC technique is utilized to achieve precision tracking of the desired trajectory in all x - y - z axes simultaneously, arriving at precision fabrication of the given pattern at high-speed. By using this advanced control technique, the nonlinear hysteresis and vibrational dynamics effects of the piezotube actuator, as well as the dynamic coupling effect, can be effectively compensated for during the iterative learning process without additional steps to learn the cross-coupling effect separately. The proposed approach is illustrated through experiments by implementing it to fabricate two Chinese

characters pattern via mechanical scratching on a gold-coated silicon sample surface at high speed. The efficacy of the proposed technique is demonstrated through the experimental results that precision tracking in all 3-D axes can be achieved in the presence of pronounced cross-axis dynamics coupling effect.

Our conclusions are presented in Chapter 6.

Chapter 2

Inversion-based Optimal Output Tracking-Transition Switching with Preview for Nonminimum-Phase Linear Systems

Abstract

This chapter considers the problem of nonperiodic tracking-transition switching with preview. Such a control problem exists in applications such as spatial mapping of mechanical property of materials at nanoscale, robot manipulation, and probe-based nanofabrication. In these applications, multiple switching between tracking and transition occur, where the output needs to track desired trajectory during the tracking sections, and rapidly transit to another point during the transition sections with no post-transition oscillations. Due to the coupling between the control of the tracking sections and that of the transition ones, and the potential mismatch of the boundary system state at the tracking-transition switching instants, these control objectives become challenging, particularly for nonminimum-phase systems. In the proposed approach, (1) the optimal desired output trajectory for the transition sections is designed through direct minimization of the output energy, and (2) the needed control input that maintains the smoothness of not only the output, but also the system state across all tracking-transition switching instants is obtained by using a preview-based stable-inversion approach. The needed preview time is quantified in terms of the system dynamics, and the recently-developed optimal preview-based inversion approach is incorporated to minimize the amount of preview time. The proposed approach is illustrated through a nanomanipulation example using a piezoelectrical actuator dynamics model in simulation.

2.1 Introduction

We present an inversion-based optimal control approach to solve the control problem of nonperiodic tracking-transition switching with preview for nonminimum-phase linear systems. Such a control problem arises in many applications, including 2-D spatial mapping of material properties at nanoscale using scanning probe microscope (SPM) [12], track seeking and following in hard-disk drive read/writing operation [13, 14], probe-based nanomanipulation and nanofabrication [15], and robotics manipulation [16]. In these applications, multiple switching between output tracking and output transition occur, and the control objectives are twofold: (1) During each tracking section, to track the desired trajectory accurately to meet the specific needs of the application; And (2) during the transition section immediately after, the output shall be rapidly transited, with no induced post oscillations, to the desired position where operation needs to be performed. The tracking-transition switching are, in general, nonperiodic, and in many applications such as nanomanipulation [15] and robotics operations [16], a finite preview of future tracking-transition switching is available for a finite amount of time (i.e., a finite preview). In this chapter, we propose a stable-inversion approach to achieve the above two control objectives. The proposed approach combines the stable-inversion approach with optimal control technique to maintain the smoothness of not only the output, but also the system state across the tracking-transition switching instants, as well as the output precision throughout the entire tracking-transition switching course.

We note that the development of the stable-inversion theory [3, 4] has solved the challenging problem of exact output tracking for nonminimum-phase systems, and has been extended recently to achieve other control objectives such as minimal-time regulation [24], efficient numerical computation of the stable-inversion [20], and causal feedforward control for static state transition through output trajectory design [25]. The entire desired output trajectory, however, needs to be known *a priori*, and no output transition is allowed. The need of pre-specifying the entire desired trajectory has been alleviated through the development of preview-based stable-inversion technique [5, 6, 7, 8], thereby, online trajectory design/modification is allowed. The desired trajectory, however, needs to be sufficiently smooth, and no output transition is allowed. On the contrary, in the output transition problem, tracking of desired output trajectory outside

the transition period is not addressed in general—only special cases where either the output outside the transition period is constant [24, 25, 26, 27, 28] or the tracking-transition switching is periodic (e.g., as in scanning operation) [29] has been considered. Conventionally, the problem of output transition is converted and solved as a state transition problem—the classical optimal state transition method (OST, e.g., [30]). The solution of OST involves user chosen boundary state values, which tends to be *ad hoc* and thereby not necessarily optimal since usually output boundary value instead of the state one is specified. Such an *ad hoc* choice of the boundary state is avoided in the recently-developed optimal output transition technique (OOT) [26, 29], where the value of the boundary state value is optimized. Smooth output transition can also be achieved by using the input-shaping technique [28, 31, 32, 33]. However, tracking of the desired output trajectory before and after the transition is not addressed, neither is multiple and nonperiodic tracking-transition switching. Therefore, there is a need to study the problem of nonperiodic tracking-transition switching with preview for nonminimum-phase systems.

Challenges exist in the problem of nonperiodic tracking-transition with preview for nonminimum-phase systems. Note that point-to-point output transition with minimal oscillations is needed in many applications. The desired output trajectory obtained from the OST [30] or the OOT [26, 29] techniques, however, can be highly oscillatory when the system dynamics is lightly-damped, because both the OST and OOT techniques are based on the minimization of input energy. As a result, the frequency components of the obtained optimal input tend to concentrate around the resonant peak(s) of the system dynamics, leading to an oscillatory desired output [34]. Although such large output oscillations can be mitigated by modifying the system dynamics with a pre-filter [14, 34], it is desirable to directly minimize the output energy rather than the input energy in the output transition. More importantly, even when such a smooth desired output trajectory across tracking-transition switching is available, smooth tracking of such a desired output trajectory across switching instants may not be achieved, because smoothness of the system state—not just the output—across the switching instances needs to be maintained, whereas the desired system state after switching tends to be unknown. Such a smoothness of system state across switching cannot be archived by using existing approaches such the OST, the OOT, or the input-shaping techniques [26, 29, 31, 32], resulting in mismatch of boundary state across switching and post-switching output oscillations. Particularly when

multiple tracking-transition switching exist and close to each other, the switching-caused oscillations can be amplified and they propagate along the tracking-transition course. Moreover, for nonminimum-phase systems, as pre-actuation is needed to track a given desired output trajectory [3, 20], the control of tracking sections is coupled with that of transition sections, i.e., the control input for each transition section shall not only achieve the required point-to-point transition, but also “prepare” the system state for the output tracking in the tracking section next [3], and vice versa. This transition-tracking coupling becomes challenging, because other than scanning operations [29, 34], usually the tracking-transition switching are nonperiodic, and the system state at the switching instants are unknown. Therefore, nonperiodic tracking-transition switching with preview for nonminimum-phase systems cannot be addressed with existing approaches.

The main contribution of this chapter is the development of an inversion-based approach to achieve optimal tracking-transition switching with preview for nonminimum-phase linear systems. In the proposed approach, the tracking-transition switching problem is transformed to designing the desired output trajectory for the transition sections first, and then obtaining the corresponding control input for the trajectory consisting of both tracking and transition sections. Specifically, the desired output trajectory for the transition sections are designed through a direct minimization of the output energy instead of the input energy. Such an output minimization also guarantees the smoothness of the desired output across the transition-tracking switching instants, up to one order less than the relative degree of the system. Secondly, the required control input is obtained through the preview-based approach. It is shown that at tracking-transition switching instants, smoothness of the entire system state is maintained even though discontinuity of the control input occurs during switching. It is also shown that the tracking error caused by the finite preview can be rendered arbitrarily small by having a large enough preview time, and the preview time to guarantee the tracking precision depends on the system nonminimum-phase characteristics of the dynamics, thereby can be quantified. Finally, the recently-developed optimal preview-based stable-inversion method [8] is incorporated into the proposed approach to reduce the amount of preview time needed for applications where the amount of preview time is stringent [35]. Therefore, the proposed approach extends the stable-inversion theory to the nonperiodic output tracking-transition switching with preview

for nonminimum-phase systems. The proposed approach is illustrated by implementing it to an nanomanipulation application using a piezoelectric actuator model in simulation. The simulation results are compared with that obtained by using the input-shaping [31] along with a PI-feedback control, to illustrate the efficacy of the proposed approach.

The rest of the chapter is organized as follows. In Section 2.2, the preview-based optimal output tracking and transition problem is formulated, followed by the proposed inversion-based solution in Section 2.3. The proposed approach is illustrated through a simulation example in Section 2.4, where simulation results are presented and discussed. Our conclusions are given in Section 2.5.

2.2 Problem Formulation: Preview-based Optimal Output Tracking-Transition

Consider the following square LTI system

$$\dot{x} = Ax + Bu, \quad y = Cx, \quad (2.1)$$

with the same number of inputs and outputs, $u(\cdot), y(\cdot) \in \mathbb{R}^p$, and $x(\cdot) \in \mathbb{R}^n$. We assume that

Assumption 1 *System (2.1) is controllable, observable, hyperbolic (i.e., has no zeros on the imaginary axis), and has a well-defined vector relative degree $r \triangleq [r_1, r_2, \dots, r_p]^T$ [36].*

In the following, without loss of generality, we assign all transition sections \mathbf{T}_k for $k \in \mathbb{N}$ (\mathbb{N} : the set of natural numbers), to be closed (See Fig. 2.1), i.e.,

$$\mathbf{T}_k = [t_{k,i}, t_{k,f}], \quad k \in \mathbb{N}. \quad (2.2)$$

where $t_{k,i}$ and $t_{k,f}$ are defined as the initial instant and the final instant for the k^{th} transition section, respectively. Correspondingly, we assign all tracking sections \mathbf{I}_q for $q \in \mathbb{N}$ to be open, i.e.,

$$\mathbf{I}_q = (t_{q,f}, t_{q+1,i}), \quad q \in \mathbb{N}. \quad (2.3)$$

As schematically depicted in Fig. 2.1, the above assignment implies that the time domain of real numbers, \mathbb{R} , is partitioned into pair-wise disjointed tracking and transition intervals, i.e.,

$$\mathbb{R} = (\cup_q \mathbf{I}_q) \cup (\cup_k \mathbf{T}_k), \quad \text{and} \quad \mathbf{I}_q \cap \mathbf{T}_k = \emptyset, \quad \text{for} \quad \forall q, k \in \mathbb{N}. \quad (2.4)$$

Such a partition of time ensures that the entire trajectory is a well-defined function of time, and is partitioned accordingly into the user-defined desired trajectory for the tracking intervals, $y_{dtr}(\cdot)$, and the to-be-designed output trajectory for the transition intervals, $y_{dtn}(\cdot)$, i.e.,

$$y_d(\cdot) = (\cup_q y_{dtr,q}(\cdot)) \cup (\cup_k y_{dtn,k}(\cdot)), \quad (2.5)$$

where $y_{dtr,q}(\cdot)$ and $y_{dtn,k}(\cdot)$ are defined for the q^{th} tracking interval \mathbf{I}_q and the k^{th} transition interval \mathbf{T}_k , respectively, and $q, k = 1, 2, \dots$. Correspondingly, the control input $u_{ff}(\cdot)$ for the tracking intervals and the transition intervals are denoted as $u_{tr}(\cdot)$ and $u_{tn}(\cdot)$, respectively,

$$u_{ff}(\cdot) = (\cup_q u_{tr,q}(\cdot)) \cup (\cup_k u_{tn,k}(\cdot)), \quad (2.6)$$

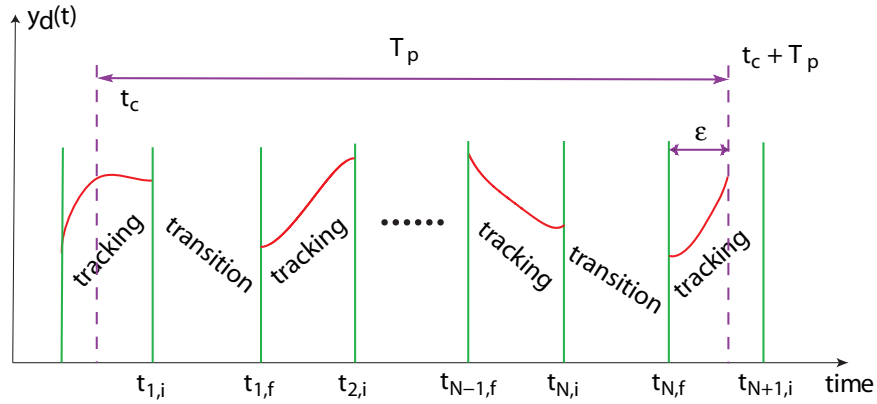


Figure 2.1: The desired output trajectory consisting of tracking sections and transition sections, where the desired output trajectory is prespecified for the tracking sections only.

Moreover, as discontinuity of the output, the input, or the system state may occur at the boundary points, we further denote the left-hand limit as $f(t^-)$, and the right-hand limit of a signal $f(t)$ at time instant t as $f(t^+)$, as given below

$$f(t^-) = \lim_{\Delta t \rightarrow 0} f(t - \Delta t), \quad f(t^+) = \lim_{\Delta t \rightarrow 0} f(t + \Delta t), \quad \text{with } \Delta t > 0. \quad (2.7)$$

Similarly, assume that the function is continuously differentiable till the $(r-1)^{th}$, then the left-hand limit and the right-hand limit of the r^{th} derivative of the signal $f(t)$, $f^{(r)}(t^-)$ and $f^{(r)}(t^+)$, are given by

$$\begin{aligned} \frac{d^{(r)} f(t^-)}{dt^r} &= \lim_{\Delta t \rightarrow 0} \frac{f^{(r-1)}(t) - f^{(r-1)}(t - \Delta t)}{\Delta t}, \\ \frac{d^{(r)} f(t^+)}{dt^r} &= \lim_{\Delta t \rightarrow 0} \frac{f^{(r-1)}(t + \Delta t) - f^{(r-1)}(t)}{\Delta t}, \end{aligned} \quad (2.8)$$

In this chapter, unlike the existing work [28, 26], the entire output transitions are not assumed to be specified/known a priori, neither are all the tracking-transition switching periods. Rather, we consider the more general scenario where the tracking-transition switching are nonperiodic, and there exists a finite preview of future desired tracking-transition switching.

Assumption 2 *The desired output trajectory is piecewisely-smooth enough, i.e., during any given tracking interval, \mathbf{I}_q for $q \in \mathbb{N}$, the desired output trajectory for the m^{th} output channel, $y_{\text{dtr},m}(\cdot)$, is differentiable up to the r_m^{th} order at all the interior points of the interval \mathbf{I}_q . Moreover, the number of output transition in any finite time interval is finite.*

Assumption 3 *At any given time instant t_c , there exists a finite preview time T_p of future desired tracking-transition switching consisting of N number of transitions ($N = 0, 1, 2, \dots$, and $N < \infty$), such that the desired output trajectory after the N^{th} transition is known for any given time duration of $\epsilon > 0$ (See Fig. 2.1).*

Remark 1 *The above assumption essentially is to require, that within the preview time window, the boundary conditions for all tracking-transition switching are well-defined. This assumption is needed to ensure that a nonzero preview time is available at any time instant t_c . Otherwise, if the desired output at the final instant of the N^{th} transition interval, $y_{\text{dtn},N}(t_{N,f})$, is unknown, no desired trajectory, in general, can be found to ensure the smoothness of the desired output trajectory across the N^{th} transition-tracking switching. As a result, the desired trajectory for the N^{th} transition interval becomes un-defined, and the preview time vanishes to zero as the time instant t_c approaches to the N^{th} transition interval (See Fig. 2.1).*

Remark 2 *Note that such a finite preview of future desired tracking-transition switching (in Assumption 3) is available in many applications. For example, in nanomanipulation [15] or robot manipulation [16], if tracking-transition switching occurs during the preview time window, the purpose of the last previewed transition—the initial part of the operation after that transition (which, in turn, implies a finite preview of the desired output trajectory), shall be known—Otherwise the last transition becomes vain.*

Remark 3 *Assumption 3 also implies that there exists an instant increase of preview time (in length) when the final instant of the preview window, $t_c + T_p$, approaches to the initial instant*

of a transition interval, i.e., when $t_c + T_p \rightarrow t_{k,i}$ for some k , the length of preview time is increased by the amount of that transition interval, i.e., $T_p \rightarrow T_p + (t_{k,f} - t_{k,i}) + \epsilon$ for any given $\epsilon > 0$. This instant increase of preview time is not a constraint of the proposed approach but an inherent property of preview in tracking-transition switching operation, (See also Remark 2).

Now we are in the position to formally state the preview-based optimal output tracking and transition (POOTT) problem:

Problem Formulation Let Assumptions 1–3 be satisfied, then the POOTT problem is to (1) design the desired output trajectory for each transition interval, $y_{dtn,k}(t)$ for $t \in \mathbf{T}_k$ and each $k = 1, 2, \dots, N$, and (2) obtain the corresponding feedforward control input $u_{ff}(\cdot)$, such that the following outcome are obtained,

$\mathcal{O}1$ The required output transition is achieved, i.e.,

$$y_{dtr}(t_{k,i}) = y_{dtn}(t_{k,i}), \quad y_{dtn}(t_{k,f}) = y_{dtr}(t_{k,f}), \quad \text{for } k = 1, 2, \dots, N. \quad (2.9)$$

$\mathcal{O}2$ During each transition, the energy of the output along with its derivatives up to the r^{th} order are minimized, i.e.,

$$\min_{y_{dtn}(\cdot)} (T_k) = \min_{y_{dtn}(\cdot)} \int_{t_{k,i}}^{t_{k,f}} (\mathbf{H}_{\mathbb{Y}} \mathbb{Y}_{dtn}(\tau))^T Q (\mathbf{H}_{\mathbb{Y}} \mathbb{Y}_{dtn}(\tau)) d\tau \quad (2.10)$$

where $Q \in \mathbb{R}^{p \times p}$ is a semidefinite positive matrix, $\mathbb{Y}_{dtn}(\cdot)$ is the vector of the desired output trajectory and its derivatives up to the r^{th} order (during the transition intervals),

$$\mathbb{Y}_{dtn}(t) = \left[\xi_{1,dtn}(t)^T, y_{1,dtn}^{(r_1)}(t), \xi_{2,dtn}(t)^T, y_{2,dtn}^{(r_2)}(t), \dots, \xi_{p,dtn}(t)^T, y_{p,dtn}^{(r_p)}(t) \right]^T, \quad \text{with} \quad (2.11)$$

$$\xi_{k,dtn}(t) = \left[y_{k,dtn}(t), \dot{y}_{k,dtn}(t), \dots, \frac{d^{r_k-1} y_{k,dtn}}{dt^{r_k-1}} \right]^T \quad (2.12)$$

and $\mathbf{H}_{\mathbb{Y}} \in \mathbb{R}^{p \times m}$ is a block diagonal matrix with $m = p + \sum_{k=1}^p r_k$,

$$\mathbf{H}_{\mathbb{Y}} = \begin{bmatrix} \mathbf{H}_{Y,1} & \mathbf{0} & \cdots & \mathbf{0} \\ \mathbf{0} & \mathbf{H}_{Y,2} & \cdots & \mathbf{0} \\ \vdots & \vdots & \ddots & \vdots \\ \mathbf{0} & \mathbf{0} & \cdots & \mathbf{H}_{Y,p} \end{bmatrix} \quad (2.13)$$

with $H_{Y,k} \in \mathbb{R}^{1 \times (r_k+1)}$ for $k = 1, 2, \dots, p$ as

$$H_{Y,k} = [H_k \quad 1] \quad (2.14)$$

where

$$[H_k \quad 1] = [-h_{k,1}, -h_{k,2}, \dots, -h_{k,r_k}, 1] \quad (2.15)$$

is the coefficient of a stable polynomial, i.e., the following polynomial $P(s)$

$$P(s) = s^{r_k+1} + h_{k,1}s^{r_k} + \dots + h_{k,r_k-1}s + h_{k,r_k} \quad (2.16)$$

has all its roots on the left open half complex plane.

O3 Provided that there exists an enough (but finite) preview, precision output tracking is maintained throughout the entire output tracking and transition course, i.e., at any time instant t , the error relative to the exact tracking input is within any chosen positive number $\epsilon_i > 0$,

$$\|e_{p,in}(t)\|_2 \triangleq \|u_{inv}(t) - u_p^*(t)\|_2 \leq \epsilon_i, \quad (2.17)$$

where $\|a\|_2$ is the standard vector 2-norm for vector $a \in \mathbb{R}^n$, $u_{inv}(\cdot)$ denotes the input that achieves exact tracking of the desired output trajectory, and $u_p^*(\cdot)$ denotes the input solution to the POOTT problem.

Note that in (2.13) and the rest of the chapter, “ $\mathbf{0}$ ” denotes a zero matrix of an appropriate dimension.

Remark 4 *The polynomial of the desired output and its derivatives in (2.10) allows the user to selectively penalize the energy of the output or its derivatives—through the design of the vectors H_k s. It will become clear immediately later that in the proposed approach, the design of the vectors H_k s under the constraint given by (2.15, 2.16) is utilized to minimize the oscillations of the output during the transition intervals.*

2.3 Stable-Inversion-Based Solution to the POOTT Problem

Next, we present an inversion-based approach to solve the POOTT problem. We start with transforming system (2.1) to the *output-tracking* form.

2.3.1 Output-Tracking Form

Under Assumption 1, there exist (i) a state transformation, $M : \mathbb{R}^n \rightarrow \mathbb{R}^n$ and (ii) an input law to transform system (2.1) into the output-tracking form. The needed state transformation M is given by

$$\begin{bmatrix} \xi(t) \\ \eta_s(t) \\ \eta_u(t) \end{bmatrix} = Mx(t) = \begin{bmatrix} M_\xi \\ M_{\eta,s} \\ M_{\eta,u} \end{bmatrix} x(t), \quad (2.18)$$

where $\xi(t) = M_\xi x(t)$ are the output and its derivatives as in

$$\xi(t) = [\xi_1^T(t), \xi_2^T(t), \dots, \xi_p^T(t)]^T \quad (2.19)$$

with $\xi_k(t)$ being defined in (3.36), and η_s and η_u are the stable and the unstable subspaces of the internal dynamics, respectively, i.e., the eigenvalues corresponding to the eigenvectors that span the subspaces of the state η_s or η_u are all on the left open half complex plane and the right one, respectively. In (2.18), the matrices M_ξ , $M_{\eta,s}$, and $M_{\eta,u}$ are partitioned according to the rows of the output vector ξ , the stable internal dynamics η_s , and the unstable internal dynamics η_u , respectively. The input needed for the transformation in (2.18), in general, can be represented as

$$\begin{aligned} u_{inv}(t) &= \mathbf{M}_\xi \xi(t) + \mathbf{M}_r y^{(r)}(t) + \mathbf{M}_s \eta_s(t) + \mathbf{M}_u \eta_u(t), \\ &= \mathbf{M}_Y \mathbb{Y}(t) + \mathbf{M}_s \eta_s(t) + \mathbf{M}_u \eta_u(t) \end{aligned} \quad (2.20)$$

where $\mathbb{Y}(\cdot)$ is as defined in (2.11). The above input is called the *inverse input*, as it determines the desired input for desired output trajectory (i.e., when $\mathbb{Y}(\cdot) = \mathbb{Y}_d(\cdot)$). The readers are referred to [5, 8] for the expressions of the Matrices \mathbf{M}_Y , \mathbf{M}_s , \mathbf{M}_u in (2.20). By using the stable-inversion theory, it can be shown [3] that for square systems under Assumptions 1, 2, the bounded solution to the unstable internal dynamics $\eta_u(\cdot)$ is uniquely determined, so is the inverse input by (2.20).

Using the state transformation (2.18) and the inverse input (2.20), system (2.1) is transformed to the following output tracking form

$$\begin{aligned} \dot{\xi}(t) &= \bar{\mathbf{I}}_{up} \xi(t) + \mathbf{B}_\xi y^{(r)}(t) \\ \dot{\eta}_s(t) &= A_s \eta_s(t) + B_s \mathbb{Y}(t) \\ \dot{\eta}_u(t) &= A_u \eta_u(t) + B_u \mathbb{Y}(t) \end{aligned} \quad (2.21)$$

where

$$\bar{\mathbf{I}}_{up} = \begin{bmatrix} \mathbf{I}_{up,1} & \mathbf{0} & \cdots & \mathbf{0} \\ \mathbf{0} & \mathbf{I}_{up,2} & \cdots & \mathbf{0} \\ \vdots & \vdots & \ddots & \vdots \\ \mathbf{0} & \mathbf{0} & \cdots & \mathbf{I}_{up,p} \end{bmatrix}, \mathbf{B}_\xi = \begin{bmatrix} B_{\xi,1} & \mathbf{0} & \cdots & \mathbf{0} \\ \mathbf{0} & B_{\xi,2} & \cdots & \mathbf{0} \\ \vdots & \vdots & \ddots & \vdots \\ \mathbf{0} & \mathbf{0} & \cdots & B_{\xi,p} \end{bmatrix}$$

$$\mathbf{I}_{up,k} = \begin{bmatrix} \mathbf{0} & E_k \\ \mathbf{0} & \end{bmatrix}_{r_k \times r_k}, \quad B_{\xi,k} = \begin{bmatrix} \mathbf{0} \\ 1 \end{bmatrix}_{r_k \times 1} \quad (2.22)$$

where E_k denotes the identity matrix of dimension $k \times k$, and the eigenvectors of A_s and A_u span the stable and the unstable subspaces of the internal dynamics, respectively. Note that in the output tracking form (2.21), the output and its derivatives ξ is considered as one part of the state.

2.3.2 Design of the Optimal Output Transition Trajectory Within the Preview Window

The output tracking form (2.21) reveals that the r^{th} derivative of the output acts as the input to the transformed system dynamics with the output and its (lower than r^{th} order) derivatives constitute one part of the system state. Thus, the optimal output design problem (2.10) can be rendered as an optimal input design problem. Specifically, we design the desired output transition trajectory through the stabilization of the output subdynamics, followed by the input energy minimization to the stabilized output subdynamics.

The output subdynamics (2.21) is stabilized by using a static state-feedback control, i.e., by using the following static state feedback gain H_ξ ,

$$y^{(r)}(t) = H_\xi \xi(t) + \gamma(t), \quad (2.23)$$

the following output subdynamics becomes exponentially stable,

$$\begin{aligned} \dot{\xi}(t) &= (\mathbf{I}_{up} + \mathbf{B}_\xi H_\xi) \xi(t) + \mathbf{B}_\xi \gamma(t) \\ &\triangleq \hat{A}_\xi \xi(t) + \mathbf{B}_\xi \gamma(t). \end{aligned} \quad (2.24)$$

Note that by (2.22–2.24), it can be verified that after the stabilization, the stabilized subdynamics related to each output y_k is in the controllable canonical form, i.e.,

$$\dot{\xi}_k(t) = \hat{A}_{\xi,k} \xi_i(t) + B_{\xi,k} \gamma_k(t) \quad (2.25)$$

where

$$\hat{A}_{\xi,k} = \begin{bmatrix} \mathbf{0} & E_{k-1} \\ H_{\xi,k} & \end{bmatrix} \quad (2.26)$$

Thus, the row vector $H_{\xi,k}$ corresponds to the characteristic polymer for the subdynamics $\{\hat{A}_{\xi,k}, B_{\xi,k}\}$. Particularly, due to the decoupling of the output subdynamics in each the output channels, each state feedback vector $H_{\xi,k}$ can be designed separately to determine the poles for the corresponding output subdynamics. Existing techniques including the LQR approach (e.g., [30]) and the Ackerman's pole placement technique (e.g., [37]) can be used. Specifically, to eliminate oscillations in the desired output during the transition intervals, the state feedback gain $H_{\xi,k}$ should be designed so that all the poles of the output subdynamics $\{\hat{A}_{\xi,k}, B_{\xi,k}\}$ are real. The stiffness of the desired output trajectory thereby can be adjusted by the locations of the poles of $\{\hat{A}_{\xi,k}, B_{\xi,k}\}$.

With the output subdynamics stabilized, the optimal desired transition output trajectory that satisfies $\mathcal{O}1$ and $\mathcal{O}2$ can be obtained by solving an optimal state transition problem [30] with respect to the external input to the r^{th} -order derivative of the output, $\gamma(\cdot)$, i.e., for any given k^{th} output transition within the preview time window, the optimal desired transition output trajectory is obtained by solving the following optimal state transition problem,

$$\min_{\gamma(\cdot)} J(T_k, \gamma) = \min_{\gamma(\cdot)} \int_{t_{k,i}}^{t_{k,f}} \gamma^T(\tau, k) R_\gamma \gamma(\tau, k) d\tau, \quad (2.27)$$

for given boundary desired output and its derivatives for the k^{th} transition, i.e., $\xi_{dtn}(t_{k,i})$ and $\xi_{dtn}(t_{k,f})$, respectively (Note that by Assumption 3, the boundary value for each transition in the preview window is known). In (2.27), $R_\gamma > 0$ of compatible dimension is used to adjust the minimization among different output channels.

Remark 5 Combining (2.23, 2.27) with (2.10–2.15), The cost function in (2.27) is transformed to that in the POOTT problem formulation is (2.10–3.36) by setting $R_\gamma = Q$ (2.10), and $H_{\xi,k} = H_k$ in (2.14). Thus, the solution to (2.27) satisfies $\mathcal{O}1$ and $\mathcal{O}2$.

The solution to the above minimization problem (2.27) can be readily obtained from the optimal state transition result (See, e.g., [30]),

$$\begin{aligned} \gamma^*(t, k) &= R_\gamma^{-1} \mathbf{B}_\xi^T e^{\hat{A}_\xi^T(t_{k,f}-t)} \mathcal{G}^{-1}(T_k) \left[\xi_{dtr}(t_{k,f}) - e^{\hat{A}_\xi(T_1-t_{k,i})} \xi_{dtr}(t_{k,i}) \right] \\ &= \Gamma(T_k, \mathcal{G}(T_k), \xi_{dtr}(t_{k,f}), \xi_{dtr}(t_{k,i})), \quad \text{for } t \in [t_{k,i}, t_{k,f}]. \end{aligned} \quad (2.28)$$

where $\mathcal{G}(T_{tr})$ is the controllability Grammian,

$$\mathcal{G}(T_{tr}) = \int_0^{T_{tr}} e^{\hat{A}_\xi(T_{tr}-\tau)} \mathbf{B}_\xi R_\gamma^{-1} \mathbf{B}_\xi^T e^{\hat{A}_\xi^T(T_{tr}-\tau)} d\tau. \quad (2.29)$$

Thus, for the k^{th} output transition, the desired optimal output trajectory and its derivatives, $\mathbb{Y}_{dtn}(t)$ for $t \in [t_{k,i}, t_{k,f}]$, is obtained by using the optimal external input (2.28) to solve the output subdynamics (2.24), and then the static state-feedback law (2.23),

$$y_{dtn}^{(r)}(t) = H_\xi \xi_{dtn}(t) + \gamma^*(t, k), \quad \text{for } t \in [t_{k,i}, t_{k,f}]. \quad (2.30)$$

Once the desired output for each k^{th} output transition within the preview time window ($k = 1, 2, \dots, N$) is specified, the desired tracking-transition output trajectory within the preview time window can be obtained accordingly. This is summarized in the following Lemma.

Lemma 1 *Let Assumptions (1) to (3) be satisfied, then,*

1. *The desired optimal output trajectory and its derivatives up to the $(r-1)^{th}$, $\xi_d(t)$, that satisfy Objectives \mathcal{O}_1 and \mathcal{O}_2 are given by*

$$\xi_d(t) = \begin{cases} \xi_{dtr}(t), & t \in \mathbf{I}_k \\ \xi_{dtn}(t), & t \in \mathbf{T}_k \end{cases} \quad (2.31)$$

and

$$y_d^{(r)}(t) = \begin{cases} y_{dtr}^{(r)}(t), & t \in \mathbf{I}_k \\ y_{dtn}^{(r)}(t) = H_\xi \xi_{dtn}(t) + \gamma^*(t, k). & t \in \mathbf{T}_k \end{cases} \quad (2.32)$$

for $k = 1, 2, \dots, N$, where $\xi_{dtr}(t)$ is the user-specified desired output trajectory for the tracking intervals, and $\xi_{dtn}(t)$ is obtained by solving the output subdynamics (2.24) with the optimal external input $\gamma^*(t, k)$ for $t \in \mathbf{T}_k$,

$$\gamma^*(t, k) = \Gamma(T_k, \mathcal{G}(T_k), \xi_{dtr}(t_{k,f}), \xi_{dtr}(t_{k,i})), \quad (2.33)$$

where the function $\Gamma(\cdot, \cdot, \cdot, \cdot)$ is as defined in (2.28);

2. *At the transition instants, the desired output trajectory is smooth up to the $(r-1)^{th}$ derivative, i.e., for each $k = 1, 2, \dots, N$,*

$$\xi_{dtr}(t_{k,i}^-) = \xi_{dtn}(t_{k,i}^+), \quad \xi_{dtn}(t_{k,f}^-) = \xi_{dtr}(t_{k,f}^+), \quad (2.34)$$

The Lemma follows directly from the fact that the output trajectory for each transition interval is the solution to the optimal state transition of the output subdynamics (2.21) for each given transition interval \mathbf{T}_k ($k = 1, 2, \dots, N$).

Remark 6 *Note that discontinuity can occur at the transition instants in the r^{th} derivative of the desired output,*

$$y_{dtr}^{(r)}(t_{k,i}^-) \neq y_{dtn}^{(r)}(t_{k,i}^+), \quad y_{dtn}^{(r)}(t_{k,f}^-) \neq y_{dtr}^{(r)}(t_{k,f}^+). \quad (2.35)$$

2.3.3 Preview-Based Control Input for the Tracking-Transition Period

Next, we present the second half of the solution to the POOTT problem—the control input that satisfies Objective \mathcal{O}_3 . We start with obtaining the control input that exactly tracks the above desired output trajectory with tracking-transition switching when there exists infinite preview (i.e., $u_{inv}(\cdot)$ in (3.2)).

Inverse Input For Exact Tracking: Infinite Preview Case

The above optimal desired output trajectory with tracking-transition switching is smooth up to the r^{th} -order—the relative degree of System (2.1). Thus, by the stable-inversion theory [3], exact tracking of such a desired trajectory exists for nonminimum-phase systems, provided that the entire trajectory is known a priori, i.e., infinite preview of the desired trajectory exists. The corresponding control input (called *the inverse input*) is noncausal and thereby can be applied to the tracking-transition planning applications such as nanomanufacturing [15, 38], where the desired trajectories in all tracking intervals along with the desired transitions in all transition intervals are specified a priori. In addition, the inverse input allows the quantification of the tracking performance when the preview is finite.

The inverse input for exact output tracking is given by

$$u_{inv}(t) = \mathbf{M}_Y \mathbb{Y}_d(t) + \mathbf{M}_s \eta_s^*(t) + \mathbf{M}_u \eta_u^*(t), \quad (2.36)$$

where $\mathbb{Y}_d(t)$ is given by (2.31, 2.32), and the stable and the unstable internal dynamics, $\eta_s^*(t)$ and $\eta_u^*(t)$, respectively, are obtained by using the desired output $\mathbb{Y}_d(t)$ to solve the stable and

the unstable internal dynamics (2.21) forward and backwards in time, respectively,

$$\begin{aligned}\eta_s^*(t) &= e^{A_s(t-t_0)}\eta_s^*(t_0) + \int_{t_0}^t e^{A_s(t-\tau)} B_s \mathbb{Y}_d(\tau) d\tau \\ \eta_u^*(t) &= - \int_t^\infty e^{-A_u(\tau-t)} B_u \mathbb{Y}_d(\tau) d\tau.\end{aligned}\tag{2.37}$$

where t_0 denotes the beginning time instant of the entire tracking- transition operation, and $\eta_s^*(t_0)$ can be set as the stable part of the internal dynamics at t_0 (obtained from the system state at t_0 through the state-transformation in (2.18)). Note that the integration in (2.37) must be partitioned into tracking and transition intervals according to the partition of the desired trajectory $Y_d(\cdot)$ in (2.31, 2.32).

Optimal-Preview-Based Inverse Input: Finite Preview Case

Obtaining the preview-based inverse control amounts to solving the unstable part of the internal dynamics (2.21) in the presence of tracking-transition switching—the stable part of the internal dynamics, $\eta_{s,p}(t)$, is the same as that for the infinite preview scenario, i.e.,

$$\eta_{s,p}(t) = \eta_s^*(t), \quad \text{for } \forall t, \tag{2.38}$$

where $\eta_s^*(t)$ is given by (2.37). The unstable internal dynamics is solved with a finite-preview of future desired trajectory T_p as,

$$\eta_{u,p}(t) = e^{-A_u(t_c+T_p)}\hat{\eta}_u(t+T_p) - \int_t^{t_c+T_p} e^{-A_u(\tau-t)} B_u \mathbb{Y}_d(\tau) d\tau \tag{2.39}$$

where $\hat{\eta}_u(t_c + T_p)$ is the estimated future boundary value of the unstable internal dynamics at the end of the preview time window $(t_c + T_p)$, i.e., the bounded internal dynamics can be considered as a boundary-value problem with unknown boundary value [25]. Particularly, in our previous work of preview-based inversion approach [5, 7], this unknown future boundary value is set to zero,

$$\hat{\eta}_u(t + T_p) = 0 \tag{2.40}$$

However, an optimal estimation of the boundary condition [8] can be obtained and incorporated into the proposed approach (See Sec. 2.3.4 later). As in (2.37), the integral in (2.39) needs to be partitioned into tracking intervals and transition ones according to the partition of the desired

output trajectory in (2.31, 2.32). Thus, with the preview-based solution to the unstable internal dynamics (2.39), the preview-based inverse input to the POOTT problem is obtained as

$$u_{pre}(t) = \mathbf{M}_Y \mathbb{Y}_d(t) + \mathbf{M}_s \eta_{s,p}(t) + \mathbf{M}_u \eta_{u,p}(t) \quad (2.41)$$

Next, we show that the above preview-based solution achieves the objective $\mathcal{O}3$. The critical issue is to maintain the smoothness of the internal dynamics as well as the system state across all tracking-transition switching instants, even in the presence of discontinuity in the r^{th} order derivative of the desired trajectory (See Remark 6). This issue is addressed in Lemma 2 below.

Lemma 2 *Let Assumptions 1—3 be satisfied, and the preview-based optimal output-input trajectory be given by (2.38) to (2.41). Then*

1. *The stable part of the internal dynamics is continuous at both the initial and the final instants of each transition interval, i.e.,*

$$\eta_s(t_{k,i}^-) = \eta_s(t_{i,f}^+), \text{ and } \eta_s(t_{k,f}^-) = \eta_s(t_{k,f}^+), \quad \text{for } k = 1, 2, \dots, N \quad (2.42)$$

2. *Provided that the estimation of the boundary condition of the unstable internal dynamics, $\hat{\eta}_u(t_c + T_p)$, is continuous, i.e., $\hat{\eta}_u(t) \in \mathbf{C}(\mathbb{R})$, the preview-based solution to the unstable internal dynamics (2.39) is continuous at both the initial and the final instants of each transition interval, i.e.,*

$$\eta_u(t_{k,i}^-) = \eta_u(t_{k,i}^+), \text{ and } \eta_u(t_{k,f}^-) = \eta_u(t_{k,f}^+), \quad \text{for } k = 1, 2, \dots, N \quad (2.43)$$

3. *Smooth state transition is achieved at both the initial and the final transition instants,*

$$x_{tr}(t_{k,i}^-) = x_{tn}(t_{k,i}^+), \quad x_{tr}(t_{k,f}^-) = x_{tn}(t_{k,f}^+). \quad (2.44)$$

Proof Note that the desired output trajectory and its derivatives are bounded, i.e., $\mathbb{Y}_d(\cdot) \in L^\infty(\mathbb{R})$, and the stable internal dynamics is integrable for forward time flow, i.e., $e^{A_s(\cdot)} B_s \in L^1(\mathbb{R}^+)$. Thereby, their convolution—the stable internal dynamics (2.37)—is uniformly continuous (e.g., [39]) at all time instant t , particularly, at the tracking-transition switching instants. This shows Result 1. Similarly, the integral part of the preview-based unstable internal dynamics solution in (2.39) is also uniformly continuous at all time instant t . Thus, Result 2 follows

if the estimated boundary condition is continuous. Note that the continuity of the estimated boundary value $\hat{u}(t)$ can be maintained by simply setting $\hat{u}(t)$ as be a constant (e.g., zero as in (2.40)). For Result 3, we note that the obtained preview-based input (2.41) is bounded, $u_{pre}(\cdot) \in L^\infty(\mathbb{R})$, thus the same argument applies to the continuity of the system state across the transition instants. This completes the proof. ■

The amount of preview time T_p that guarantees the precision in the preview-based inverse input can be quantified for given precision in the input.

Lemma 3 *Let the Assumptions in Theorem 2 be satisfied, and the future boundary value of the unstable internal dynamics be set to zero, i.e., $\hat{\eta}_u(t_c + T_p) = 0$, then for any given precision in the preview-based inverse input ϵ_i , there exists a finite preview time $T_p < \infty$ such that the required input precision (3.2) can be achieved. Particularly, the required preview time is given by*

$$T_p^* \triangleq \frac{1}{\alpha} \ln \left(\frac{K}{\alpha \epsilon} \right), \quad (2.45)$$

where the positive constant α is the bound of the exponentially-decaying rate of the unstable internal dynamics,

$$\|e^{-A_u t}\|_2 \leq K_1 e^{-\alpha t}, \quad \forall t \geq 0; \quad (2.46)$$

and the positive constant K is defined as

$$K \triangleq K_1 K_y \|C_u\|_2 \|B_u\|_2,$$

with $K_y \triangleq \|\mathbb{Y}_d(\cdot)\|_\infty = \sup_{t \in \mathbb{R}} \|\mathbb{Y}_d(t)\|_2$.

Proof The proof follows arguments similar to those in [5] and thereby is omitted. ■

Remark 7 *As discussed in Remark 3, at time instant t_c , if the preview time window crosses the tracking-to-transition switching and enters next transition interval \mathbf{T}_{N+1} , i.e., if $t_c + T_p \geq t_{N,i}$ and $t_c + T_p - \epsilon < t_{N,i}$ for any given $\epsilon > 0$, the preview time T_p will be increased instantly by the amount of the next transition interval, i.e., $T_p = T_p + (t_{N,f} - t_{N,i})$. As at the time instant t_c , the desired output trajectory for the next transition interval has been designed by Lemma 3, such an increase of the preview time will improve the tracking precision.*

Therefore, this chapter extends the preview-based inversion approach to solve the problem of nonperiodic tracking-transition switching with preview. In applications such as robot manipulation [16] and nanomanufacturing [38], reducing the amount of needed preview time is crucial because in these applications, the amount of preview time is limited by constraints such as cost, hardware performance and physical constraints (as in active noise control [35]). The needed preview time can be reduced by utilizing the knowledge of the previewed future desired trajectory to optimally estimate the unknown future boundary value $\eta_u(t_c + T_p)$.

2.3.4 Optimal Estimation of the Unknown Boundary Value of the Unstable Internal Dynamics

By using the optimal preview-based inversion approach [8], the optimal estimation unknown future boundary value of the unstable internal dynamics can be obtained by minimizing a linear quadratic regulation (LQR) cost function that trades off the output tracking error with respect to the input energy within the preview time window. Note in [8], the optimal preview-based inversion technique is developed for tracking smooth desired output trajectory. The extension to the proposed POOTT problem requires accounting for the discontinuity, at the tracking-transition switching instants, in the r^{th} -order derivative of the desired trajectory and that in the preview-based inverse input (See (2.35)). Concretely, the following cost function with respect to the boundary value is minimized,

$$\min_{\mathbb{B}} J(t_c, \mathbb{B}) = \min_{\mathbb{B}} \int_{t_c}^{t_c+T_p} \|\xi(\tau) - \xi_d(\tau)\|_Q^2 + \|u_p(\tau)\|_R^2 d\tau \quad (2.47)$$

where

$$\mathbb{B} \triangleq \hat{\eta}_u(t_c + T_p), \quad (2.48)$$

and

$$\|M\|_W \triangleq M^T W M,$$

is the weighted 2-norm of matrix M w.r.t. the semi-positive symmetric weight $W \geq 0$. Similar to the integral in the preview-based solution to the unstable internal dynamics (See (2.39)), the integral in the above cost function should be partitioned into tracking and transition sections according to the partition of the desired trajectory in (2.2–2.6). However, as the desired trajectory

is bounded up to the r^{th} order derivatives, the optimal estimation of the boundary condition $\hat{\eta}(t_c + T_p)$ in [8] can be extended to the proposed tracking-transition switching scenario.

Theorem 1 [8] *Let Assumptions 1 to 3 be satisfied, then the optimal boundary condition for the unstable internal dynamics $\hat{\eta}_u^*(t_c + T_p)$ that minimizes the cost function (2.47) is given by*

$$\mathbb{B}^* \triangleq \hat{\eta}_u^*(t_c + T_p) = -\mathcal{I}_1(T_p)^{-1} \mathcal{I}_2(t_c, T_p)^T. \quad (2.49)$$

where

$$\begin{aligned} \mathcal{I}_1(T_p) &\triangleq \int_{t_c}^{t_c+T_p} \Psi_x(\tau)^T Q_\xi \Psi_x(\tau) + \mathbf{P}_{E_u}^T(\tau) R \mathbf{P}_{E_u}(\tau) d\tau \\ \mathcal{I}_2(t_c, T_p) &\triangleq \int_{t_c}^{t_c+T_p} [\phi_x(t_c, \mathbb{Y}_d, \tau) - x_{ref}(\tau)]^T Q_\xi \Psi_x(\tau) + \mathbf{P}(\mathbb{Y}_d, \tau)^T R \mathbf{P}_{E_u}(\tau) d\tau \end{aligned} \quad (2.50)$$

and

$$Q_\xi \triangleq M_\xi^T Q M_\xi$$

is the modified weight (with M_ξ given by (2.18)), and the vector function $\phi_x(t_c, \mathbb{Y}_d, t)$ and the matrix function $\Psi_x(t)$ are defined as

$$\begin{aligned} \phi_x(t_c, \mathbb{Y}_d, t) &\triangleq e^{A(t-t_c)} x(t_c) + \int_{t_c}^t e^{A(t-\tau)} B \mathbf{P}(\mathbb{Y}_d, \tau) d\tau \\ \Psi_x(t) &\triangleq \int_{t_c}^t e^{A(t-\tau)} B \mathbf{P}_{E_u}(\tau) \quad \text{with} \end{aligned} \quad (2.51)$$

$$\begin{aligned} \mathbf{P}(\mathbb{Y}_d(\cdot), t) &\triangleq \mathbf{M}_Y \mathbb{Y}_d(t) + \mathbf{M}_s \eta_s(t) + \mathbf{M}_u \hat{\eta}_u(t) \\ \mathbf{P}_{E_u}(t) &\triangleq \mathbf{M}_u e^{-A_u(t_c+T_p-t)}. \end{aligned} \quad (2.52)$$

Remark 8 *Note that when computing the optimal boundary value, the reference state $x_{ref}(t)$ in (2.50) is not needed—With the mapping matrix M_ξ , it is instead converted to the derivatives of the desired output, $\xi_d(t)$.*

The critical issue to incorporate the above optimal estimation of boundary value in the proposed approach is to guarantee the continuity of the boundary value across the switching instants (See Lemma 2 (2)).

Lemma 4 *The optimal estimation of the future boundary value of the unstable internal dynamics in (2.49) to (2.52) is continuous with respect to the time instant t_c .*

Proof The proof amounts to showing that the vector function $\mathcal{I}_2(t_c, T_p)$ (in (2.50)) is continuous w.r.t. t_c (as the matrix $\mathcal{I}_1(T_p)$ is a constant matrix for given preview time). First, note that similar to the argument in Lemma 2, we can show that the vector functions $\phi_x(t_c, \mathbb{Y}_d, t)$ and $\Psi_x(t)$ in (2.51) are continuous w.r.t. t . Then, by Lemma 2 (c), the vector function $\phi_x(t_c, \mathbb{Y}_d, t)$ is also continuous w.r.t. t_c . As a result, the first part of the integral (i.e., the integral of the first term before “+”) in $\mathcal{I}_2(t_c, T_p)$ is continuous w.r.t. t_c . Moreover, note that although discontinuity occurs in the vector function $\mathbf{P}(\mathbb{Y}_d(\cdot), t)$, this vector is integrable on any given interval $[t_c, t_c + T_p]$, therefore the second part of the integral $\mathcal{I}_2(t_c, T_p)$ is absolutely continuous (thereby continuous) w.r.t. t_c (e.g., [39]). This completes the proof. ■

2.4 Simulation Example: Nanomanipulation

We illustrate the proposed approach by a simulation example of using a piezoelectric actuator model in nanomanipulation.

2.4.1 Nonperiodic Output Tracking-Transition Switching with Preview in Nanomanipulation

Preview-based output tracking with nonperiodic tracking-transition switching is needed in applications such as nanomanipulation, nanofabrication [15] and robotic operation [16]. In nanomanipulation based on scanning probe microscope (SPM), a micro-machined cantilever probe driven by a piezoelectric actuator is utilized to manipulate nanoscale subjects both horizontally and perpendicularly [15], to build integrate circuit using nanotubes [40], or to conduct surgery operations on a single live cell [41]. In these operations, precision output tracking is needed to perform trajectory dependent tasks (e.g., to push a nanotube to a specific location), while swift transition is needed to reposition the probe to the desired location (e.g., to relocate the probe to be close to the nanotube where the next operation takes place). Clearly, frequent tracking-transition switching occur in these operations where multiple tasks are required at multiple locations. As nanomanipulation usually involves online generated commands by the user (e.g., through an imaging based interface) [5], preview-based approach becomes a nature choice to

address the required output tracking-transition switching, particularly at high-speed. Thus, in this simulation, a piezoelectric actuator model in nanomanipulation operation was considered.

The dynamics model of the piezo actuator is as follows.

$$G(s) = \frac{x(s)}{u_x(s)} = K_x \frac{\prod_{q=1}^4 (s - z_q)}{\prod_{r=1}^6 (s - p_r)} \quad (2.53)$$

where the input is the voltage applied to the piezoelectric actuator (in Volt), and the output is the displacement of the piezo actuator (in angstrom \AA), and the Laplace transform variable s is in rad/ms (to reduce the numerical computation error), and

$$\begin{aligned} K_x &= 29.28, \\ z_q &= 9.274 \pm 41.659i, -2.484 \pm 30.434i, \\ p_r &= -0.188 \pm 31.326i, -0.857 \pm 24.570i, -20.263, -15.198 \end{aligned} \quad (2.54)$$

The corresponding frequency response is shown in Fig. 2.2. Note that the above piezo actuator dynamics model is nonminimum phase with a pair of complex zeros on the right-half-plan.

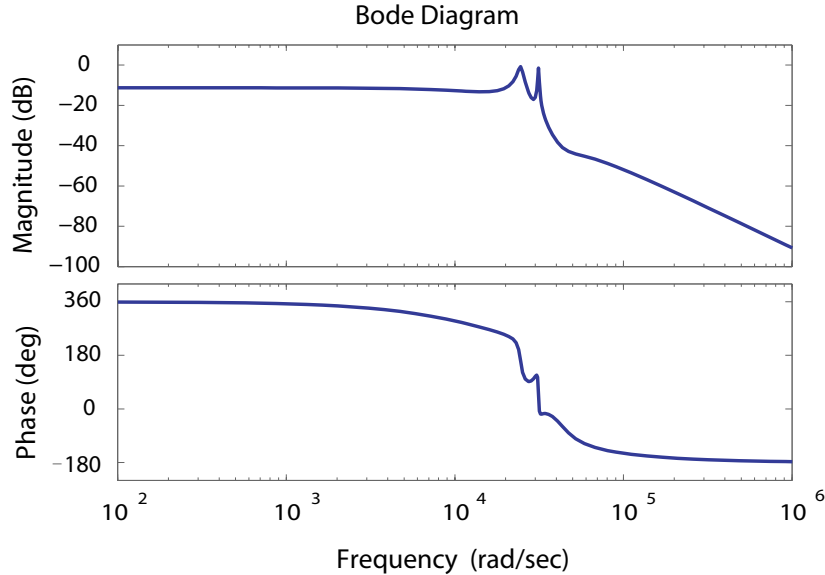


Figure 2.2: The frequency response of the piezo actuator mode

2.4.2 Output Tracking Form, Internal Dynamics, and Inverse Input

The piezo dynamics model in (3.77) has a relative degree of two. The minimal state-space representation of the piezoelectric dynamics model (3.77) was obtained by using a balance

realization, and then, the inversion based input was obtained as,

$$\begin{aligned} u_{inv}(t) = & [20.3906 \quad -0.2032 \quad 0.0342] \mathbb{Y}_d(t) \\ & + [-0.5609 \quad 4.5764] \eta_s(t) + [10.9054 \quad -20.0614] \eta_u(t), \end{aligned} \quad (2.55)$$

where

$$\mathbb{Y}_d(t) = [y_d(t) \quad \dot{y}_d(t) \quad \ddot{y}_d(t)]^T \quad \text{and}$$

$$\begin{aligned} \dot{\eta}_s(t) = & \begin{bmatrix} -2.4839 & 30.4342 \\ -30.4342 & -2.4839 \end{bmatrix} \begin{bmatrix} \eta_{s,1}(t) \\ \eta_{s,2}(t) \end{bmatrix} + \begin{bmatrix} -8.4186 & 0.0714 & -0.0112 \\ 6.3290 & -0.1005 & 0.0155 \end{bmatrix} \mathbb{Y}_d(t) \\ \dot{\eta}_u(t) = & \begin{bmatrix} 9.2736 & -41.6586 \\ 41.6586 & 9.2736 \end{bmatrix} \begin{bmatrix} \eta_{u,1}(t) \\ \eta_{u,2}(t) \end{bmatrix} + \begin{bmatrix} 45.4971 & -0.3607 & 0.0651 \\ -37.0249 & 0.3158 & -0.0579 \end{bmatrix} \mathbb{Y}_d(t) \end{aligned} \quad (2.56)$$

The above inverse control input and the internal dynamics were used in output tracking during both the tracking and the transition sessions. The key was to (1) obtain the optimal output trajectory for the transition sessions (See Sec. 2.3.2), and (2) determine the preview-based internal dynamic states η_s and η_u in the inverse input (2.55) across the switching instants (See Sec. 2.3.2).

2.4.3 Implementation of the POOTT Technique

Desired Transition Trajectory Design To implement the proposed technique to the POOTT problem, we start with designing the optimal desired output trajectory for the transition sections. Note that in experimental applications, only the optimal desired output trajectory for transition sections within the preview window is designed. However, as the design of the optimal transition trajectory did not depend on the preview-based input, we designed, in the simulation, the optimal output transition trajectory for all transition sections at once—however, at each time instant, only the desired trajectory within the given preview time window was used for control.

To emulate possible tracking scenarios in real nanomanipulation applications, three different types of trajectories (ramp, sinusoidal, and exponential signals) were incorporated into the

desired trajectory of the tracking sessions. As shown in Fig. 2.3 (a), the desired trajectory contained a total of six tracking sessions. Then the desired trajectory for the transition sections were designed according to Eqs. (2.24, 2.28, 2.29). Specifically, the output-related subdynamics (2.21) was stabilized first, by using the standard LQR state-feedback approach [30]. Then, the optimal desired transition trajectory that guaranteed the smoothness of the desired output across the switching instants with minimal vibrations (Requirements $\mathcal{O}1$ and $\mathcal{O}2$) were obtained by using the optimal state transition method (See (2.28, 2.29)). The obtained optimal output transition trajectory is shown in Fig. 2.3 (a) for $Q = \text{diag}([10 \ .001])$, and $R = [1]$. For comparison, we also chose a different set of Q and R at $Q = \text{diag}([.001 \ .001])$ and $R = [1]$ when stabilizing the output subdynamics. The corresponding optimal output transition trajectory is shown in Fig. 2.3 (b).

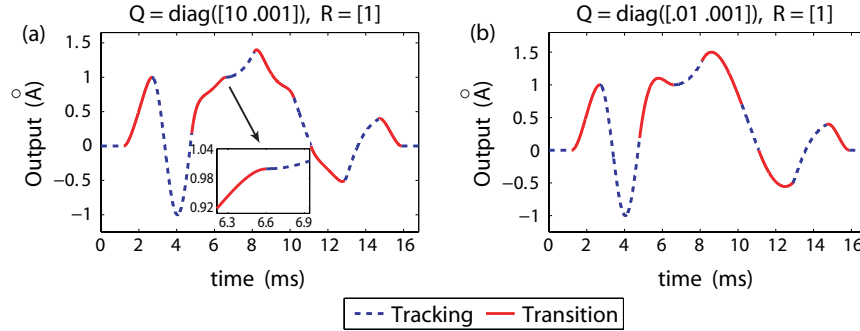


Figure 2.3: Comparison of the desired trajectory for the transition sections obtained by using the LQR technique with different weights.

The simulation results clearly demonstrate that the proposed method guarantee the smoothness of the desired output trajectory across tracking-transition switching instants (See the insert in Fig. 2.3 (a)). Comparing Fig. 2.3 (a) with Fig. 2.3 (b), it is evident that different stabilization of the output subdynamics results in different desired output trajectory for transition sessions: The larger state weight Q relative to the input energy weight R results in less variation in the transition trajectory. A similar effect can also be obtained by using other stabilization methods such as pole placement. The desired trajectory in Fig. 2.3 (a) was used in the simulation.

Optimal preview-based inverse input To obtain the preview-based inverse input for tracking the output trajectory with tracking-transition switching, the stable part of the internal dynamics

was solved first (See Sec. 2.3.3), where the desired output $\mathbb{Y}_d(\tau)$ in (2.56) was specified according to Lemma 1 (See (2.31–2.34)), and the initial boundary value $\eta_s^*(t_0)$ was set to zero (as initially both the system and the output were at zero). Then, the preview-based solution to the unstable internal dynamics was solved for a given finite-preview time (See (2.39)), where the unknown future boundary value of the unstable internal dynamics (at the end of the preview time window) was optimally estimated (See Sec. 3.3.2). To ensure the tracking precision, preview time of $T_p = 0.8$ ms was used. This preview time was chosen based on the estimated settling time of the unstable internal dynamics (~ 1 ms) (See (2.56)).

For comparison, the input shaping technique [31] was also applied to design and track the desired output trajectory during the transition sections. Then a feedback controller consisting of a notch-filter in serial with a PI controller was used for the output tracking during the tracking sections. The desired output transition trajectory was designed by first obtaining the input shaper, and then convolving the input shaper with the chosen desired reference command signal for the transition sections [31]. The input shaper was obtained as a series of impulses (Readers are referred to [31] for details). The reference command signal for the transition sections was chosen as ramp signals with a flat final period. As the piezo dynamics model consisted of two vibration modes (i.e., two resonant peaks, See (3.3.1) and Fig. 2.2), the input shaper was designed by solving the vibration and robustness constraints, particularly, the zero vibration and derivative (ZVD) constraints, for each of these two modes simultaneously [31]. The resulting input shaper $S(t)$ consisting of five impulses was obtained as

$$S(t) = \sum_{i=1}^5 A_i \delta(t - \tau_i) \quad (2.57)$$

where “ $\delta(t)$ ” denotes the impulse function (i.e., Dirac delta function), and the amplitude and time delay of each impulse $\delta(t)$, A_i and τ_i , are given by

$$\begin{bmatrix} A_i \\ \tau_i \end{bmatrix} = \begin{bmatrix} 0.1533 & 0.3010 & 0.2749 & 0.1477 & 0.1232 \\ 0 & 0.1003 & 0.1279 & 0.2006 & 0.2557 \end{bmatrix} \quad (2.58)$$

The obtained reference command signal and the modified command signal convolved with the input shaper is shown in Fig. 2.4 (a), and the desired trajectory of transition sections obtained by using the reference command signal and that by using the modified command signal are compared in Fig. 2.4 (b).

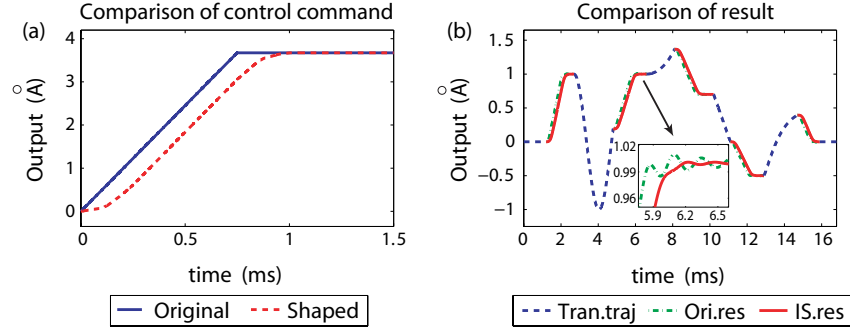


Figure 2.4: (a) Comparison of the original command (“Original”) with the shaped command convolved by the input shaper (“Shaped”); and (b) comparison of the system response using the original command and that by using the shaped command, where the insert zooms-in one switching instant.

The feedback controller during the tracking sections was designed by using a notch filter to “cancel” the dominant resonant mode at 24.6 KHz and 31.3 KHz first (See Fig. 2.2). Then a PI controller was designed for the modified system dynamics (the piezo dynamics model in (3.77) with the notch filter in front). The parameters of the PI controller at $K_p = 1$, $K_i = 40000$ were chosen to achieve small rise time and eliminate the steady-state error of the modified system. In the simulation, the control input was switched between the input-shaping feedforward control (for the transition sections) and the PI-notch filter feedback control (for the tracking sections). The control input at the switching instants was determined by maintaining the continuity of the system output.

2.4.4 Simulation results and discussion

Output tracking at three different speeds were evaluated in the simulation, i.e., the desired trajectory shown in Fig. 2.3 (a) were speeded up to obtain the desired trajectory at higher speed. The output tracking results for the low-speed tracking are compared in Fig. 2.5 for those obtained by using the proposed approach (with a preview time of 0.8 ms) in (a), (c), and those obtained by using the input shaping-PI control in (b), (d). The tracking results obtained by these two methods for the higher-speed tracking are also compared in Fig. 2.6, where the same preview time of $T_p = 0.8$ ms was used. Moreover, we also applied the proposed approach to track an even higher speed of desired trajectory where multiple tracking-transition switching

occurred in the preview window of 0.8 ms. The tracking results were shown in Fig. 2.7. As discussed below, the comparison for the two slower cases clearly demonstrate the superior tracking performance of the proposed method over the input shaping-PI control method, tracking of this higher-speed desired trajectory by using the input-shaping PI-control was not conducted.

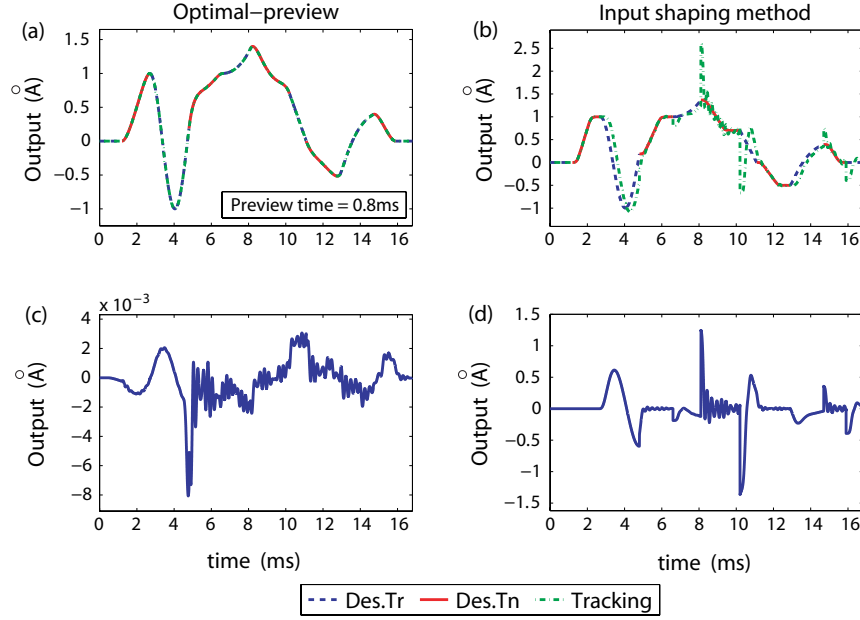


Figure 2.5: Comparison of (upper row) the output tracking at relatively low-speed by using (a, c) the proposed approach with (b, d) that by using the input shaping-PI control method, and (lower row) the corresponding tracking errors.

The simulation results show that by using the proposed inversion-based POOTT technique, precision output tracking can be maintained throughout the entire tracking-transition course. In the low speed tracking, relatively good tracking can be achieved by using the input-shaping-PI control except at the switching instants—large oscillations occurred at the switching instants because only the continuity of the output, not the whole system state, was maintained at the switching instants. Such large oscillations at switching instants, caused by the mismatch of the system state, were dramatically reduced by using the proposed technique. Note that as discontinuity occurred at the switching instants in the r^{th} derivative of the desired output trajectory, the tracking error at the switching instants were larger than that at other time instants. However, the relative RMS tracking error $E_2(\%)$ by using the proposed control technique was still very small (only 0.14%), over 70 times smaller than that of using the input shaping-PI control

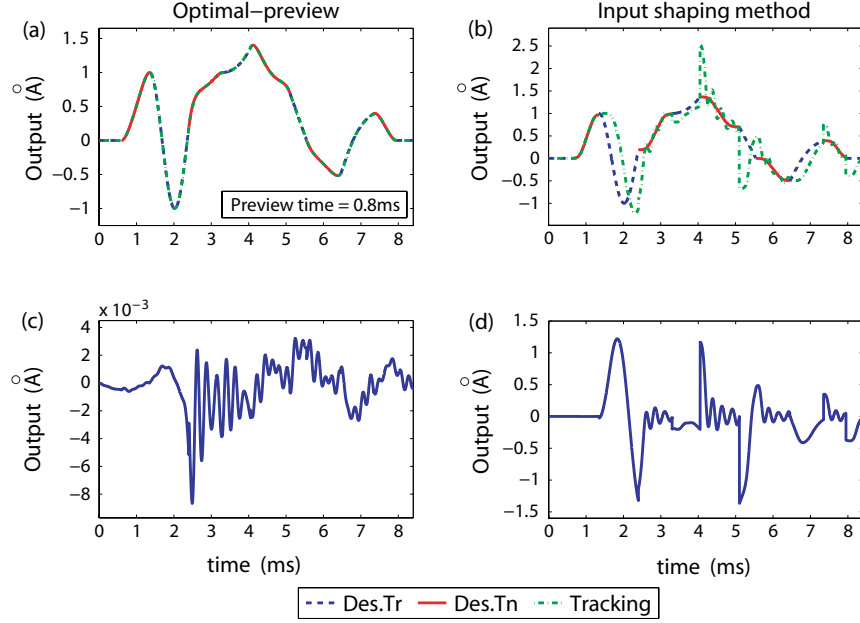


Figure 2.6: Comparison of (upper row) the output tracking at middle speed by using (a, c) the proposed approach with (b, d) that by using the input shaping-PI control method and (lower row) the corresponding tracking errors.

method (9.85%, See Fig. 2.5). Such a precision tracking across all tracking-transition switching was maintained even when the trajectory became much faster—at middle-speed tracking and high-speed tracking, the relative RMS tracking error $E_2(\%)$ were still very small (about 0.17% and 0.28%, See Fig. 2.6, 2.7). Particularly, simulation results showed that almost the same tracking precision was maintained even when there existed multiple tracking-transition switching within the preview time window (for the high-speed desired trajectory of 1.68 ms total time). Whereas the overall output tracking by using the input shaping-PI feedback control method deteriorated as the trajectory became faster (See Figs. 2.5, 2.6). Therefore, the simulation results demonstrate that smooth output tracking over nonperiodic tracking-transition switching can be achieved by using the proposed technique.

Effect of Preview-Time on Output Tracking To demonstrate the effect of the amount of preview time on the tracking performance of output tracking-transition switching, four different preview times ($T_p = 0.08$ ms, 0.15 ms, 0.3 ms and 0.8 ms) were used in the simulation. Additionally, to illustrate the efficacy of optimal boundary value estimation [8] to reduce the amount of preview time, we also compared the output tracking by using the optimal estimation of the boundary value in the proposed method (called *the optimal boundary POOTT technique*)

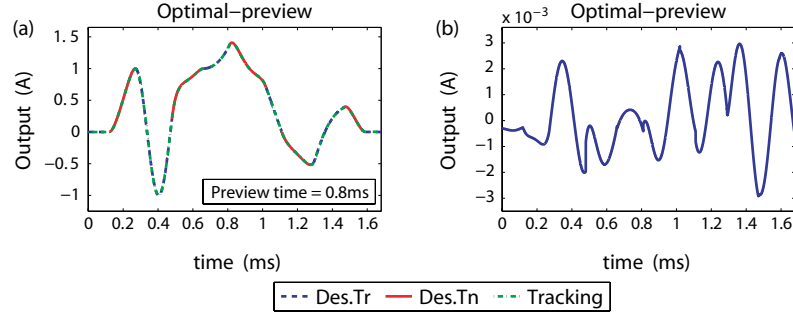


Figure 2.7: The output tracking at high speed by using the proposed approach (a) and the corresponding tracking errors (b).

with that by using zero boundary value (See (2.40)) in the proposed method (called *the zero boundary POOTT technique*). The tracking results obtained by using these two methods are compared in Fig. 2.8 for the preview time $T_p = 0.08$ and 0.15 ms, along with that obtained with zero preview time. The output tracking results for the other two longer preview times $T_p = 0.3$ and 0.8 ms are also compared in Fig. 2.9.

The simulation results show that having an enough amount of preview time was critical to the tracking of nonperiodic output tracking-transition switching with preview. For both the zero-boundary and the optimal boundary POOTT methods, the tracking error decreased as the preview time increased. Without preview ($T_p = 0$ ms), however, tracking error as large as 5 times over the desired output amplitude occurred (See Fig. 2.8 (a)). Such a large tracking error was dramatically reduced by using preview in the proposed POOTT technique (See Fig. 2.8 (b), (c), (d) and Fig. 2.9). Particularly, with preview time of 0.8 ms, output tracking error as small as $< 0.4\%$ was achieved by using both the zero-boundary and the optimal-boundary POOTT methods. Thus, with enough preview time, precision output tracking over nonperiodic tracking-transition switching can be achieved by using the proposed POOTT technique.

The simulation results also show that the amount of preview time for achieving precision output tracking can be substantially reduced by using the optimal boundary instead of the zero boundary POOTT technique. For example, when the preview time was as small as $T_p = 0.08$ ms, relatively good output tracking over the entire tracking-transition course can still be obtained by using the optimal-boundary POOTT method (As shown in Fig. 2.8 (a), (c), the relative RMS tracking error $E_2(\%)$ was about 1.48%), whereas the output tracking obtained by using the

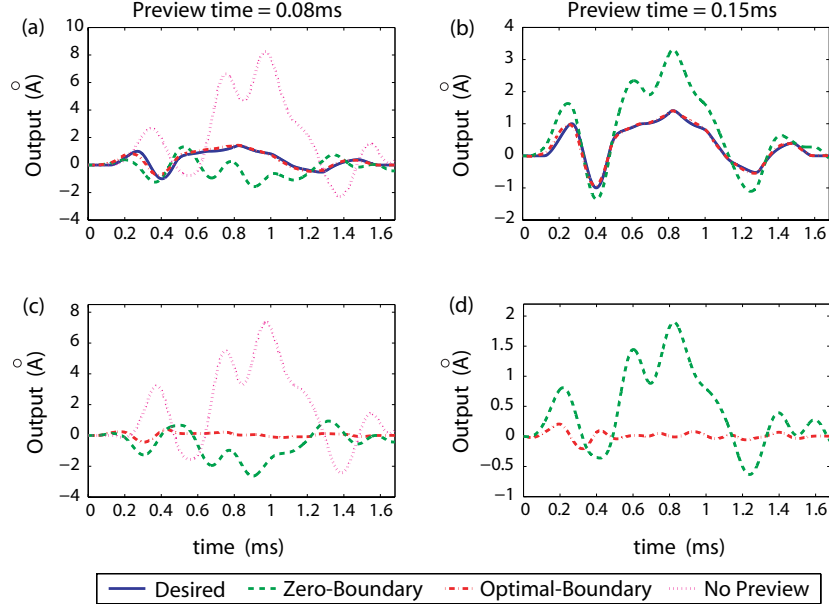


Figure 2.8: Comparison of (upper row) the output tracking and (upper row) the tracking error obtained by using the optimal boundary POOTT method (“Optimal-Boundary”) with those obtained by using the zero-boundary POOTT method (“Zero-Boundary”) and no-preview for the preview time of (left column) $T_p = 0.08$ ms and (right column) $T_p = 0.15$ ms.

zero-boundary POOTT technique was completely lost (See Fig. 2.8 (a), (c)). As the preview time was increased to $T_p = 0.3$ ms, although the tracking performance of the zero-boundary POOTT technique was significantly improved, the relative RMS tracking error $E_2(\%)$ was still over 15 times larger than that of using the optimal-boundary POOTT method. (See Fig. 2.9 (a), (c)). Therefore, the simulation results demonstrate that the proposed POOTT technique extends the preview-based stable-inversion approach to precision tracking in nonperiodic output tracking-transition switching.

2.5 Conclusions

In this chapter, an inversion-based approach to achieve precision tracking in nonperiodic tracking-transition switching with preview has been proposed. The optimal desired output trajectory for the transition sections was designed by directly minimizing the output energy, and the required control input was obtained by using a preview-based stable-inversion approach. The proposed approach maintained the smoothness of system state across the tracking-transition switching, and the required preview time has been quantified in terms of the system internal dynamics.

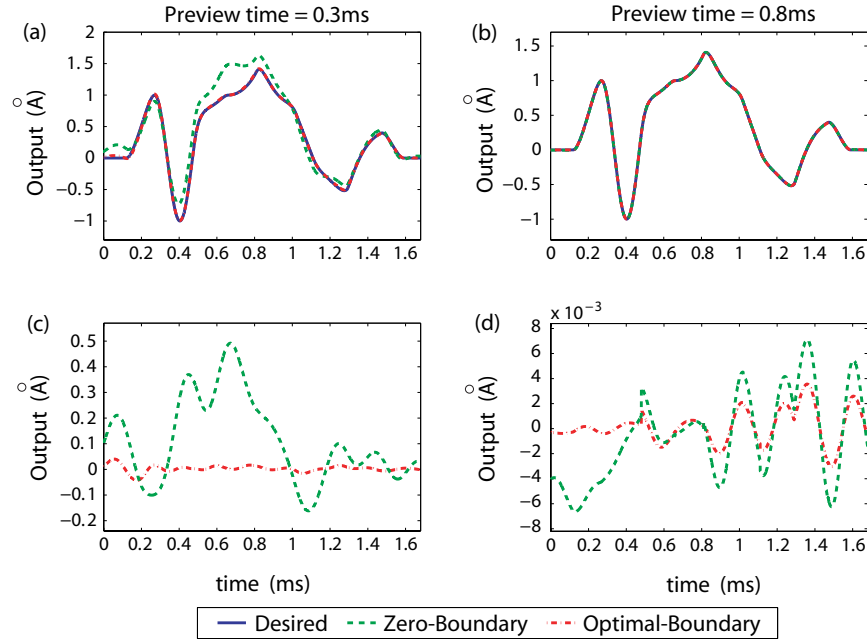


Figure 2.9: Comparison of (upper row) the output tracking and (upper row) the tracking error obtained by using the optimal preview inversion method with those obtained by using the preview inversion method with the preview time of (left column) $T_p = 0.3$ ms and (right column) $T_p = 0.8$ ms.

The preview time was further minimized by incorporating with the recently-developed optimal preview-based inversion approach. The proposed approach was demonstrated by implementing it to a nanomanipulation application using a piezoelectric actuator model in simulation.

Chapter 3

B-Spline-Decomposition-based Output Tracking with Preview for Nonminimum-Phase Linear Systems

Abstract

In this chapter, a B-spline-decomposition-based approach to output tracking with preview for nonminimum-phase systems is proposed. It has been shown and demonstrated through implementations that when there exists a finite (in time) preview of future desired trajectory, precision output tracking of nonminimum-phase systems can be achieved by using the preview-based stable-inversion technique. The performance of this approach, however, can be sensitive to system dynamics uncertainty. Moreover, the computation involved in the implementation can be demanding. We propose to address these challenges by integrating the notion of trajectory decomposition and the iterative learning control technique together. Particularly, the B-splines are used to construct a library of desired output elements and their corresponding control input elements a priori, and the ILC techniques such as the recently-developed multi-axis inversion-based control (MAIIC) approach are used to obtain the control input elements that achieve precision output tracking of the corresponding desired output elements. Then the previewed future desired trajectory is decomposed by using the desired output elements, and the control input is synthesized by using the corresponding input elements with chosen pre- and post- actuation time. The required pre-/post- actuation times are quantified based on the stable-inversion theory. The use of B-splines substantially reduces the number of output elements in the library, and the decomposition-synthesis only occurs at time instants specified by the given preview time and pre-actuation time. The proposed approach is illustrated through simulation study of a nanomanipulation application using a nonminimum-phase piezo actuator model.

3.1 Introduction

In this chapter, we propose a B-spline-decomposition-based approach to the problem of output tracking with preview for nonminimum-phase (NMP) linear systems. It is noted that exact tracking of NMP systems, although cannot be achieved by using feedback control alone [2], can be attained by using the stable-inversion theory [3]. The obtained solution, however, is noncausal—the *unique* stable (bounded) control input (called the inverse input) depends on the entire future desired trajectory, thereby cannot be implemented to applications where the desired trajectory is generated online (e.g., robotics manipulation, or autonomous vehicle guidance). The dependence of the inverse input on the future desired trajectory has been quantified through the development of the preview-based stable-inversion techniques [7, 8]. Such a quantification enables the stable-inversion techniques to be implemented to achieve precision output tracking with a quantified large enough preview time, as demonstrated in various applications [6]. The tracking performance of the preview-based stable-inversion techniques, however, can be sensitive to the uncertainties and variations of system dynamics [17, 42]. Moreover, the online computation involved in the preview-based stable-inversion can be demanding [8, 21, 22]. Motivated by these challenges in practical implementations, the proposed approach aims to achieve precision tracking of output trajectory with preview, while accounting for the system uncertainties and variations, and avoiding heavy online computation demand.

Current approaches to output tracking with preview of NMP systems need to be improved for practical implementations. The benefits of preview for output tracking of NMP systems have been well recognized and exploited in various feedback-based approaches, including the LQ-, the H_∞ - and the ℓ_2 -optimal preview control [43, 44, 45]. Particularly, the preview mechanism has been utilized to alleviate the fundamental performance limits of feedback control to NMP systems [2]. It is shown that the limit of the tracking error exponentially decays with the increase of the preview time. The quantification, however, is limited to SISO systems [46], and special functions only (either step functions, sinusoidal functions, or exponential functions) [2], and does not lead to the design of the “optimal” feedback controller that attains the lower limit. Although the tracking performance limit was extended to general functions in [2], the extension is constrained to SISO systems only with simple zeros, and it is difficult to directly

quantify the tracking error from the limit bound due to the use of the frequency-dependent weight function. These limits in feedback-based approaches to output tracking of preview for NMP systems have been addressed in the preview-based stable-inversion approach [6, 7, 8]. The preview-based stable-inversion technique provides not only a systematic and conceptually straightforward method to design the feedforward controller, but also an explicit quantification of the tracking error that exponentially decays as the increase of the preview time (with the decaying rate governed by the minimum distance of the NM zeros w.r.t. the imaginary axis) [7, 8]. The practical implementation of the preview-based stable-inversion approach, however, still faces challenges arising from the system dynamics variations [6, 17] and the demanding online computation. Specifically, as convolution operation is involved in computing the control input at each sampling instant [20], it might be challenging to implement the preview-based stable-inversion approach when the sampling period is stringent. Therefore, there exists a need to account for these challenges in output tracking with preview of NMP systems for practical implementations.

These uncertainty and computation related challenges can be avoided by using the iterative learning control (ILC) techniques [47]. By exploiting the repetitive nature of the operation, the ILC techniques can compensate for the system dynamics uncertainties—due to either the nonlinear dynamics on the linear part [47] or the part of dynamics that is difficult to model [47] and thereby, difficult to address otherwise without compromising the tracking performance. For example, it has been demonstrated recently in experiments that by using the ILC approach, precision tracking can be achieved for complex trajectories with power spectrum similar to a band-limited white-noise and cut-off frequency beyond the dominant resonant frequency of the system [48]. Also, the iteration mechanism allows the ILC approach to be noncausal—the entire output tracking from the previous iteration trial can be utilized to determine the control input in current iteration, thereby achieving exact output tracking of NMP systems in repetitive applications. Moreover, in ILC framework online computation can be largely avoided, particularly when the ILC law is updated offline. Two constraints, however, limit the ILC approach for the output tracking with preview: One, the entire desired trajectory needs to be known a priori whereas in many applications not the entire but a finite preview of the desired trajectory is available; Secondly, the operation needs to be repetitive whereas those in output

tracking with preview are not. Therefore, challenges still exist to achieve highly-efficient and precision tracking with preview for NMP systems.

The main contribution of this chapter is the development of a trajectory-decomposition-based approach to overcome the above challenges in output tracking with preview for NMP linear systems. The proposed approach utilizes the decomposition concept [49, 50] to enable the use of ILC techniques for non-repetitive output tracking. Specifically, the desired output trajectory is decomposed into a finite summation of output elements, and a library consisting of pairs of desired input-output elements are constructed a priori offline, where the output elements are generated by using uniform B-splines, and the corresponding input elements are obtained by using ILC techniques. Then, the control input is synthesized online via the superimposition principle. To account for the NM zeros and the truncation of the extended B-spline elements (to decompose the previewed output with nonzero starting and/or end values), a finite pre- and post-actuation times are needed to implement each input element. The needed pre- and post-actuation time(s) are quantified based on the stable-inversion theory for the tracking precision of the original previewed desired trajectory. The advantages of using uniform B-splines lie in the small size of the library obtained (e.g., merely seven output elements are needed when the uniform 3^{rd} -degree B-splines are used). The proposed approach is illustrated through a simulation example of nanomanipulation. We note that the notion of library-based decomposition has been explored before for repetitive operations [49, 50]. The fundamental improvements of the proposed approach lie in the utilization of B-splines, the tracking of arbitrary trajectory in non-repetitive operations, and the clarification and quantification of pre- and post-actuation effect, particularly for nonminimum-phase systems. Thus, the proposed approach extends the decomposition-based output-tracking approach for more general and broader applications.

3.2 B-spline-Decomposition-Based Approach to Output-Tracking with Preview

In this section, the proposed approach based on the B-spline decomposition is presented. We start with formulating the considered output tracking problem.

3.2.1 Problem formulation

Consider a square linear time invariant (LTI) system described by

$$\begin{aligned}\dot{x}(t) &= Ax(t) + Bu(t) \\ y(t) &= Cx(t)\end{aligned}\tag{3.1}$$

where $x(t) \in \mathbb{R}^n$ is the state, $u(t) \in \mathbb{R}^q$, $y(t) \in \mathbb{R}^q$ are the input and the output, respectively.

We assume that

Assumption 4 *System (3.1) is controllable and observable, and has a well-defined relative degree $r = [r_1, r_2, \dots, r_q]$ [36]. Moreover, system (3.1) is stable and hyperbolic (i.e., system (3.1) has no zeros on the imaginary axis).*

Assumption 5 *The desired output trajectory is sufficiently smooth, i.e., the k^{th} desired output, for each $k = 1, 2, \dots, q$, is differentiable at least up to the r_k^{th} order. Moreover, a finite preview of the future desired output trajectory exists for a preview time of $T_p < \infty$, i.e., at any time instant t_c , the desired output trajectory is known for $t \in [t_c, t_c + T_p]$.*

Definition 1 *Output Tracking of Nonminimum-Phase LTI Systems with Preview* *Let Assumptions 4, 5 be satisfied, then for any given desired tracking precision $\epsilon > 0$, the output tracking of system (4.1) with preview is to obtain the control input $u_{\text{pre}}(\cdot)$ such that at given time instant t , the output tracking error is less than ϵ for a large enough preview time T_p , i.e.,*

$$\|e_{\text{out}}(t)\|_2 \triangleq \|y_d(t) - y_{\text{pre}}(t)\|_2 \leq \epsilon,\tag{3.2}$$

where $\|a\|_2$ is the standard 2-norm for vector $a \in \mathbb{R}^n$, $y_d(\cdot)$ denotes the desired output trajectory, and $y_{\text{pre}}(\cdot)$ denotes the output tracking trajectory obtained by the preview-based input.

Our goal in solving the above tracking problem is to overcome the uncertainty and computation related challenges as discussed in the Introduction, and achieve precision tracking and high efficiency in implementation. A trajectory-decomposition-based approach is proposed next.

3.2.2 Decomposition-Synthesis-Based Output Tracking Approach

We first present the major three steps involved in the proposed decomposition-based approach without specifying the underline decomposition method used—the steps remain almost

the same when other decomposition methods are used: (1) Construct a library consisting of pairs of desired output elements and their corresponding input elements, during the tracking, at the decomposition time instants (specified by the chosen pre-actuation time and the available preview time), (2) decompose the previewed desired output trajectory into a linear combination of desired output elements, and (3) update the control input by using the input elements corresponding to the selected desired output elements in step (2) (keep the control input the same otherwise).

Library of the desired input-output elements \mathcal{L}_e

The library \mathcal{L}_e consisting of pairs of desired output elements and the corresponding input elements is given as

$$\mathcal{L}_e = \{[y_{k,i}^*(\cdot), u_{k,i}^*(\cdot)] \mid k = 1, 2, \dots, q; i = 1, 2, \dots, N_L\} \quad (3.3)$$

where, for ease of input-synthesis, the desired output element $y_{k,i}^*(\cdot) \in \mathbb{R}^{q \times 1}$ for given k and $i = 1, 2, \dots, N_L$ has only the k^{th} output channel nonzero,

$$y_{k,i}^*(\cdot) = [0 \cdots y_{e,i}^*(\cdot) \cdots 0]^T, \text{ with } i = 1, 2, \dots, N_L, \quad (3.4)$$

and $u_{k,i}^*(\cdot) \in \mathbb{R}^{q \times 1}$ is the corresponding desired input element, i.e.,

$$u_{k,i}^*(\cdot) = [u_{k,i,1}(\cdot) u_{k,i,2}(\cdot) \cdots u_{k,i,q}(\cdot)]^T, \text{ with } i = 1, 2, \dots, N_L. \quad (3.5)$$

Furthermore, the desired output trajectory elements $y_{e,i}^*(\cdot)$ s are sufficiently smooth with a compact support starting from time $t = 0$, i.e., there exists a finite $t_i < \infty$, such that

$$y_{e,i}^*(t) = 0 \text{ for } t \notin [0, t_i], \text{ and } \forall i = 1, 2, \dots, N_L. \quad (3.6)$$

Under Assumptions 4 and 5, there exists a unique desired input to achieve exact tracking of each desired output element—by the stable-inversion theory [3]. As the entire desired output element is known a priori, iterative learning control approach is ideal to obtain the desired input elements in practical implementations. Furthermore, for nonminimum phase systems, the desired input elements are noncausal [3], i.e., to achieve exact tracking of the desired output element starting from time $t_c = 0$, the corresponding input needs to be applied from $t \rightarrow -\infty$

[26, 23], i.e., an infinite long pre-actuation time of the control input is needed. Similarly, an infinite long post-actuation time is needed for the exact tracking of each output element—in order to maintain the necessary state condition when adding two or more input elements together [26, 23]. Thus in practical implementations, truncation of each desired input element to a finite pre- and post-actuation times becomes necessary. The effect of such a finite pre- and post-actuation in the proposed approach is quantified later in Sec. 4.2.2.

In the following, to simplify the notation, for $\alpha \in \Re$ and x a vector (or matrix), αx denotes the vector (or matrix) with each entry scaled by α .

Online Desired Trajectory Decomposition

For any given tracking precision, the required pre- and post-actuation time is proportional to the size of the desired output trajectory [26, 23]. Thus, the pre- and post-actuation time, in general, can be different for different output channel and/or different decomposition instant (defined immediately below) as well. Thus, we denote the pre- and post- actuation time at any given j^{th} decomposition instant as $\mathbb{T}_{pa,j}$ and $\mathbb{T}_{pst,j}$, respectively.

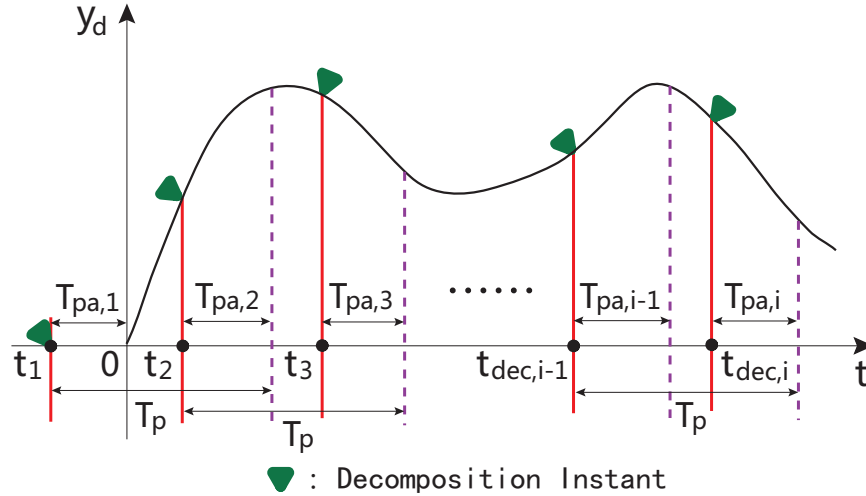


Figure 3.1: The proposed control scheme: The red-vertical lines and the big green arrows denote the decomposition instants (i.e., the time instants at which the decomposition–synthesis process occur). At each decomposition instant, the part of the previewed desired output trajectory to be decomposed is marked by the two right ahead adjacent purple-dashed lines, where $\mathbb{T}_{pa,j}$ s for $j = 1, 2, \dots$ denote the corresponding pre-actuation times, and T_p is the preview time.

Definition 2 For given preview time T_p and pre-actuation time $\mathbb{T}_{pa,j}$, the j^{th} **decomposition**

instant, $t_{dec,j}$, is the time instant at which the previewed desired trajectory $y_d(t)$ for $t \in [t_{dec,j} + \mathbb{T}_{pa,j}, t_{dec,j} + T_p]$ is decomposed, and is given by (see Fig. 4.2)

$$t_{dec,j} = t_{dec,j-1} + T_p - \mathbb{T}_{pa,j}, \quad \text{for } j > 1, \quad (3.7)$$

and $t_{dec,1} = 0$ initially.

Assumption 6 At any decomposition instant $t_{dec,j}$ for $j = 1, 2, \dots$, the available preview time T_p is greater than the required pre-actuation time $\mathbb{T}_{pa,j}$, i.e.,

$$T_p > \mathbb{T}_{pa,j} \quad \forall j = 1, 2, \dots \quad (3.8)$$

We present below the decomposition at the j^{th} decomposition instant $t_{dec,j}$ and consequently, the synthesis and update of the control input between the j^{th} and the $(j+1)^{th}$ decomposition instants. The added part of the previewed desired output trajectory, i.e., $y_d(t)$ for $t \in [t_{dec,j} + \mathbb{T}_{pa,j}, t_{dec,j} + T_p]$ (see Fig. 4.2), will be decomposed into (approximated by) a finite sum of the desired output elements with given desired precision ϵ_a , i.e., for the previewed desired output trajectory in the k^{th} channel, $y_{d,k}(\cdot)$ in

$$y_d(\cdot) = [y_{d,1}(\cdot) \ y_{d,2}(\cdot) \ \cdots \ y_{d,q}(\cdot)]^T, \quad (3.9)$$

we approximate $y_{d,k}(t)$ for $t \in [t_{dec,j} + \mathbb{T}_{pa,j}, t_{dec,j} + T_p]$ by

$$y_{d,k}(t) \approx \sum_{i=1}^{N_{d,k}} p_{k,i} y_{e,j}^*(t - t_{dec,j} - t_{sep,k,i}) \quad (3.10)$$

$$= \sum_{i=1}^{N_{d,k}} p_{k,i} y_{k,j}^*(t - t_{dec,j} - t_{sep,k,i}), \quad (3.11)$$

such that for any given j ,

$$\left(\int_{t_{dec,j} + \mathbb{T}_{pa,j}}^{t_{dec,j} + T_p} \mathbf{E}_{y,apox}(\tau)^2(d\tau) \right)^{1/2} \leq \epsilon_a, \quad \text{where} \quad (3.12)$$

$$\mathbf{E}_{y,apox}(t) \triangleq \left\| y_d(\tau) - \sum_{k=1}^q \sum_{i=1}^{N_{d,k}} p_{k,i} y_{k,j}^*(t - t_{dec,j} - t_{sep,k,i}) \right\|_2$$

where $y_{e,j}^*(\cdot)$ and $y_{k,j}^*(\cdot)$ are defined in (4.3), $p_{k,i} \in \Re$ are constant coefficients, and the positive constants $t_{sep,k,i} \geq 0$ denote any additional shift needed in the decomposition (e.g., when

the uniform B-splines are used to construct the library, see Sec. 3.2.3 later).

Online Input Synthesis

Based on the decomposition of the previewed desired output in Eq. (3.11), the desired input to track the added part of the previewed desired output is obtained as a linear combination of the corresponding input elements from the library \mathcal{L}_e , i.e., the desired input $u_d(t)$ to track $y_{d,k}(t)$ for $t \in [t_{dec,j} + \mathbb{T}_{pa,j}, t_{dec,j} + T_p]$ is synthesized as

$$u_{d,j}(t) = \sum_{k=1}^q \left(\sum_{i=1}^{N_{d,k}} p_{k,i} u_{k,i}^*(t - t_{dec,j} - t_{sep,k,i}) \right) \quad (3.13)$$

where $u_{k,i}^*(t) \in \mathbb{R}^{p \times 1}$ is given by (4.4). Note that the tracking of the original desired trajectory $y_d(\cdot)$ is guaranteed by the superimposition property of LTI systems (see (4.2)–(4.4)). Then for a given required tracking precision ϵ , the corresponding pre-actuation time $\mathbb{T}_{pa,j}$ and post-actuation time $\mathbb{T}_{pst,j}$ can be determined (discussed later in Sec. 4.2.2), and the truncated control input for tracking the decomposed part of the previewed desired output trajectory is obtained as

$$u_{trt,j}(t) = \mathcal{W}_{t_{j,1}, t_{j,2}}(t) u_{d,j}(t), \quad \text{for tracking} \quad (3.14)$$

$$y_{d,k} \in [t_{dec,j} + \mathbb{T}_{pa,j}, t_{dec,j} + T_p],$$

where $\mathcal{W}_{t_{j,1}, t_{j,2}}(\cdot)$ is the window function (i.e., $\mathcal{W}_{t_1, t_2}(t) = 1$ for $t \in [t_1, t_2]$, and $\mathcal{W}_{t_1, t_2}(t) = 0$ otherwise) with

$$t_{j,1} = t_{dec,j}, \quad t_{j,2} = t_{dec,j} + t_{j,\max} + \mathbb{T}_{pst,j},$$

and $t_{j,\max}$ is the upper bound of the supports of all the desired output elements involved in the j^{th} decomposition,

$$t_{j,\max} = \sup_k t_{k,j}. \quad (3.15)$$

The post-actuation time $\mathbb{T}_{pst,j}$ is needed as truncated B-splines (i.e., with none-zero starting or end value) are used in the approximation, and these truncated B-splines are smoothly extended and transited to zero to become the desired output elements in the Library (see Sec. 3.2.4).

Finally, the control input for $t \in [t_{dec,j}, t_{dec,j+1})$ is updated by

$$u_{pre,j}(t) = \begin{cases} u_{pre,j}(t) + u_{trt,j}(t), & t = t_{dec,j} \\ u_{pre,j}(t), & t \in (t_{dec,j}, t_{dec,j+1}) \end{cases} \quad (3.16)$$

and the previewed control input $u_{pre,j}(t)$ is applied to the system for $t \in [t_{dec,j}, t_{dec,j+1}]$.

Remark 9 *The proposed method can also be applied to trajectory planning applications, where the decomposition of the desired output trajectory and the synthesis of the control input are only needed once.*

3.2.3 B-spline-Based Desired Trajectory Decomposition

Next we describe decomposition based on B-splines. Although various function interpolation techniques can be employed for the decomposition (e.g., see textbook [51]), B-splines are chosen for their flexibility that results in a small size library of input-output elements.

B-spline-Based Trajectory Decomposition

The B-spline-based signal representation and approximation technique has been studied recently for control such as trajectory planning [52] and optimal control [53, 54]. We present below the construction of B-spline—for completeness—as in Ref. [55] by formulating the B-spline approximation as a LQ-optimal control problem.

With no loss of generality, we consider the decomposition of the k^{th} channel desired output trajectory for time $t \in I \triangleq [0, \mathbf{T}_d]$. By (3.10), the previewed desired output trajectory in the k^{th} channel can be approximated by

$$y_{d,k}(t) \approx \sum_{i=-s+1}^{m-1} p_{k,i} B_{i,s}(t) \triangleq p_{apx,k}(t) \quad (3.17)$$

where $B_{i,s}(t)$ are the s^{th} -degree basis functions, and $m \geq s + 2$ is the total number of knots with t_i s for $i = -s + 1, \dots, m - 1$, chosen as below in the approximation

$$0 \leq t_{-s+1} \leq t_{-s+2} \leq \dots \leq t_{m-1} \leq \mathbf{T}_d.$$

With the knots chosen as above, the B-spline basis functions are obtained by setting

$$B_{i,0}(t) = \begin{cases} 1, & \text{for } t_i \leq t < t_{i+1}, \\ 0, & \text{otherwise,} \end{cases} \quad (3.18)$$

and recursively by

$$B_{i,s}(t) = \frac{t - t_i}{t_{i+s} - t_i} B_{i,s-1}(t) + \frac{t_{i+s+1} - t}{t_{i+s+1} - t_{i+1}} B_{i+1,s-1}(t), \quad (3.19)$$

$$i = -s + 1, -s + 2, \dots, m - 1.$$

For given degree and knots number of B-splines, the total number of B-splines used in the approximation $N_{d,k}$ is then given by

$$N_{d,k} = m + s - 1 \geq 2s + 1 \quad (3.20)$$

We assume that there are N_B number of sampled desired output values used in the above approximation, i.e., we select $\{y_{d,k}(\gamma_1), y_{d,k}(\gamma_2), \dots, y_{d,k}(\gamma_{N_B})\}$ with

$$0 \leq \gamma_1 \leq \gamma_2 \leq \dots \leq \gamma_{N_B} \leq \mathbf{T}_d.$$

Then, the approximation problem in (4.11) can be formulated as an optimal control problem,

$$\min_{P_k \in \mathfrak{R}^{N_{d,k}}} J(\gamma), \quad \text{where} \quad (3.21)$$

$$J(\gamma) \triangleq \int_I \lambda (p_{apx,k}^{(2)}(t))^2 dt + \sum_{j=1}^{N_B} w_j (p_{apx,k}(\gamma_j) - y_{d,k}(\gamma_j))^2,$$

where

$$P_k = [p_{k,-s+1} \ p_{k,-s+2} \ \dots \ p_{k,m-1}]^T, \quad (3.22)$$

$$\gamma = \{\gamma_1 \ \gamma_2 \ \dots \ \gamma_{N_B}\}^T,$$

and $\lambda > 0$ and $w_j \in [0, 1]$ for $\forall j$ are the weights. The solution to the above optimization problem is given by

$$P_k^* = (\lambda Q + M^T W M)^{-1} M^T W \zeta_{y,k} \quad (3.23)$$

where

$$\zeta_{y,k} = [y_{d,k}(\gamma_1) \ y_{d,k}(\gamma_2) \ \dots \ y_{d,k}(\gamma_{N_B})]^T, \quad (3.24)$$

$$W = \text{diag}([w_1 \ w_2 \ \dots \ w_{N_B}]), \quad (3.25)$$

and

$$Q = [q_{k_r, k_c}] \in \mathbb{R}^{N_{d,k} \times N_{d,k}}, \quad (3.26)$$

with $k_r, k_c = -s + 1, -s + 2, \dots, m - 1$, and

$$q_{k_r, k_c} = \int_I B_{i,s}^{(2)}(t) B_{j,s}^{(2)}(t) dt. \quad (3.27)$$

Furthermore, the matrix $M \in \mathbb{R}^{N_B \times N_{d,k}}$ is given by

$$B = \begin{bmatrix} B_{-s+1,s}(\gamma_1) & B_{-s+2,s}(\gamma_1) & \cdots & B_{m-1,s}(\gamma_1) \\ B_{-s+1,s}(\gamma_2) & B_{-s+2,s}(\gamma_2) & \cdots & B_{m-1,s}(\gamma_2) \\ \vdots & \vdots & \vdots & \vdots \\ B_{-s+1,s}(\gamma_{N_B}) & B_{-s+2,s}(\gamma_{N_B}) & \cdots & B_{m-1,s}(\gamma_{N_B}) \end{bmatrix} \quad (3.28)$$

Note that in solution (4.14), all the matrices (vectors) except the sampled values of the desired output in (4.15) are known *a priori*, as usually the preview time T_p , the degree and the number of the B-splines s and $N_{d,k}$, respectively, and the number of sampled values used in the approximation N_B are given. Therefore, the previewed output trajectory can be effectively decomposed online.

Uniform B-splines The uniform B-splines, obtained when the knots selected are evenly spaced within the time interval, i.e., $t_{i+1} - t_i = \mathbf{T}_d / (m - 1)$ for $i = 0, \dots, m - 2$ in (4.5), possess two features particularly useful to reduce the number of elements in the library \mathcal{L}_e : (1) The obtained B-splines are nothing but time-shift copies of each other, with the shift time given by the spacing between two successive knots, i.e., the time-shift $t_{sep,j}$ in (3.10) is the same, and is given by

$$t_{sep,k,i} = t_{i+1} - t_i = \frac{\mathbf{T}_d}{m - 1} = \Delta t_{sep,j}, \quad \text{for } i = 0, 1, \dots, m - 2. \quad (3.29)$$

(2) The truncation points of the truncated B-spline basis are fixed and uniformly spaced. For example, for the 3^{rd} uniform B-splines, the truncation instants are at $s \times \Delta t_{sep,j}$ ($s = 1, 2, 3$) ahead or behind of the starting or the end instant of the basis function, respectively (see Fig. 4.1). For example, when the 3^{th} B-splines are used, the library \mathcal{L}_e only consists of seven elements of input-output pairs (see Fig. 4.1). Due to these advantages, we assume (the results below, however, also hold when non-uniform B-splines used with very minor changes):

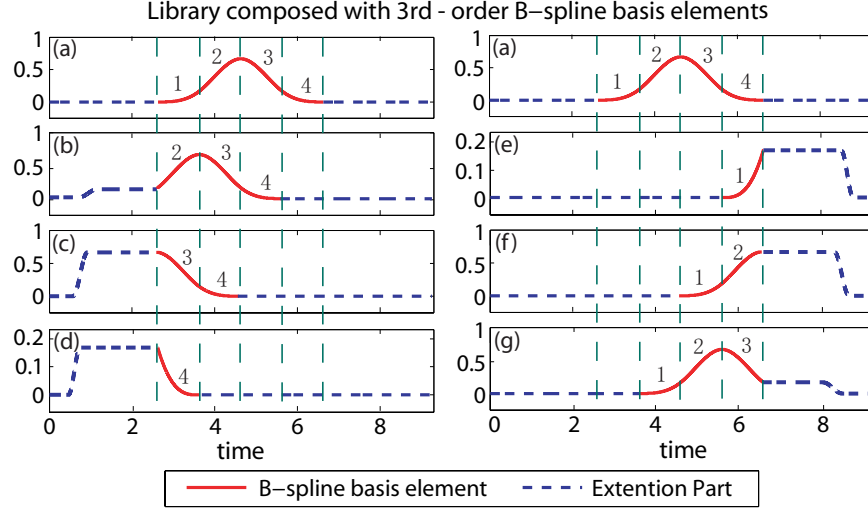


Figure 3.2: The desired output elements in the library \mathcal{L}_e generated by using the 3^{rd} -degree uniform B-spline basis function and its truncated version.

Assumption 7 The output elements $y_{e,i}^*$ for $i = 1, 2, \dots, N_L$ in the library \mathcal{L}_e are generated from the s^{th} -degree of uniform B-splines with $s \geq r_{\max} + 1$, where $r_{\max} = \max_k r_k$ is the highest relative degree among all output channels.

In light of Assumption 5, the degree requirement in the above Assumption 7 is needed as the s^{th} -degree B-splines is up to $s - 1$ order continuously differentiable.

In the following, we denote, respectively, the subset of output elements obtained from untruncated B-spline elements, and those of truncated-B-spline elements with extension at the beginning or at the end, as \mathbb{B}_o , \mathbb{B}_{be} , and \mathbb{B}_{fe} , respectively.

3.2.4 Output Elements Extension and Input Elements Approximation

To ensure precision tracking, the desired output elements used in the decomposition needs to be sufficiently smooth [3]. This smoothness requirement implies that the truncated B-splines cannot be used directly as the desired output elements. Thus, the following output-extension-input-approximation scheme is proposed to address this issue.

Output Elements Extension The output elements in the library generated by truncated B-splines with non-zero starting values, are obtained via extension and smooth transition as follows: $y_{e,i}^*(\cdot) \in \mathbb{B}_{be}$ are given by

$$y_{e,i}^*(t) = \begin{cases} 0 & t < -3\mathbb{T}_{pa}^* \\ \mathcal{T}_{e,i}(t) & t \in [-3\mathbb{T}_{pa}^*, -2\mathbb{T}_{pa}^*], \\ y_{e,i}^*(0) & t \in (-2\mathbb{T}_{pa}^*, 0), \\ y_{e,i}^*(t) & t \in [0, t_i] \end{cases} \quad (3.30)$$

where \mathbb{T}_{pa}^* is the maximum pre-actuation time large enough to guarantee the tracking precision for all tracking in the given application, $\mathcal{T}_{e,i}(\cdot)$ denotes a smooth function to transit the output element $y_{e,i}^*(t)$ from 0 to the truncated value at $y_{e,i}^*(0)$ (e.g., an exponential function). Finally, the above extended and transited output elements are filtered to render the element $y_{e,i}^*(\cdot)$ around the extension points smooth enough while keeping the filtering-caused deviation small enough to meet Assumption 5 (e.g., by using a high-order noncausal low-pass filter).

Similarly, the output elements in the library generated from truncated B-splines with non-zero ending values, are obtained via extension and smooth transition as follows for $t > t_i$, for $y_{e,i}^*(\cdot) \in \mathcal{B}_{fe}$,

$$y_{e,i}^*(t) = \begin{cases} y_{e,i}^*(t) & t \in [0, t_i), \\ y_{e,i}^*(t_i) & t \in (t_i, t_i + 2\mathbb{T}_{pst}^*), \\ \mathcal{T}_{e,i}(t) & t \in [t_i + 2\mathbb{T}_{pst}^*, t_i + 3\mathbb{T}_{pst}^*], \\ 0 & t > t_i + 3\mathbb{T}_{pst}^* \end{cases} \quad (3.31)$$

where \mathbb{T}_{pst}^* is the maximum post-actuation time (quantification of \mathbb{T}_{pa}^* and \mathbb{T}_{pst}^* is addressed in Sec. 4.2.2). As an example, the output elements obtained through the above extension scheme are plotted in Fig. 4.1 for the 3th-degree B-splines case.

Input Elements Approximation As shown by the stable-inversion theory [3] and discussed immediately in Sec. 4.2.2, the control input element for the above smoothly-extended output element exponentially approaches to a constant during the extension period of the output elements (see Fig. 4.1). Thus, at any given j^{th} decomposition instant, the input element $u_{k,i}^*(t)$ (corresponding to the i^{th} output element used in the decomposition of the k^{th} channel of the desired output) are approximated as a constant for time greater than an half of the extension

time window, i.e.,

$$u_{k,i}^*(t) = \begin{cases} u_{k,i}^*(-\mathbb{T}_{pa,j}), & \text{for } t \in [-2\mathbb{T}_{pa,j}, -\mathbb{T}_{pa}^*], \\ u_{k,i}^*(t_{k,i} + \mathbb{T}_{pst}^*), & \text{for } t \geq t_i + \mathbb{T}_{pst,j} \end{cases} \quad (3.32)$$

Offset of the Previewed Output for Decomposition At each decomposition instant, the previewed desired output to be decomposed is offsetted to start at zero.

3.2.5 Quantification of the Pre- and Post-Actuation Times

Next, we quantify the pre- and post-actuation times. We start the quantification for each desired output element first, then for tracking after only one decomposition instant, and finally, for tracking after any given number of decomposition instants. To begin with, we represent system (3.1) in the output tracking form.

Output Tracking Form [36] Under Assumptions 4, 5, system (3.1) can be transformed to the following output tracking form through a state transformation $\Gamma : \mathbb{R}^n \rightarrow \mathbb{R}^n$

$$x(t) = \Gamma \begin{bmatrix} \xi(t) \\ \eta_s(t) \\ \eta_u(t) \end{bmatrix} = [\Gamma_\xi \ \Gamma_{\eta,s} \ \Gamma_{\eta,u}] \begin{bmatrix} \xi(t) \\ \eta_s(t) \\ \eta_u(t) \end{bmatrix}, \quad (3.33)$$

along with the inverse control input $u_{inv}(\cdot)$

$$u_{inv}(t) = \mathbf{M}_Y \mathbb{Y}_d(t) + \mathbf{M}_s \eta_s(t) + \mathbf{M}_u \eta_u(t), \quad (3.34)$$

such that

$$\begin{aligned} \dot{\xi}(t) &= \dot{\xi}_d(t), \\ \dot{\eta}_s(t) &= A_s \eta_s(t) + B_s \mathbb{Y}_d(t), \\ \dot{\eta}_u(t) &= A_u \eta_s(t) + B_u \mathbb{Y}_d(t). \end{aligned} \quad (3.35)$$

where

$$\xi(t) = \left[y_1, \dot{y}_1, \dots, \frac{d^{r_1-1}y_1}{dt^{r_1-1}}, y_2, \dot{y}_2, \dots, \frac{d^{r_2-1}y_2}{dt^{r_2-1}}, \dots, y_p, \dot{y}_p, \dots, \frac{d^{r_p-1}y_p}{dt^{r_p-1}} \right]^T \quad (3.36)$$

is the output and its derivatives, and

$$\mathbb{Y}_d(t) = \begin{bmatrix} \xi_d(t) & y_d^{(r)}(t) \end{bmatrix}^T. \quad (3.37)$$

In (3.35), $\eta_s(\cdot)$ and $\eta_u(\cdot)$ are the stable and the unstable internal dynamics [36], respectively, i.e., all the eigenvalues of A_s and A_u are on the open left hand side and the open right hand side of the complex plane, respectively. Particularly, the stable and unstable internal dynamics are solved by flowing the state forward and backwards in time, respectively, i.e.,

$$\begin{aligned}\eta_s(t) &= \mathcal{L}_s(0, t, \mathbb{Y}_{k,i}(\cdot)), \\ \eta_u(t) &= \mathcal{L}_u(t, \infty, \mathbb{Y}_{k,i}(\cdot)),\end{aligned}\tag{3.38}$$

where

$$\begin{aligned}\mathcal{L}_s(t_\ell, t_\mu, U(\cdot)) &\triangleq \int_{t_\ell}^{t_\mu} e^{A_s(t_\mu - \tau)} B_s U(\tau) d\tau \\ \mathcal{L}_u(t_\ell, t_\mu, U(\cdot)) &\triangleq - \int_{t_\ell}^{t_\mu} e^{-A_u(\tau - t_\ell)} B_u U(\tau) d\tau\end{aligned}\tag{3.39}$$

The above (3.38) implies that in general, infinite pre- and post-actuation is needed to achieve exact tracking of nonminimum-phase systems [26, 23]. Moreover, for systems satisfying Assumption 4, the control input to achieve exact tracking of a given desired output trajectory is unique [3] — regardless of the method used to obtain the desired input element $u_{k,i}^*(\cdot)$. Thus, truncation to a finite pre- and post-actuation time is needed when using the desired input elements to synthesize the input (see Sec. 4.2.1 and (4.22)).

The Lemma below quantifies the pre- and post-actuation time for one output element in the library \mathbb{L}_e .

Lemma 5 *Let Assumptions 4, 5, 6, and 7 be satisfied, and let $y_{k,i}^*(\cdot)$ be any given output element in the library \mathcal{L}_e as specified by (4.3). Then the error due to a finite pre- and post-actuation time, $T_{pa,i}$ and $T_{pst,i}$ respectively, in the tracking of $y_{k,i}^*(\cdot)$, $\|e_{y,i}(t)\|_2$, is bounded as*

$$\|e_{y,i}(t)\|_2 \leq \begin{cases} \mathbf{Y}_{e,i}^\infty [\mathcal{E}_{y,i}(t, T_{pa,i}, T_{pst,i}) + \\ \mathcal{K}_{a,s} e^{-(\alpha+\lambda)T_{pa,i}-\lambda t}], & y_{e,i}^*(\cdot) \in \mathbb{B}_{be} \\ \mathbf{Y}_{e,i}^\infty \mathcal{E}_{y,i}(t, T_{pa,i}, T_{pst,i}), & y_{e,i}^*(\cdot) \in \mathbb{B}_o \\ \mathbf{Y}_{e,i}^\infty [\mathcal{E}_{y,i}(t, T_{pa,i}, T_{pst,i}) + \Lambda(\mathcal{K}_{t,u}, \hat{\mathcal{K}}_{t,u}, t) \\ e^{-\beta T_{pst,i}}], & y_{e,i}^*(\cdot) \in \mathbb{B}_{fe} \end{cases} \quad (3.40)$$

for $t \geq 0$, where

$$\begin{aligned} \mathbf{Y}_{e,i}^\infty &\triangleq \sup_{\tau} \|\mathbb{Y}_{e,i}(\tau)\|_\infty, \\ \mathcal{E}_{y,i}(t, T_{pa,i}, T_{pst,i}) &\triangleq \left\{ \mathcal{K}_{a,u} e^{-(\beta+\lambda)T_{pa,i}-\lambda t} + \Lambda(\mathcal{K}_{t,s}, \hat{\mathcal{K}}_{t,s}, t) e^{-\alpha T_{pst,i}} \right\} \end{aligned} \quad (3.41)$$

with

$$\Lambda_0(K_1, K_2, t) \triangleq (K_1 - K_2 e^{-\lambda t}) \mu(t - t_{k,i} - T_{pst,i}), \quad (3.42)$$

$\mu(t)$ is the unit step function, and

$$\begin{aligned} \mathcal{K}_{a,s} &\triangleq \frac{2}{\alpha} M_A M_{A_s} \|\Gamma_{\eta,s}\|_2 \|B_s\|_2 \|C\|_2, \\ \mathcal{K}_{a,u} &\triangleq \frac{1}{\beta} M_A M_{A_u} \|\Gamma_{\eta,u}\|_2 \|B_u\|_2 \|C\|_2, \\ \mathcal{K}_{t,s} &\triangleq \frac{1 + M_{A_s}}{\alpha \lambda} M_A M_{A_s} \|\mathbf{M}_s\|_2 \|B_s\|_2 \|B\|_2 \|C\|_2, \\ \hat{\mathcal{K}}_{t,s} &\triangleq \mathcal{K}_{t,s} e^{\lambda(t_{k,i} + T_{pst,i})}, \\ \mathcal{K}_{t,u} &\triangleq \frac{2}{\beta \lambda} M_A M_{A_u} \|\mathbf{M}_u\|_2 \|B_u\|_2 \|B\|_2 \|C\|_2, \\ \hat{\mathcal{K}}_{t,u} &\triangleq \mathcal{K}_{t,u} e^{\lambda(t_{k,i} + T_{pst,i})}, \end{aligned} \quad (3.43)$$

where the constants M_A , M_{A_u} , α and β satisfy the following Hurwitz matrix inequality.

$$\|e^{At}\|_2 \leq M_A e^{-\lambda t}, \quad \|e^{A_s t}\|_2 \leq M_{A_s} e^{-\alpha t}, \quad \|e^{-A_u t}\|_2 \leq M_{A_u} e^{-\beta t} \quad (3.44)$$

Proof: We first consider the output elements obtained from un-truncated B-splines, i.e., $y_{e,i}^*(\cdot) \in \mathbb{B}_o$, and quantify the error due to the finite pre-actuation only—the error due to the post-actuation is obtained via superimposition. Note that in this case the input element equals

to the exact-tracking input for time $t > -T_{pa,i}$, and the tracking error is caused by the state error at time instant $-T_{pa,i}^j$ [26, 23]. Thus, by (4.21), (4.22), the finite-truncation caused error of the system state at any time instant $t \geq -T_{pa,i}$ is given by:

$$e_{x,i}^*(t) \triangleq x_{e,i}^*(t) - x_{p,i}(t) = e^{A(T_{pa,i}+t)} x_{e,i}^*(-T_{pa,i}) \quad (3.45)$$

By (3.33), the state value can be further represented by the output (and its derivatives) and the internal dynamics. Particularly, for the desired output elements considered in this chapter (see (4.10)), $\xi_d(t) = 0$ and $\eta_s(t) = 0$ for $t \leq 0$. Thus, by (3.33), (3.38),

$$\begin{aligned} e_{x,i}^*(t) &= e^{A(T_{pa,i}+t)} \Gamma_{\eta,u} \eta_u(-T_{pa,i}) \\ &= e^{A(T_{pa,i}+t)} \Gamma_{\eta,u} \mathcal{L}_u(-T_{pa,i}, \infty, B_u \mathbb{Y}_{k,i}(\cdot)) \end{aligned} \quad (3.46)$$

Thus, the finite pre-actuation-caused tracking error for $y_{k,i}^*(\cdot) \in \mathbb{B}_o$ can be quantified similarly as the finite preview-time-caused tracking error, and is omitted.

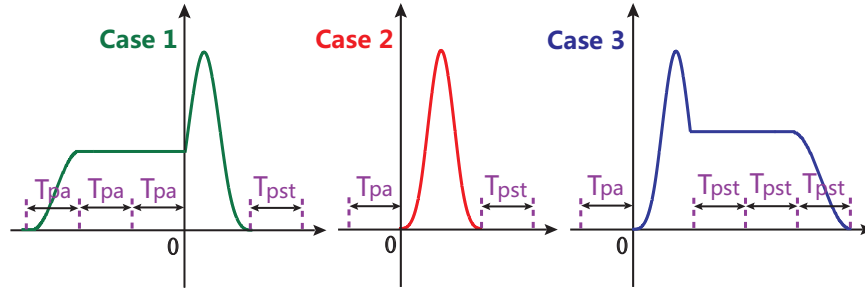


Figure 3.3: The pre- and post-actuation time, T_{pa} and T_{pst} for (2) the s^{th} -degree B-spline basis function, (1) the one truncated at the beginning, and (3) the one truncated at the end.

Secondly, by (3.47), (3.34), and (3.38), as $y_{k,i}(t) = 0$ for $t \geq t_{k,i}$, the finite post-actuation caused tracking-error for $\bar{e}_{k,i}^*(t)$ $t \geq t_{k,i} + T_{pst,i}$, is, in fact, due to approximating the inverse input its value at time instant $t_{k,i} + T_{pst,i}$, which, in turn, is caused by approximating the stable internal dynamics $\eta_s(t)$ with its value at $t_{k,i} + T_{pst,i}$, i.e., $\eta_s(t) \approx \eta_s(t_i + T_{pst,i})$ for $t \geq t_{k,i} + T_{pst,i}$. Thus,

$$\begin{aligned} \bar{e}_{x,i}^*(t) &= \int_{t_{k,i}+T_{pst,i}}^t e^{A(t-\tau)} B \bar{e}_{u,i}^*(\tau) d\tau, \quad \text{and,} \\ \bar{e}_{u,i}^*(t) &= \mathbf{M}_s(\eta_s(t) - \eta_s(t_i + T_{pst,i})) \\ &= e^{AsT_{pst,i}} [(e^{As\Delta t} - 1)\eta_s(t_{k,i})] \quad (\Delta t \triangleq t - t_{k,i} - T_{pst,i}) \end{aligned} \quad (3.47)$$

where the boundary values $\eta_s(t_{k,i})$ can be further bounded as

$$\|\eta_s(t_i)\|_2 \leq \frac{1}{\alpha} \|B_s\|_2 \sup_{\tau} \|Y_{k,i}(\tau)\|_{\infty}, \quad (3.48)$$

This shows the second formula in (3.40).

Next we consider the output elements obtained from truncated-at-the-beginning the proof is obtained to quantify the B-splines, i.e., $y_{k,i}^*(\cdot) \in \mathbb{B}_{be}$. The finite post-actuation caused error for these elements is the same as that for those from untruncated B-splines. Whereas the finite pre-actuation-caused state error is given by the sum of the state error at time instant $t_{pa,k,i}$ and the input error for $t \geq T_{pa,i}$ (due to the transition of the extension to zero, see Fig. 4.1), i.e.,

$$e_{x,i}^*(t) = e^{A(T_{pa,i}+t)} e_{x,i}(-T_{pa,i}) + \int_{-T_{pa,i}}^t e^{A(t-\tau)} B e_{u,k,i}(\tau) d\tau \quad (3.49)$$

Note that the first error term on the r.h.s. can be bounded the same as that for the un-truncated B-spline elements. And by (3.34) (3.38), the input error in the above (3.49) comes from the error of the stable internal dynamics $\eta_s(t)$ for $t \leq -T_{pa,i}$ caused by the replacement of the constant desired output with the smooth transition to zero, i.e., for $t \geq -T_{pa,i}$

$$\begin{aligned} e_{u,k,i}(t) &= M_s e_{\eta,s}(t), \quad \text{with} \\ e_{\eta,s}(t) &= e^{A_s(T_{pa,i}+t)} e_{\eta,s}(-T_{pa,i}) \\ &= e^{A_s(T_{pa,i}+t)} \left[\mathcal{L}_s(-\infty, -3T_{pa,i}, \mathbb{Y}_d(0)) + \mathcal{L}_s(-3T_{pa,i}, -2T_{pa,i}, (\mathbb{Y}_d(0) - \hat{\mathbb{Y}}_d(t))) \right], \end{aligned} \quad (3.50)$$

It can be verified that the above $\mathcal{L}_s(-\infty, -3T_{pa,i}, \mathbb{Y}_d(0))$ and $\mathcal{L}_s(-3T_{pa,i}, -2T_{pa,i}, (\mathbb{Y}_d(0) - \hat{\mathbb{Y}}_d(t)))$ (as defined in (3.39)) can be quantified similarly as those for the case of $y_{k,i}(\cdot) \in \mathbb{B}_0$. This shows the first formula in (3.40).

Finally, we consider the output elements obtained from truncated-at-the-end B-splines, i.e., $y_{k,i}^*(\cdot) \in \mathbb{B}_{fe}$. Note for these elements the finite pre-actuation caused error is the same as that of elements from untruncated B-splines, and the post-actuation-caused state error consists of errors caused by (1) the replacement of a constant desired output with the smooth transition to zero, and (2) the replacement of the input for $t \geq t_{k,i} + T_{pst,i}$ by the constant equaling to the input value at time instant $t_{k,i} + T_{pst,i}$,

$$e_{u,i}(t) = \begin{cases} \mathbf{M}_u e^{A_u(t_{k,i}+T_{pst,i}-t)} e_{\eta,u}(t_{k,i} + T_{pst,i}) & t \leq t_{k,i} + T_{pst,i} \\ \mathbf{M}_s \bar{e}_{\eta,s}(t) + \mathbf{M}_u e_{\eta,u}(t_{k,i} + T_{pst,i}) & t > t_{k,i} + T_{pst,i} \end{cases} \quad (3.51)$$

where

$$\begin{aligned}
e_{\eta,u}(t_{k,i} + T_{pst,i}) &= \mathcal{L}_u(t_{k,i} + 3T_{pst,i}, \infty, \mathbb{Y}_{k,i}^*(t_{k,i})) \\
&\quad + \mathcal{L}_u(t_{k,i} + 3T_{pst,i}, t_{k,i} + 2T_{pst,i}, \left(\mathbb{Y}_{k,i}^*(t_{k,i}) - \hat{\mathbb{Y}}_{k,i}^*(t) \right)) \\
\bar{e}_{\eta,s}(t) &= \eta_s(t) - \eta_s(t_i + T_{pst}) \\
&= \mathcal{L}_s(t_{k,i}, t, \mathbb{Y}_{k,i}^*(t_{k,i})) - \mathcal{L}_s(t_{k,i}, t_{k,i} + T_{pst,i}, \mathbb{Y}_{k,i}^*(t_{k,i}))
\end{aligned} \tag{3.52}$$

Thus, the error terms $e_{\eta,u}(t_{k,i} + T_{pst,i})$ and $\bar{e}_{\eta,s}(t)$ can be quantified similarly as above. This finishes the proof. \blacksquare

Next, we consider the tracking error at any given j^{th} decomposition instant due to the finite pre- and post-actuation of the synthesized input $u_{trt}(t)$ obtained from the decomposition of $y_d(t)$ with $t \in [t_{dec,j} + T_{pa,j}, t_{dec,j} + T_p)$. For clarification, for any given k^{th} ($k = 1, 2, \dots, q$) output channel we order the output elements by the time they first appear in the decomposition of the previewed desired output in that channel $y_{d,k}(\cdot)$, and denote, for the i^{th} output element, the pre- and post-actuation times as $T_{pa,k,i}^j$ and $T_{pst,k,i}^j$, respectively.

Theorem 2 *Let conditions in Lemma 5 be satisfied, and at any given j^{th} decomposition time instant $t_{dec,j}$, let the previewed desired output $y_{d,k}(t)$ for $t \in [t_{dec,j} + T_{pa,k,j}, t_{dec,j} + T_p]$ and $k = 1, 2, \dots, q$ be given, and be decomposed into $N_{d,k}^j$ number of desired output elements generated by the s^{th} -degree B-splines. Then the finite pre- and post-actuation caused output tracking error can be bounded as*

$$\|e_y(t)\|_2 = \left(\sum_{k=1}^q (\|e_{y,k}(t)\|_2)^2 \right)^{1/2}, \tag{3.53}$$

where for $k = 1, \dots, q$,

$$\begin{aligned}
\|e_{y,k}(t)\|_2 &\leq \hat{\mathbf{Y}}_{j,k}^\infty \left\{ \mathbb{K}_1 e^{-\beta T_{pa,k,1}^j} e^{-\lambda(T_{pa,k,1}^j + t)} \right. \\
&\quad \left. + \left[\Lambda_1(\mathbb{K}_2, \mathbb{K}_3, t) e^{-\beta T_{pst,k,N_{d,k}}^j} + \Lambda_1(\mathbb{K}_4, \mathbb{K}_5, t) e^{-\alpha T_{pst,k,N_{d,k}}^j} \right] \right\}.
\end{aligned} \tag{3.54}$$

where $\Lambda_1(\cdot, \cdot, \cdot)$ has the same structure as $\Lambda_0(\cdot, \cdot, \cdot)$ in (4.27) with the step function $\mu(\cdot)$ replaced by $\mu(t - T_p + T_{pa,k,1}^j - T_{pst,k,N_{d,k}}^j)$, $T_{pa,k,1}^j$ and $T_{pst,k,N_{d,k}}^j$ are the pre-actuation time of the first input element and the post-actuation time of the last input element involved in the decomposition, respectively,

$$\hat{\mathbf{Y}}_{j,k}^\infty = \sup_i |p_{k,i}| \mathbf{Y}_{e,i}^\infty, \quad i = 1, 2, \dots, N_{d,k}, \tag{3.55}$$

with $\mathbf{Y}_{e,i}^\infty$ given by (3.41), and for $j = 1, \dots, 5$, \mathbb{K}_j s are given by

$$\begin{aligned}
 \mathbb{K}_1 &= (s+1)\mathcal{K}_{a,u}, \quad \mathbb{K}_2 = s\mathcal{K}_{t,u}, \quad \mathbb{K}_3 = s\hat{\mathcal{K}}_{t,u}, \\
 \mathbb{K}_4 &= \mathcal{K}_{t,s} \sum_{i=N_{d,k}-s+1}^{N_{d,k}^j} e^{-\beta\Gamma_i} + \mathcal{K}_{t,s} \sum_{i=s+1}^{N_{d,k}-s} e^{-\alpha\Gamma_i} + s\mathcal{K}_{t,s}, \\
 \mathbb{K}_5 &= \mathcal{K}_{t,s} \sum_{i=N_{d,k}-s+1}^{N_{d,k}} e^{-\beta\Gamma_i + \lambda(T_{pst,k,N_{d,k}^j} + T_p - \Omega_i)} \\
 &\quad + \mathcal{K}_{t,s} \sum_{i=s+1}^{N_{d,k}-s} e^{-\alpha\Gamma_i + \lambda(T_{pst,k,N_{d,k}} + T_p - \Omega_i)} + s\hat{\mathcal{K}}_{t,s}.
 \end{aligned} \tag{3.56}$$

where $\mathcal{K}_{a,u}$, $\mathcal{K}_{t,s}$, $\hat{\mathcal{K}}_{t,s}$, $\mathcal{K}_{t,u}$ and $\hat{\mathcal{K}}_{t,u}$ are given by (3.43), and

$$\Gamma_i \triangleq (N_{d,k}^j - i - 1)\Delta t_{sep,j}, \quad \Omega_i \triangleq (i - 1)\Delta t_{sep,j}. \tag{3.57}$$

with $\Delta t_{sep,i}$ given by (4.7).

Proof By superposition, the proof is obtained to quantify the tracking error caused by finite pre- and post-actuation time in one output channel, i.e., for any given $k = 1, \dots, q$, we consider the tracking error for

$$y_{d,k}(\cdot) = [0 \cdots y_{d,0,k}(\cdot) \cdots 0]^T, \tag{3.58}$$

where $y_{d,0,k}(\cdot) \in \mathfrak{R}$ denotes the desired output trajectory in the k^{th} channel. Note for the $N_{d,k}^j$ number of output elements generated by the s^{th} -degree B-splines (employed in decomposing $y_{d,0,k}(\cdot)$), s number of output elements generated by the truncated-at-the-beginning B-splines are involved in decomposing $y_{d,0,k}(t)$ for $t \in [0, \Delta t_{sep,j})$, and s number of output elements generated by the truncated-at-the-end B-Splines are involved in decomposing $y_{d,0,k}$ for $t \in [t_k - \Delta t_{sep,j}, t_k]$, i.e.,

$$y_{k,i}^*(\cdot) \in \begin{cases} \mathbb{B}_{be}, & \text{for } i = 1, 2, \dots, s, \\ \mathbb{B}_o, & \text{for } i = s+1, \dots, N_{d,k}^j - s, \\ \mathbb{B}_{fe}, & \text{for } i = N_{d,k}^j - s+1, \dots, N_{d,k}^j. \end{cases} \tag{3.59}$$

Secondly, for the i^{th} output element ordered above, the pre-actuation time of $y_{k,i}^*(\cdot)$ for $i = s+1, \dots, N_{d,k}^j$ and the post-actuation time of $y_{k,i}^*(\cdot)$ for $i = 1, \dots, N_{d,k}^j - s$ are increased

by the separation time between the starting and the final time instants with respect to those of $y_{e,s+1}^*(\cdot)$ and $y_{e,N_k-s+1}^*(\cdot)$, respectively, i.e.,

$$\begin{aligned} T_{pa,k,i} &= \begin{cases} T_{pa,k,1}, & i = 1, \dots, s \\ T_{pa,k,1} + \Gamma_i, & i = s+2, \dots, N_{d,k}^j, \end{cases} \\ T_{pst,k,i} &= \begin{cases} T_{pst,k,N_{d,k}} + \Omega_i, & i = 1, \dots, N_{d,k}^j - s, \\ T_{pst,k,N_{d,k}}, & i = N_{d,k} - s + 1, \dots, N_{d,k}^j, \end{cases} \end{aligned} \quad (3.60)$$

where Γ_k and Ω_k are given in Eq. (3.57), respectively. Finally note that the previewed desired output trajectory to be decomposed always starts from zero, thereby, the weighted sum of the output elements involved in decomposing $y_{d,k}(t)$ around $t = 0$ equals to zero at $t = 0$,

$$\left. \sum_{i=1}^s p_{k,i} y_{e,i}^*(t) \right|_{t=0} = 0. \quad (3.61)$$

The above (3.61) implies that for minimum-phase systems, the finite pre-actuation time effect on the weighted sum of the input elements vanishes. Thus, the proof is completely by applying the superposition principle along with Eqs. (3.59), (3.60), (3.61) to Lemma (5). \blacksquare

As shown by (3.54), the finite pre- and post-actuation time caused tracking error exponentially depends on the length of the first pre- and the last post-actuation time, $T_{pa,k,1}$ and $T_{pst,k,N}$, respectively, and the above Theorem (2) shows that the required pre- and post-actuation times (for given tracking precision) are ultimately determined by the largest one (among all output channels) needed, respectively. Thus, at any given j^{th} decomposition instant the pre- and post-actuation times, $\mathbb{T}_{pa,j}$ and $\mathbb{T}_{pst,j}$, respectively, are related to those of output elements in the decomposition by

$$\mathbb{T}_{pa,j} = \max_k T_{pa,k,1}^j, \quad \mathbb{T}_{pst,j} = \max_k T_{pst,k,N_{d,k}}^j, \quad k = 1, 2, \dots, q, \quad (3.62)$$

and with no loss of generality, we assume

Assumption 8 *At any given decomposition instant, the pre- and post-actuation times, $T_{pa,k,1}^j$ and $T_{pst,k,N_{d,k}}^j$ are the same across all output channels.*

Finally, we consider the general case where prior to the current time instant t_c , there are m number of decomposition instants.

Theorem 3 Let conditions in Theorem (2) and Assumption (8) be satisfied, and at the current time instant t_c , there are m number of decomposition instants, $t_{dec,j}$ with $j = 1, \dots, m$, and at each $t_{dec,j}$, there are N_j number of the s^{th} -degree uniform B-splines based output elements used in the decomposition. Then the finite pre- and post- actuation caused output tracking error can be bounded as

$$\|E_y(t)\|_2 = \left(\sum_{k=1}^q (\|E_{y,k}(t)\|_2)^2 \right)^{1/2}, \quad (3.63)$$

where for $k = 1, \dots, q$, and $t > m(T_p - \mathbb{T}_{pa,m}^*)$,

$$\begin{aligned} \|E_{y,k}(t)\|_2 &\leq \hat{\mathbb{Y}}_{m,k}^\infty \left\{ \hat{\mathbb{K}}_1 e^{-(\beta \mathbb{T}_{pa,m}^* + \lambda t)} \right. \\ &\quad \left. + \left[\Lambda_2(m\mathbb{K}_2, \hat{\mathbb{K}}_3, t) e^{-\beta \mathbb{T}_{pst,m}^*} + \Lambda_2(m\mathbb{K}_4, \hat{\mathbb{K}}_5, t) e^{-\alpha \mathbb{T}_{pst,m}^*} \right] \right\} \end{aligned} \quad (3.64)$$

where for $j = 1, 2, \dots, m$,

$$\begin{aligned} \hat{\mathbb{Y}}_{m,k}^\infty &= \max_j \hat{\mathbb{Y}}_{j,k}^\infty, & \mathbb{T}_{pa,m}^* &= \min_j \{\mathbb{T}_{pa,j}\}, \\ \mathbb{T}_{pst,m}^* &= \min_j \{\mathbb{T}_{pst,j}\}, & \hat{\mathbb{K}}_1 &= \mathbb{E}_{T_p, T_{pa}} \mathbb{K}_1, \quad \text{and} \end{aligned} \quad (3.65)$$

$$\hat{\mathbb{K}}_3 = \mathbb{E}_{T_p, T_{pa}} \mathbb{K}_3, \quad \hat{\mathbb{K}}_5 = \mathbb{E}_{T_p, T_{pa}} \mathbb{K}_5, \quad \text{with} \quad (3.66)$$

$$\mathbb{E}_{T_p, T_{pa}} = \frac{1 - e^{m(T_p - \mathbb{T}_{pa,m}^*)\lambda}}{1 - e^{(T_p - \mathbb{T}_{pa,m}^*)\lambda}}, \quad (3.67)$$

and $\Lambda_2(\cdot, \cdot, \cdot)$ has the same structure as $\Lambda_0(\cdot, \cdot, \cdot)$ in (4.27) with the step function $\mu(\cdot)$ replaced by $\mu(t - T_p + \mathbb{T}_{pa,tot,m} - \mathbb{T}_{pst,k})$, with

$$\mathbb{T}_{pa,tot,m} = \sum_{j=1}^m \mathbb{T}_{pa,j},$$

and $\mathcal{K}_{a,s}$, $\mathcal{K}_{a,u}$, $\mathcal{K}_{t,s}$ and $\mathcal{K}_{t,u}$ given by (3.43), and \mathbb{K}_i s for $i = 1, 2, 3, 4$ defined in (3.56), respectively.

Proof: Similar to the proof of Theorem 2, we consider the pre- and post-actuation effect on one output channel, i.e., the k^{th} output channel for $k = 1, 2, \dots, q$. Note that at the current time instant t_c , the actual effect time of the finite pre-actuation related to the p^{th} decomposition instant (for $p \leq m$) is given by (i.e., replace t in the expression on the right side of (3.54) with $t_{act,p}$ given below),

$$t_{act,p} = t - pT_p - \sum_{j=1}^p \mathbb{T}_{pa,j-1} \quad (\text{with } \mathbb{T}_{pa,0} = 0.) \quad (3.68)$$

By applying the superposition principle to Theorem (2) along with (3.68), the total pre-actuation caused tracking error is given by

$$\begin{aligned}
\|E_y(t)\|_2 &\leq \mathbb{K}_1 \sum_{p=1}^m \hat{\mathbf{Y}}_{p,k}^\infty e^{-\beta T_{pa,k,1}^p} e^{-\lambda(T_{pa,k,1}^p + t_{act,p})} \\
&\leq \hat{\mathbf{Y}}_{m,k}^\infty \mathbb{K}_1 e^{-\beta \mathbb{T}_{pa}^* - \lambda(\mathbb{T}_{pa}^*)} \sum_{p=1}^m e^{-\lambda(t - p(T_p + \mathbb{T}_{pa}^*))} \\
&\quad (\text{By (4.26), (3.66), and (3.68), and Assumption (8), along with } t \geq m(T_p - \mathbb{T}_{pa,m}^*)) \\
&\leq \hat{\mathbf{Y}}_k^\infty \mathbb{K}_1 \mathbb{E}_{T_p, T_{pa}} e^{-(\beta \mathbb{T}_{pa,m}^* + \lambda t)}
\end{aligned} \tag{3.69}$$

Similarly, note that at the current time instant t_c , the actual effect time of the post pre-actuation related to the p^{th} decomposition instant (for $p \leq m$), embedded in $\Lambda_2(\cdot, \cdot, \cdot)$, is also given by (3.68) (i.e., replace t on the right side of (4.27) with $t_{act,p}$ in (3.68)). Hence by the superposition principle again, the total post-actuation caused tracking error can be bounded as

$$\begin{aligned}
\|E_y(t)\|_2 &\leq \sum_{p=1}^m \left\{ \hat{\mathbf{Y}}_{p,k}^\infty \left[\mathbb{K}_2 - \mathbb{K}_3 e^{-\lambda t_{act,p}} \right] e^{-\alpha T_{pst,k,N_d,k}^p} \right. \\
&\quad \left. + \left[\mathbb{K}_4 - \mathbb{K}_5 e^{-\lambda t_{act,p}} \right] e^{-\beta T_{pst,k,N_d,k}^p} \right\}
\end{aligned} \tag{3.70}$$

Thus, the finite post-actuation caused tracking error can be bounded similarly as shown in (3.69), by applying (3.66) (3.68) to the above (3.70). And the proof is completed by combining with (3.69). \blacksquare

Quantification for Practical Implementation In practical implementations, although the input elements for exact tracking of the desired output elements cannot be obtained—due to, e.g., the presence of inevitable noise and other disturbances effects, the input elements for precision output tracking can be achieved. As demonstrated in [48, 56], by using the ILC techniques, the tracking error can be reduced to the noise level. Thus, we consider that a practically achievable desired input element, $u_{i,k}^a(\cdot)$, can be obtained such that for every output element $y_{k,i}^*(\cdot)$ in the library \mathcal{L}_e , the practically achievable output element $y_{k,i}^a(\cdot)$ is different from the desired one by a known tracking limit ϵ_e , i.e.,

$$\|y_{k,i}^a(t) - y_{k,i}^*(t)\|_2 \leq \epsilon_e, \text{ for } \forall k = 1, \dots, q, \text{ and } i = 1, \dots, N_L. \tag{3.71}$$

Furthermore, when using the uniform B-spline elements in the decomposition, there are at

most $s + 1$ number of elements summed together at any given time instant. Thus, the following Lemma follows immediately.

Lemma 6 *Let conditions in Theorem (2) be satisfied, and the practically achievable desired input element be specified by (4.29). Also, let the pre- and post-actuation time $\mathbb{T}_{pa,1}$ and \mathbb{T}_{pst,N_k} be as in Theorem (2). Then at any given time instant t_c , the tracking error of using the synthesized input is bounded as*

$$\begin{aligned} \|E_y^a(t)\|_2 &\leq \|E_y(t)\|_2 + \left(\sum_{k=1}^q \|e_{y,k}^a(t)\|_2^2 \right)^{1/2}, \quad \text{with} \\ \|e_{y,k}^a(t)\|_2 &\leq \sum_{j=1}^{s+1} |p_{k,j}| \epsilon_e, \end{aligned} \quad (3.72)$$

where $p_{k,j}$ are the coefficients of the output elements used in the decomposition of the previewed desired output in the k^{th} output channel at time instant t .

3.2.6 ILC Approach to Construct the Library \mathcal{L}_e

The ILC approach is utilized in the proposed technique to obtain the desired input for each desired output element in the library \mathcal{L}_e . As the entire desired output element is known a priori, knowledge of the desired output can be fully exploited along with the system dynamics in the ILC framework [57], thereby, allowing the use of noncausality to overcome the nonminimum-phase constraints on tracking precision [58]. Moreover, the offline construction of the library allows the utilization of iteration to compensate for the adverse effect of repetitive disturbances, unmodelled dynamics, and parametric uncertainties. We note that various ILC techniques can be used for constructing the library [57, 58]—as an illustrative example, below the recently-developed multi-axis inversion-based control (MAIIC) technique [56] is presented,

$$\begin{aligned} \hat{U}_0(j\omega) &= 0 \\ \hat{U}_k(j\omega) &= \hat{U}_{k-1}(j\omega) + \rho(j\omega) G_{I,md}^{-1}(j\omega) (\hat{Y}_d(j\omega) - \hat{Y}_{k-1}(j\omega)) \end{aligned} \quad (3.73)$$

where $G_{I,md}$ is a diagonal matrix with diagonal elements being the model of the diagonal subsystems of system $G(j\omega)$,

$$G_{I,md}(j\omega) = \text{diag} [G_{11,md}(j\omega), G_{22,md}(j\omega), \dots, G_{nn,md}(j\omega)], \quad (3.74)$$

and

$$\rho(j\omega) = \text{diag} [\rho_1(j\omega), \rho_2(j\omega), \dots, \rho_n(j\omega)] \quad (3.75)$$

is the iteration coefficient matrix with the diagonal element $\rho_p(j\omega) \in \mathbb{R}^+$ for each $p \in \mathbb{Z}$. In (5.4), $\hat{U}_k(j\omega)$ and $\hat{Y}_k(j\omega)$ denote the input and output of the system in the k^{th} iteration, respectively,

$$\begin{aligned} \hat{U}_k(j\omega) &= [\hat{u}_{1,k}(j\omega), \hat{u}_{2,k}(j\omega), \dots, \hat{u}_{n,k}(j\omega)]^T, \\ \hat{Y}_k(j\omega) &= [\hat{y}_{1,k}(j\omega), \hat{y}_{2,k}(j\omega), \dots, \hat{y}_{n,k}(j\omega)]^T. \end{aligned} \quad (3.76)$$

It can be shown [56] that the above MAIIC technique can achieve precision output tracking in repetitive operations when the noise disturbance is small, and the noise effect can be quantified, frequency wise, by the ratio of the noise to the desired output amplitude. The efficacy of the above MAIIC approach has been demonstrated through experiments in nanopositioning control [56].

3.3 Nanomanipulation Simulation and Example

In this section, we illustrate the proposed technique by implementing it to an output tracking simulation for planner nanomanipulation application using two piezotube actuators. We start with describing precision positioning in nanomanipulation.

3.3.1 Output tracking with preview in nanomanipulation

Preview-based output tracking is needed in nanomanipulation, where a micro-machined cantilever probe driven by piezoelectric actuators is utilized to manipulate nanoscale subjects [15], both horizontally and perpendicularly, to, for example, build integrate circuit using nanotubes [40] or to conduct surgery operations on single live cell [41]. As nanomanipulation usually involves online-generated commands (e.g., through an imaging based interface), preview-based approach becomes a nature choice to output tracking, particularly at high-speed. Similar precision output tracking with preview also exists in areas such as nanofabrication [15] and robotic operation [16]. We focus, in the following, on x - y axes precision positioning in planer nanomanipulation—the use of the proposed approach to z -axis precision positioning is similar.

The dynamics of the piezoelectric actuator for x -axis (the y -axis dynamics is similar) positioning on an scanning probe microscope (SPM) system can be described by the transfer function below,

$$G(s) = \frac{x(s)}{u_x(s)} = K_x \frac{\prod_{q=1}^4 (s - z_q)}{\prod_{r=1}^6 (s - p_r)} \quad (3.77)$$

where the input and output are the voltage applied to the piezoelectric actuator (in Volt) and the displacement of the piezo actuator (in μm), respectively, and the Laplace transform variable s is in rad/ms (to reduce the numerical computation error), and

$$K_x = 29.28,$$

$$z_q = 0.9274 \pm 41.659i, -0.2484 \pm 30.434i,$$

$$p_r = -0.188 \pm 31.326i, -0.857 \pm 24.570i, -20.26, -15.20.$$

The above dynamics model is nonminimum-phase with a pair of complex zeros on the right-half-plan. Note to illustrate the proposed approach, we focused on the compensation for the linear dynamics only and neglected the hysteresis behavior of the piezo actuators — The hysteresis effect, as being range dependent [10], is negligible when the displacement is small relative to the full displacement range of the piezo actuator [10].

3.3.2 Implementation of the B-Spline-Decomposition-based Output Tracking

The proposed approach was implemented to a contour tracking typical in planar nanomanipulation, by following the three steps described in Sec. 4.2.1. The contour to track is shown in Fig. 3.4 (a), and the corresponding desired x - and y - axes trajectories are plotted in Fig. 3.4 (b), (c), respectively. To mimic the experimental condition in practical implementations, we considered that there existed disturbance and/or measurement noise augmented to the control input and the measured output, respectively. The added input/output noise was generated as a band-limited white-noise with cut-off frequency at 5 KHz. The amplitude of the noise at $\sim \pm 0.02 \mu\text{m}$ was similar to that observed in experiments of similar nanopositioning using SPM [56].

In the following simulation, we assumed that the preview time was 4 ms (i.e., at each sampling instant, the future desired trajectory was known for 4 ms). Such a preview time, quantified according to Theorem (4), was enough to ensure precision tracking of the desired

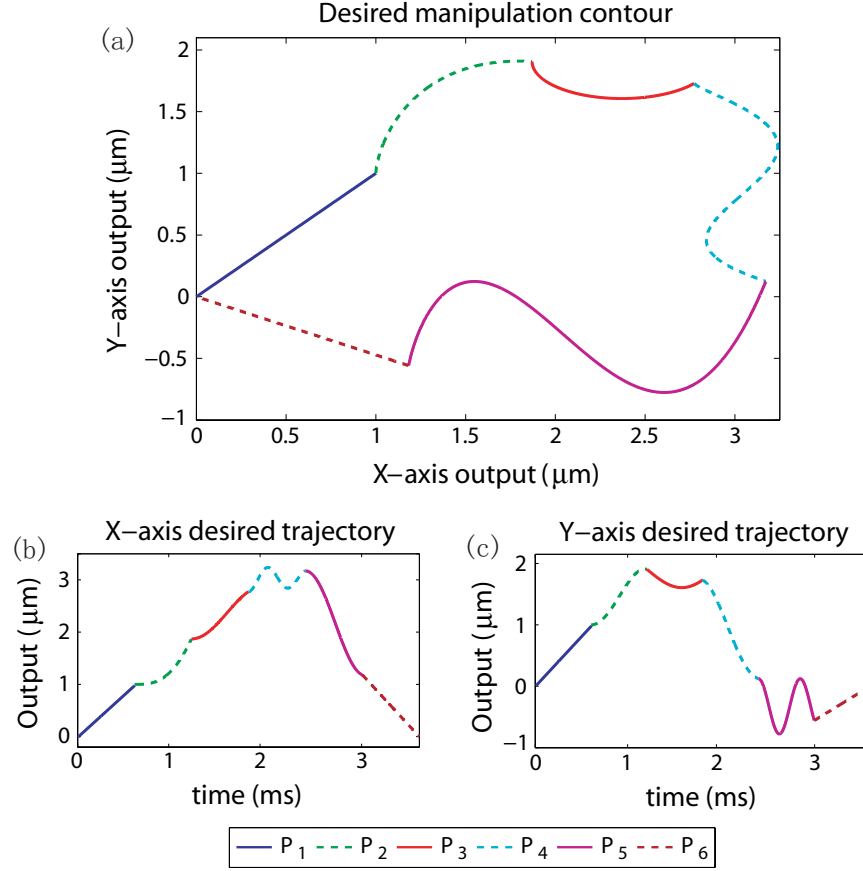


Figure 3.4: Desired manipulation contour and previewed X-Y desired trajectories in simulation.

trajectory (i.e., the tracking error was close to the size of noise added to the signals).

Library Construction The output elements $y_{k,i}^*(\cdot)$ for $k = 1, 2$ and $i = 1, \dots, N_L$ were constructed by using the 7th-degree uniform B-splines, resulting in a total of $N_L = 15$ output elements. With total knots number chosen at $m = 8$, the B-splines can be readily obtained recursively from (4.6), and the output elements for the truncated-at-the-beginning B-splines (total of 7) and those for the truncated-at-the-end (total of 7) were obtained via extension, smooth transition to zero, and filtering (See Subsec. 3.2.4). The corresponding input elements $u_{k,i}^*(\cdot)$ for $k = 1, 2$ and $i = 1, \dots, 15$ were obtained by using the MAIIC technique. The relative tracking error of each output element in 2-norm, $E_2(\%)$, was very close to the noise level at $\sim 0.5\%$ (As demonstrated in [56], precision output tracking with tracking error close

to noise level can be achieved by using the MAIIC technique in experiments), where

$$E_2(\%) = \frac{\|y_{k,i}^*(\cdot) - y_{k,i}^a(\cdot)\|_2}{\|y_{k,i}^*(\cdot)\|_2}.$$

Desired Trajectory Decomposition With given previewed desired trajectory (i.e., with given preview time), the required pre- and post-actuation times can be quantified by Theorem (4) and Lemma (7), which, in turn, can be used to determine the decomposition instant by (4.20). As an example, the decomposition instants along with the corresponding decomposition of the x - and y -axes desired trajectories at each instant for the same pre-actuation time of $T_{pa,j} = 3$ ms for $\forall j$ are shown in Fig. 3.5. With knots number $m = 8$, a total of 15 output elements were used in the approximation at each decomposition instant. The approximation error measured in 2-norm was below 0.001 %, over 500 times smaller than the noise size (The same approximation precision was maintained in the following simulation).

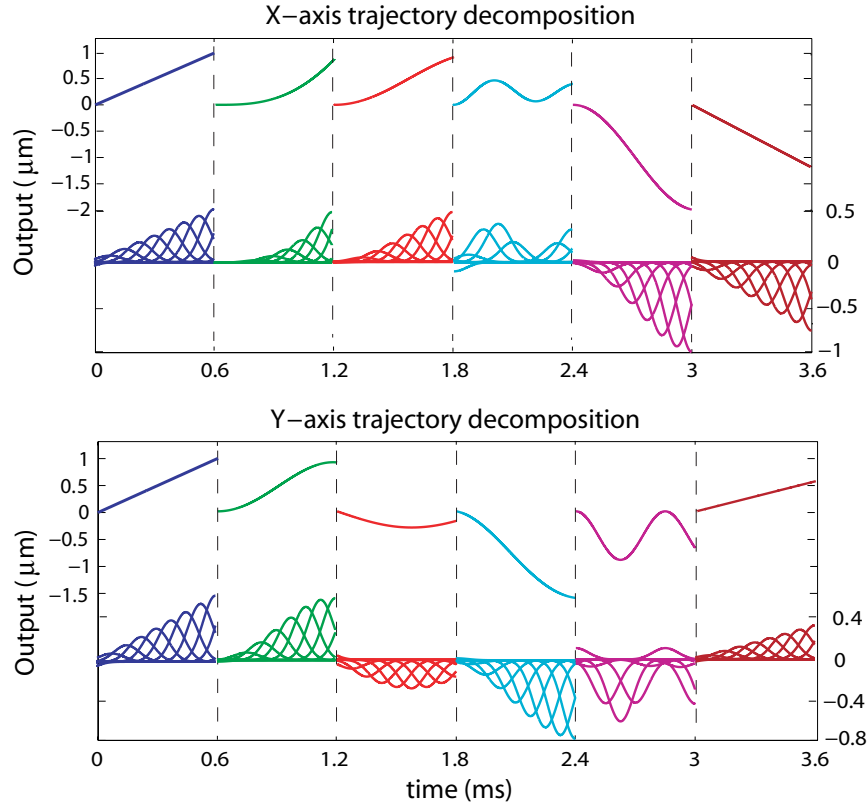


Figure 3.5: The decomposition of the previewed desired trajectory by using the 7th-degree uniform B-spline elements, where the pre-actuation time was chosen the same as 3 ms for the total preview time of 4 ms (for the ease of presentation).

Online Input Synthesis At each time decomposition instant $t_{dec,j}$, the control input for tracking the decomposed desired trajectory was synthesized by adding together the input elements corresponding to the output elements employed in the approximation at that instant (see Eq. (4.21)), with truncation at the beginning and the end for the chosen pre-actuation time $\mathbb{T}_{pa,j}$ and post-actuation time $\mathbb{T}_{pst,j}$, respectively. Then the control input was updated according to (4.23).

3.3.3 Simulation results and discussion

To demonstrate the effects of pre-actuation and post-actuation time on the output tracking performance, the y -axis output tracking with two different pre-actuation times $\mathbb{T}_{pa,j}$ and two different post-actuation times $\mathbb{T}_{pst,j}$, $\mathbb{T}_{pa,j} = 0.05, 3$ ms, and $\mathbb{T}_{pst,j} = 0.05, 1$ ms, respectively, were investigated in the simulations¹. Specifically, the y -axis output tracking results are compared in Fig. 3.6 for the pre-actuation time of $\mathbb{T}_{pa,j} = 3$ ms, and 0.05 ms in y -axis, where the post-actuation time was kept the same at $\mathbb{T}_{pst,j} = 1$ ms for all $j = 1, 2, \dots, 6$. The tracking results obtained with two different post-actuation times $\mathbb{T}_{pst,j} = 1$ ms and 0.05 ms are also compared in Fig. 3.7, where the pre-actuation time was kept the same at $\mathbb{T}_{pa,j} = 3$ ms. We also examined the exponential decaying of the tracking error with the increase of the pre- and post actuation time (See Theorem (4)), as shown for the y -axis in Fig. 3.8.

Also, the manipulation contour tracking results are compared in Fig. 3.9 for the pre-actuation time of $\mathbb{T}_{pa,j} = 3$ ms and 0.05 ms and post-actuation time of $\mathbb{T}_{pst,j} = 1$ ms and 0.05 ms, respectively, where a long enough post-actuation time and pre-actuation time were applied in both cases. Moreover, the manipulation contour tracking results are compared in Fig. 3.10 for the pre- and post-actuation time $T_{pa} = 0.05$ ms, $T_{pst} = 0.05$ ms and the pre- and post-actuation time $T_{pa} = 3$ ms, $T_{pst} = 1$ ms.

The simulation results show that by using the proposed trajectory-decomposition-based output tracking technique, precision output tracking can be maintained throughout the entire

¹We realize that pre- and post-actuation time can be chosen differently at each decomposition instant to account for the change of the desired output amplitude. To simplify the presentation the same pre- and post-actuation times across all decomposition instant were chosen here

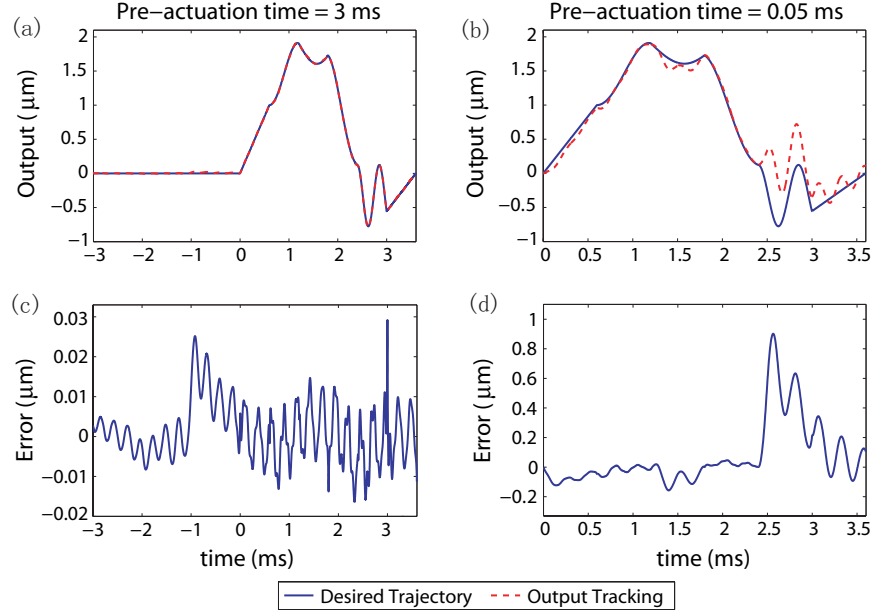


Figure 3.6: Comparison of (upper row) the y-axis output tracking and (lower row) the tracking error obtained by using the proposed technique with pre-actuation time of (left column) $T_{pa} = 3$ ms, (right column) $T_{pa} = 0.05$ ms. The post-actuation time was the same at $T_{pst} = 1$ ms for $j = 1$ to $j = 6$.

output tracking. The output tracking performance can be significantly improved as the pre-actuation time was increased. For example, by using the proposed technique, the relative RMS tracking error $E_2(\%)$ was only 0.54% for y axes when the pre-actuation time was at 3 ms, (see Fig. 3.6 (a), (c)). Note that such a tracking error size was comparable to the size of the noise and disturbance existing in the control system. On the contrary, when the pre-actuation time became much shorter at $T_{pa} = 0.05$ ms, such a good tracking cannot be maintained — the relative RMS tracking error $E_2(\%)$ was about 22.67% for y axis (see Fig. 3.6 (b), (d)). Therefore, precision output tracking can be achieved with a long-enough pre-actuation time.

The simulation results also demonstrated that when the pre-actuation time was fixed, the tracking error increased as the post-actuation time reduced. When the pre-actuation time was long enough, the tracking error was small when the post-actuation time was long. The simulation results above showed that a pre-actuation of $T_{pa} = 3$ ms was long enough to achieve precision output tracking. Thus, precision output tracking with noise level tracking error ($E_2(\%) = 0.62\%$) was achieved when the post-actuation time was large at $T_{pst} = 1$ ms (see Fig. 3.7 (a), (c)). However, the tracking error increased significantly when the post-actuation time was

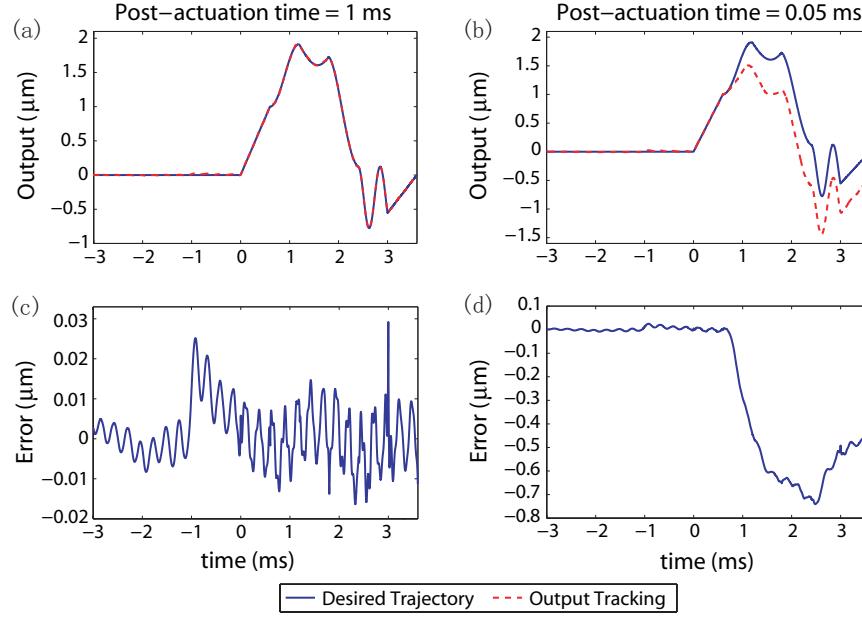


Figure 3.7: Comparison of (upper row) the y-axis output tracking and (lower row) the tracking error obtained by using the proposed technique with post-actuation time of (left column) $T_{pst} = 1$ ms, (right column) $T_{pst} = 0.05$ ms. The pre-actuation time was the same at $T_{pa} = 3$ ms for $j = 1$ to $j = 6$.

reduced to $T_{pst} = 0.05$ ms (see Fig. 3.7 (b), (d)). Therefore, the simulation results demonstrated that precision output tracking can be achieved (down to the noise level) by choosing a sufficiently large pre- and post-actuation time in the proposed approach.

Simulation results also illustrated the effects of the desired output size along with the increase of number of decomposition instants on the tracking performance. As shown in both Fig. 3.6 and Fig. 3.7, the finite pre- or post-actuation time caused tracking error became much larger in the later half of the tracking than that in the earlier half². Such an increase of the tracking error reflects the combined effect of the desired output size and the number of decomposition instants — both as been described in Theorem (4). Particularly, the accumulation of decomposition instants led to a larger constant $\hat{\mathbb{K}}_1$ and a larger value of $\Lambda_2(\cdot, \cdot, \cdot)$, resulting in a larger finite pre- and post-actuation time caused tracking error (See (4.24)). However, Theorem (4) (see Eq. (4.24)) also shows that the increase of pre- and post-actuation time eventually exponentially dominates these two effects, as evidently shown in Fig. 3.8. Therefore, the

²The decrease of the tracking error near the end of the tracking was due to the vanishing of the nonminimum-phase zero effect as the entire future trajectory became completely available

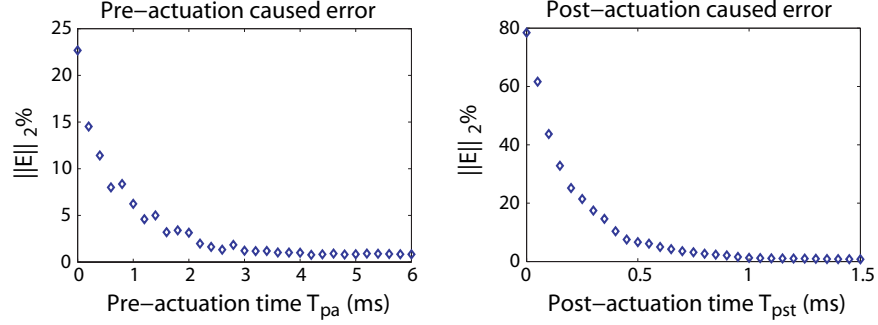


Figure 3.8: The 2-norm of the tracking error vs. pre-actuation time (left column) and post-actuation time (right column).

simulation results demonstrated the efficacy of the proposed approach in preview-based output tracking applications.

3.4 Conclusions

In this chapter, a B-spline-decomposition-based approach to output tracking with preview was proposed. A library consisting of elements of input-output pairs was constructed offline a priori to decompose the previewed desired output trajectory and then synthesis the corresponding control input. Uniform B-splines were used to generate the output elements, where the truncated B-splines with none-zero starting or end value were extended and smoothly transited to zero via filtering in generating the output elements. The corresponding input elements were obtained offline by, for example, iterative learning control techniques. The effect of finite pre- and post-actuation time of the synthesized control input on the tracking performance were quantified by using the stable-inversion theory. The proposed method was illustrated by a planar nanomanipulation simulation study with two nonminimum-phase piezo actuator models.

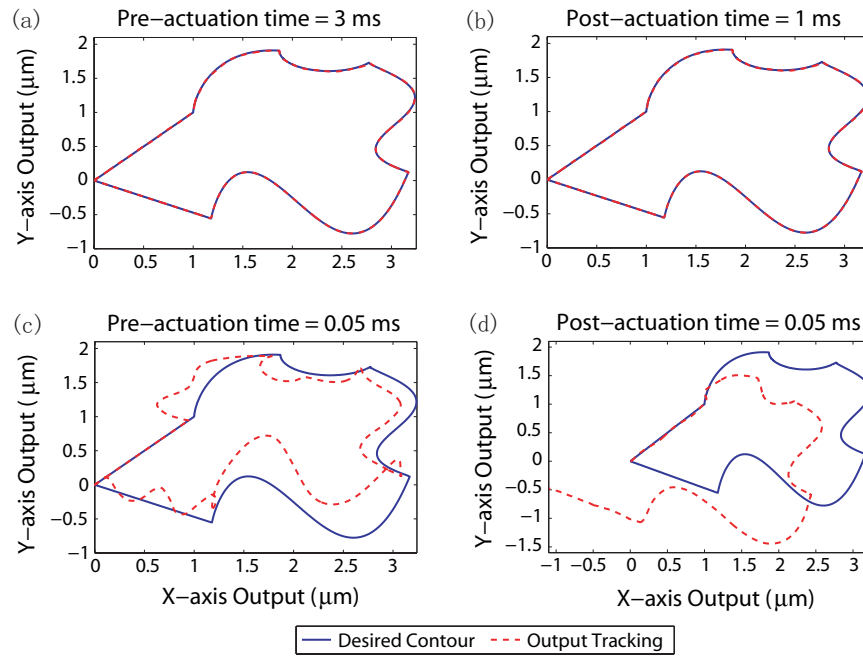


Figure 3.9: Comparison of the manipulation contour tracking using the proposed technique with (left column) pre-actuation time of (upper row) $T_{pa} = 3$ ms and (lower row) $T_{pa} = 0.05$ ms, and (right column) post-actuation time of (upper row) $T_{pst} = 1$ ms and (lower row) $T_{pst} = 0.05$ ms.

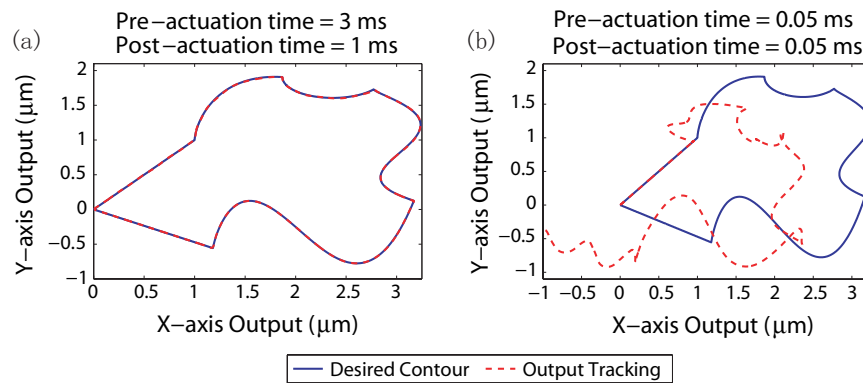


Figure 3.10: Comparison of the manipulation contour tracking using the proposed technique with (left column) pre- and post-actuation time $T_{pa} = 3$ ms and $T_{pst} = 1$ ms, and (right column) pre- and post-actuation time $T_{pa} = 0.05$ ms and $T_{pst} = 0.05$ ms.

Chapter 4

B-spline-Decomposition-Based Approach to Multi-Axis Trajectory Tracking: Nanomanipulation Example

Abstract

In this chapter, a B-spline-decomposition (BSD)-based approach to output tracking with preview is explored to achieve high-speed, large-range nanomanipulation in experiments. When a finite (in time) preview of the future desired trajectory is available, precision output tracking of nonminimum-phase (NMP) systems can be achieved by using the preview-based stable-inversion technique. The performance of the preview-based inversion approach, however, can be sensitive to uncertainties of system dynamics. Moreover, the computation involved in the implementation can be demanding. The BSD approach has been developed recently to address these challenges. In the BSD approach, a library of desired output elements and their corresponding input elements is constructed a priori, then the previewed future desired trajectory is decomposed into a summation of finite number of output elements, and the control input is synthesized by using the corresponding input elements with chosen pre- and post-actuation times. The BSD technique utilizes the uniform B-splines to construct the output elements, the ILC techniques to obtain the input elements, and the stable-inversion theory to quantify the pre- and post-actuation times. In this work, we demonstrate and evaluate the BSD technique for precision tracking with preview in experiments, by implementing it to a nanomanipulation application using a scanning probe microscope. Particularly, a feedback controller consisting of a proportional-integral (PI) followed by a notch filter is formed first to account for the hysteresis and creep effects of the piezo actuator, then the BSD technique is applied to the closed-loop system to achieve precision tracking at high-speed. The experiments showed that the tracking speed can be substantially improved by using the BSD technique over using feedback control alone.

4.1 Introduction

This chapter is focused on high-speed nan positioning control in tracking online generated trajectory via a novel B-spline-decomposition-based (BSD) technique [59]. Nan positioning is needed in a wide range of applications, from scanning probe microscope (SPM) [60], precision optics [61], silicon wafer alignment [62], to micro/nano robotics [15]. For example, nan positioning of the cantilever probe relative to the sample surface is central to—at nanoscale—image, measure, manipulate, and pattern the sample using SPM [60]. High-speed nan positioning is particularly important as precision nan positioning at high-speed not only directly translates and results in improved efficiency and throughput, but more importantly, enables studies and operations not possible otherwise. For example, high-speed SPM imaging allows, for the first time, direct observation of locomotion of living cells [63]. High-speed nan positioning via hardware innovation (e.g., piezoelectric actuators with higher-bandwidth), however, tends to be accompanied with increased cost and/or reduced operation range [62]. Therefore, advanced control techniques are needed to continuously improve high-speed nan positioning performance.

Various feedback techniques have been proposed for nan positioning control. As smart actuators such as piezoelectric actuators are widely used in nan positioning applications, nan positioning control is often complicated by the hysteresis behavior and drift (creep) effects of piezo actuators [9]. These adverse effects are coupled with the vibrational dynamics of the nan positioning system along with other disturbances of random behavior (e.g., measurement noise) [64, 65]. Feedback control approaches [65]–[68] such as robust control and sliding mode control have been developed to compensate for these effects of nonlinear and random nature. The tracking precision of these feedback approaches at high-speed, however, can be limited as the closed-loop bandwidth, thereby the tracking precision at high-speed, needs to be traded-off with the robustness requirement—governed by the *Bode's plot* [1]. Such a trade-off-caused bandwidth limit is more pronounced when the sensor noise becomes significant as sensor noise can be “amplified” by the feedback loop otherwise and result in large output oscillations [69]. Moreover, for non-minimum phase systems, the tracking precision of feedback control system is dictated by the non-minimum phase zeros of the system, i.e., exact tracking cannot be

achieved by feedback control alone [2]. Therefore, challenges exist in feedback control for high-speed nanopositioning control.

These feedback-related challenges to high-speed nanopositioning control can be largely alleviated by using feedforward control techniques, as demonstrated by the inversion-based feedforward control techniques developed recently [6, 9, 60]. By inverting the model of the vibrational dynamics and/or hysteresis [9], precision tracking of a given desired trajectory can be achieved by applying the obtained inverse input as a feedforward. The inversion-based feedforward approach can be quite effective in high-speed precision tracking as the open-loop bandwidth tends to be larger than the closed-loop one, and the issue of noise amplification can be largely avoided in feedforward control. Particularly, the inversion-based techniques overcome the constraints of non-minimum phase zeros imposed on the tracking performance, and achieve exact tracking for non-minimum phase systems. The efficacy of the inversion-based approach to high-speed nanopositioning has been illustrated experimentally in SPM imaging applications [6, 42]. The performance of the inversion-based control, however, can be sensitive to modeling error [17, 42], while it is not practical in practices to correct/update the model each time when the effect of the system dynamics variation becomes significant. Moreover, for nonminimum-phase systems, the computation load can be demanding when tracking online-specified desired trajectory [20], as convolution operation is required during the sampling period when obtaining/updating the inverse input online. Thus, there exists a need to address these constraints of feedforward approach to high-speed nanopositioning control.

These modeling and online-computation related issues in the inversion-based approach can be largely avoided through the iterative learning control framework of nanopositioning [64, 70, 71]. Particularly, the modeling errors and slow variation of the system dynamics caused by, for example, parts replacement (e.g., change of cantilever probe in SPM (so that the system dynamics itself remains largely unchanged during the current operation)) can be easily accounted for via few iterations with no trade-off to tracking precision [64, 70]. The iteration framework also provides a nature venue to employ noncausality to achieve exact tracking for non-minimum phase systems, as well as to compensate for both the hysteresis and dynamics effects [64] during high-speed, large-range nanopositioning applications. The ILC approach, however, is limited to *repetitive* operations, and cannot be directly implemented to applications where the

desired trajectory is specified online, such as nanomanipulation or nanofabrication [15]. Thus, high-speed precision tracking in *nonrepetitive* nanopositioning control still remains as a challenge.

In this chapter, we propose to address the limits described above for high-speed nanopositioning by using the recently-developed BSD technique [59] for high-speed precision tracking of online-specified trajectories, and demonstrate this technique through experiment of trajectory tracking in nanomanipulation application. The BSD technique avoids the demanding online computation when tracking an online-generated desired trajectory with preview (i.e., the future desired trajectory is known for a finite amount of preview time), by decomposing the previewed desired trajectory into a finite number of output elements based on B-splines, and synthesizing the control input by using the corresponding input elements via the superposition principle. The BSD technique retains the advantages of the ILC approach described above by using the ILC technique to construct a library of pairs of input-output elements *a priori*, while extending the ILC framework to non-repetitive tracking via online decomposition. The stable-inversion theory [3] is utilized to quantify the pre- and post-actuation times [23] required in the input synthesis. In this work, the BSD technique is implemented to track a planar trajectory in 2D nanomanipulation. First, a feedback loop consisting of a proportional-integral (PI) controller followed by a notch filter is employed to account for mainly the drift and hysteresis effects. Then, by applying the BSD technique to the closed-loop system, the experimental results show that the precision of output tracking with preview can be substantially improved over feedback control alone, particularly at high-speed. The effect of finite post-actuation time on tracking precision has also been studied and demonstrated in the experiment. Therefore, this chapter demonstrates the efficacy of the BSD technique for high-speed precision tracking of preview in nanopositioning control applications in practices.

The rest of the chapter is organized as follows. The BSD technique is described in Section 4.2 from practical implementation viewpoint. Then, in Section 4.3, the BSD technique is applied to the output tracking experiment in nanomanipulation, along with the experimental results and discussions. Our conclusions are given in Section 4.4.

4.2 B-spline-Decomposition-Based Approach to Output Tracking with Preview

The BSD approach proposed in [59] aims to overcome two main constraints of the stable-inversion-based technique to output tracking with preview [6]—sensitive to modeling error, and demanding online computation—while retaining the advantage of the inversion approach in achieving precision tracking for NMP systems. Particularly, the BSD approach is developed for linear time invariant (LTI) systems given by

$$\begin{aligned}\dot{x}(t) &= Ax(t) + Bu(t) \\ y(t) &= Cx(t)\end{aligned}\tag{4.1}$$

where $x(t) \in \mathbb{R}^n$ is the state, and $u(t) \in \mathbb{R}^q$, $y(t) \in \mathbb{R}^q$ are the input and output, respectively.

We consider that system (4.1) is controllable and observable, with a well-defined relative degree ($r = [r_1, r_2, \dots, r_q]$), and no zeros on the imaginary axis. Moreover, the desired trajectory to track is sufficiently smooth (i.e., the j^{th} desired output, for each $j = 1, 2, \dots, p$, is differentiable at least to the r_j^{th} order), and can be previewed for a finite time T_p . These conditions are reasonable and can be satisfied in a wide range of tracking applications (including the nanomanipulation example studied in this chapter).

4.2.1 Decomposition-Synthesis-Based Output Tracking

Next we present the BSD technique from implementation viewpoint—the derivation and analysis of the technique are omitted (readers are referred to [59] for details). The BSD technique mainly comprises the following three steps.

Step 1) Construct a Library of desired input-output elements \mathcal{L}_e The library is to provide the output elements for decomposing the previewed desired trajectory, and the corresponding input elements for synthesizing the input. Specifically, the library \mathcal{L}_e of pairs of B-spline-based input-output elements is given by

$$\mathcal{L}_e = \{[y_{k,i}^*(\cdot), u_{k,i}^*(\cdot)] \mid k = 1, 2, \dots, q; i = 1, 2, \dots, N_e\}\tag{4.2}$$

where N_e is the total number of different base output elements, and for ease of input-synthesis, the desired output elements $y_{k,i}^*(\cdot) \in \mathbb{R}^{q \times 1}$ for given k and $i = 1, 2, \dots, N_e$ have only the

k^{th} output channel nonzero, i.e., only one base output element, $y_{e,i}^*(\cdot) \in \mathfrak{R}$, appears in the k^{th} output channel,

$$y_{k,i}^*(\cdot) = [0 \cdots y_{e,i}^*(\cdot) \cdots 0]^T, \text{ with } i = 1, 2, \dots, N_e, \quad (4.3)$$

and $u_{k,i}^*(\cdot) \in \mathfrak{R}^{q \times 1}$ is the corresponding desired input element,

$$u_{k,i}^*(\cdot) = [u_{k,i,1}(\cdot) \cdots u_{k,i,q}(\cdot)]^T, \text{ with } i = 1, 2, \dots, N_e. \quad (4.4)$$

Thus, the total number of input-output elements N_L is given by $N_L = q \times N_e$. The base output elements, $y_{e,i}^*(\cdot)$ s, are generated by using the s^{th} -order uniform B-splines, $B_{i,s}(\cdot)$ for $i = 1, 2, \dots, N_e$, where the uniform B-splines $B_{i,s}(\cdot)$ can be constructed recursively by setting

$$B_{i,0}(t) = \begin{cases} 1, & \text{for } t_i \leq t < t_{i+1}, \\ 0, & \text{otherwise,} \end{cases} \quad (4.5)$$

and then recursively

$$B_{i,s}(t) = \frac{t - t_i}{t_{i+s} - t_i} B_{i,s-1}(t) + \frac{t_{i+s+1} - t}{t_{i+s+1} - t_{i+1}} B_{i+1,s-1}(t), \quad (4.6)$$

$$i = -s + 1, -s + 2, \dots, m - 1,$$

where, for $t \in [0, \mathbf{T}_d]$, $m > s + 2$ is the total number of knots with t_i s for $i = -s + 1, -s + 2, \dots, m - 1$, chosen as below in the decomposition

$$0 \leq t_{-s+1} \leq t_{-s+2} \leq \cdots \leq t_{m-1} \leq \mathbf{T}_d.$$

Uniform B-splines are obtained when the knots selected are evenly spaced within the time interval, with shift time given by the spacing between two successive knots as,

$$t_{sep,k,i} = t_{i+1} - t_i = \frac{\mathbf{T}_d}{m - 1} = \Delta t_{sep,i} \quad (4.7)$$

Thus, uniform B-splines are nothing but time-shift copies of each other, with the shifting time equaling to $t_{sep,k,i}$. The use of uniform B-splines (instead of non-uniform ones) results in a small size of library. For example, when using the uniform cubic (3^{rd} -order) splines, only

seven different B-splines are needed to construct the output elements (i.e., N_e in Eq. (4.3) = 7), including one base function (shown in Fig. 4.1 (a)) and six truncated B-splines needed to decompose the beginning (or the end) portion of the previewed desired trajectory, as shown in Fig. 4.1 (b) to (g). These six output elements are obtained by smoothly extending and transiting the six truncated B-splines to zero at the end (or from zero at the beginning). Specifically, the output elements in the library generated by the truncated B-splines with non-zero starting values are obtained via extension and smooth transition as

$$y_{e,i}^*(t + 3\mathbb{T}_{pa}^*) = \begin{cases} 0 & t < -3\mathbb{T}_{pa}^* \\ \mathcal{T}_{e,i}(t) & t \in [-3\mathbb{T}_{pa}^*, -2\mathbb{T}_{pa}^*], \\ y_{e,i}^*(0) & t \in (-2\mathbb{T}_{pa}^*, 0), \\ y_{e,i}^*(t) & t \in [0, t_i], \end{cases} \quad (4.8)$$

Similarly, the output elements generated from the truncated B-splines with non-zero ending values are obtained via extension and smooth transition for $t > t_i$ as

$$y_{e,i}^*(t) = \begin{cases} y_{e,i}^*(t) & t \in [0, t_i], \\ y_{e,i}^*(t_i) & t \in (t_i, t_i + 2\mathbb{T}_{pst}^*), \\ \mathcal{T}_{e,i}(t) & t \in [t_i + 2\mathbb{T}_{pst}^*, t_i + 3\mathbb{T}_{pst}^*], \\ 0 & t > t_i + 3\mathbb{T}_{pst}^* \end{cases} \quad (4.9)$$

where \mathbb{T}_{pa}^* and \mathbb{T}_{pst}^* are the maximum pre- and post-actuation times that are large enough to guarantee the needed tracking precision for all tracking in the given application, $\mathcal{T}_{e,i}(\cdot)$ denotes a smooth function to transit the output element $y_{e,i}^*(t)$ from 0 to the truncated value at $y_{e,i}^*(0)$. Quantification of the pre- and post-actuation times is presented in Sec. 4.2.2 later.

Note that the B-spline-based output elements generated above are sufficiently smooth with a compact support starting at time $t = 0$, i.e., for $i = 1, 2, \dots, N_e$,

$$y_{e,i}^*(t) = 0 \text{ for } t \notin [0, t_i], \text{ with } t_i < \infty. \quad (4.10)$$

For each output element $y_{e,i}^*(\cdot)$, the corresponding input element is obtained in advance by using the ILC techniques. As the entire output element is known, ILC approach is advantageous in utilizing noncausality to achieve exact output tracking for NMP systems [48, 47] (i.e., precision tracking in practices), and the iteration mechanism to account for modeling errors

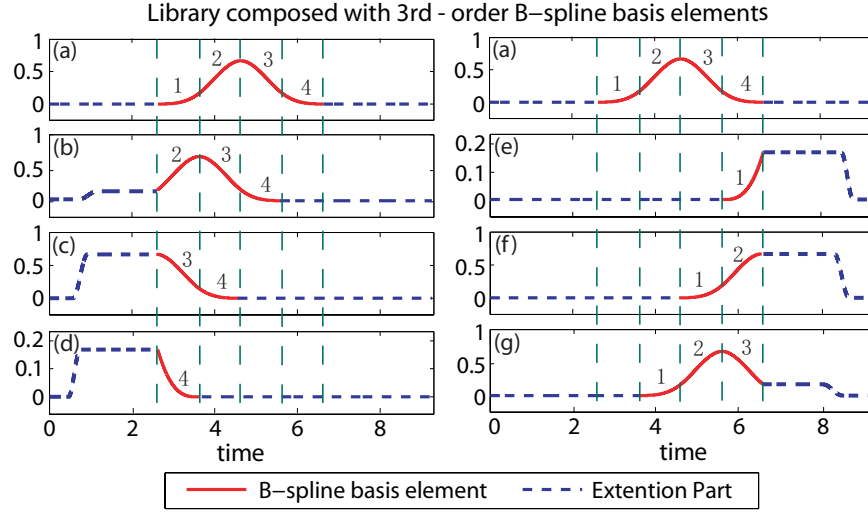


Figure 4.1: The seven ((a) to (g)) output elements generated by using the cubic uniform B-splines.

caused by the change of system dynamics, particularly for modeling errors caused by factors such as the changes of operation condition or parts. As the input obtained previously achieved precision tracking priori the system dynamics change, only few iterations are needed provided that the dynamics change is small (as in many applications). Such a compensation for modeling error with no tracking precision trade-off is more efficient and easier to implement in practices than updating the system model and using the updated model to redesign the controller—as needed in many feedback and feedforward control approaches. Precision tracking achieved by using the ILC has been well demonstrated in the literature [?], including nano-positioning control [11, 38, 56]. As an example, the multi-axis inversion based control (MAIIC) technique used in this work is presented in Sec. 4.3.

Step 2) Decompose the Previewed Desired Trajectory Online At any given j^{th} decomposition instant (see Fig. 4.2) $t_{dec,j}$, the desired trajectory $y_d(t)$ for $t \in [t_{dec,j} + \mathbb{T}_{pa,j}, t_{dec,j} + T_p]$ is decomposed as:

$$y_{d,k}(t) \approx \sum_{i=1}^{N_{d,k}} p_{k,i} B_{s,i}(t) \triangleq p_{apx,k}(t), \quad (4.11)$$

where $\mathbb{T}_{pa,j}$ is the pre-actuation time at the j^{th} decomposition instant, and the coefficients of

the decomposition, $p_{k,i}s$, are obtained by solving the following quadratic minimization problem [55],

$$\min_{P_k \in \mathbb{R}^{N_{d,k}}} J(\gamma), \text{ with} \quad (4.12)$$

$$J(\gamma) \triangleq \int_I \lambda (p_{apx,k}^{(2)}(t))^2 dt + \sum_{j=1}^{N_{d,k}} w_j (p_{apx,k}(\gamma_j) - y_{d,k}(\gamma_j))^2,$$

$$P_k = [p_{k,-s+1} \ p_{k,-s+2} \ \cdots \ p_{k,m-1}]^T, \quad (4.13)$$

$$\gamma = \{\gamma_1 \ \gamma_2 \ \cdots \ \gamma_{N_{d,k}}\}^T,$$

and $\lambda > 0$, $w_j \in [0, 1]$ for $\forall j$ are the weights. The solution is readily obtained as

$$P_k^* = (\lambda Q + M^T W M)^{-1} M^T W \zeta_{y,k} \quad (4.14)$$

where

$$\zeta_{y,k} = [y_{d,k}(\gamma_1) \ y_{d,k}(\gamma_2) \ \cdots \ y_{d,k}(\gamma_{N_{d,k}})]^T, \quad (4.15)$$

$$W = \text{diag}([w_1 \ w_2 \ \cdots \ w_{N_{d,k}}]), \quad (4.16)$$

$$Q = [q_{i,j}] \in \mathbb{R}^{N_{d,k} \times N_{d,k}}, \ i, j = 1, 2, \dots, N_{d,k}, \quad (4.17)$$

with

$$q_{i,j} = \int_{I_{tc}} B_{i,s}^{(2)}(t) B_{j,s}^{(2)}(t) dt. \quad (4.18)$$

and the matrix $M \in \mathbb{R}^{N_{d,k} \times N_{d,k}}$ is given by

$$M = \begin{bmatrix} B_{s,1}(\gamma_1) & B_{s,2}(\gamma_1) & \cdots & B_{s,N_{d,k}}(\gamma_1) \\ B_{s,1}(\gamma_2) & B_{s,2}(\gamma_2) & \cdots & B_{s,N_{d,k}}(\gamma_2) \\ \vdots & \vdots & \vdots & \vdots \\ B_{s,1}(\gamma_{N_{d,k}}) & B_{s,2}(\gamma_{N_{d,k}}) & \cdots & B_{s,N_{d,k}}(\gamma_{N_{d,k}}) \end{bmatrix} \quad (4.19)$$

Note that in solution (4.14), all the matrices (vectors) except the sampled values of the desired output in (4.15) are known *a priori*. Thus, the previewed output trajectory can be effectively decomposed online.

In the above decomposition, the j^{th} **decomposition instant**, $t_{dec,j}$, is the time instant at which the previewed desired trajectory $y_d(t)$ for $t \in [t_{dec,j} + \mathbb{T}_{pa,j}, t_{dec,j} + T_p)$ is decomposed, and is given by (see Fig. 4.2),

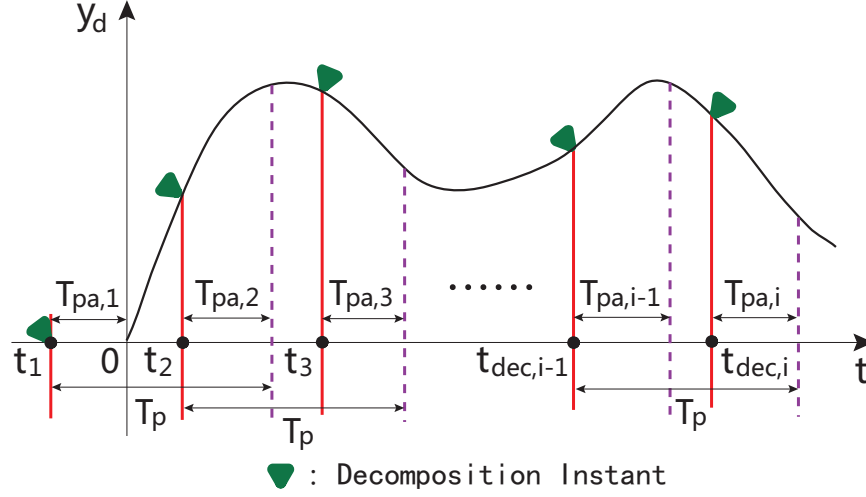


Figure 4.2: The output decomposition in the BSD technique.

$$t_{dec,j} = t_{dec,j-1} + T_p - \mathbb{T}_{pa,j}, \quad \text{for } j > 1, \quad (4.20)$$

and $t_{dec,1} = 0$ initially.

Step 3) Synthesize the Input Online Based on the decomposition in Eq. (4.11), the desired input to track the added part of the previewed desired output $u_{d,k}(t)$, $y_{d,k}(t)$ for $t \in [t_{dec,j} + \mathbb{T}_{pa,j}, t_{dec,j} + T_p]$ and any give output channel k ($k = 1, 2, \dots, q$), is given by

$$u_{d,j}(t) = \sum_{k=1}^q \left(\sum_{i=1}^{N_{d,k}} p_{k,i} u_{k,i}^*(t - t_{dec,j} - t_{sep,k,i}) \right) \quad (4.21)$$

where $u_{k,i}^*(t) \in \mathbb{R}^{p \times 1}$ is given by (4.4). Note that the tracking of the original desired trajectory $y_d(\cdot)$ is guaranteed by the superposition property of LTI systems (see (4.2)—(4.4)). Then for a given required tracking precision ϵ , the corresponding pre-actuation time $\mathbb{T}_{pa,j}$ and post-actuation time $\mathbb{T}_{pst,j}$ can be determined (discussed later in Sec. 4.2.2), and the truncated control input to track the decomposed part of the previewed desired output trajectory is obtained as

$$u_{trt,j}(t) = \mathcal{W}_{t_{j,1}, t_{j,2}}(t) u_{d,j}(t), \quad \text{for tracking} \quad (4.22)$$

$$y_{d,k} \in [t_{dec,j} + \mathbb{T}_{pa,j}, t_{dec,j} + T_p],$$

where $\mathcal{W}_{t_{j,1}, t_{j,2}}(\cdot)$ is the window function (i.e., $\mathcal{W}_{t_1, t_2}(t) = 1$ for $t \in [t_1, t_2]$, and $\mathcal{W}_{t_1, t_2}(t) = 0$ otherwise) with

$$t_{j,1} = t_{dec,j}, \quad t_{j,2} = t_{dec,j} + t_{j,max} + \mathbb{T}_{pst,j},$$

and $t_{j,max}$ is the upper bound of the supports of all the output elements selected for the j^{th} decomposition, $t_{j,max} = \sup_k t_{k,j}$.

Finally, the control input is updated as

$$u_{pre,j}(t) = \begin{cases} u_{pre,j}(t) + u_{trt,j}(t), & t = t_{dec,j} \\ u_{pre,j}(t), & t \in (t_{dec,j}, t_{dec,j+1}) \end{cases} \quad (4.23)$$

As schematically depicted in Fig. 4.2 (and experimentally demonstrated later in Sec. 4.3), the decomposition-synthesis operation is only needed at the decomposition instants as specified by (4.20)—not at every sampling instant.

4.2.2 Quantification of the Pre- and Post-Actuation Times

We present quantification of the pre- and post-actuation times based on the stable-inversion theory below [59]. As the input to achieve exact tracking for a given desired trajectory is *unique* for systems considered in this chapter, the quantification is general—regardless the techniques employed in obtaining the input elements of the library.

In the next Theorem, the tracking error caused by the finite pre- and post-actuation times is quantified for any given time instant during the output tracking course, i.e., we consider that there are m number of decomposition instants priori to the current time instant t_c , and the accumulated tracking error caused by the finite pre- and post-actuation times at all the m number of decomposition instants is quantified.

Theorem 4 *At any given time instant t_c , assume that there are m number of decomposition instants before t_c , $t_{dec,j}$ with $j = 1, \dots, m$, and at each $t_{dec,j}$ there are N_j number of s^{th} -degree uniform B-splines based output elements used in the decomposition. Then the finite pre- and post-actuation caused output tracking error at any time instant $t \geq t_c$ can be bounded as*

$$\|E_y(t)\|_2 = \left(\sum_{k=1}^q (\|E_{y,k}(t)\|_2)^2 \right)^{1/2}, \quad (4.24)$$

where for $k = 1, \dots, q$, and $t > m(T_p - \mathbb{T}_{pa,m}^*)$,

$$\begin{aligned} \|E_{y,k}(t)\|_2 &\leq \hat{\mathbf{Y}}_{m,k}^\infty \left\{ \hat{\mathbb{K}}_1 e^{-(\beta \mathbb{T}_{pa,m}^* + \lambda t)} \right. \\ &\quad \left. + \left[\Lambda_1(m\mathbb{K}_2, \hat{\mathbb{K}}_3, t) e^{-\beta \mathbb{T}_{pst,m}^*} + \Lambda_1(m\mathbb{K}_4, \hat{\mathbb{K}}_5, t) e^{-\alpha \mathbb{T}_{pst,m}^*} \right] \right\}, \end{aligned} \quad (4.25)$$

and for $j = 1, 2, \dots, m$,

$$\begin{aligned} \hat{\mathbf{Y}}_{m,k}^\infty &= \max_j \hat{\mathbf{Y}}_{j,k}^\infty, \\ \mathbb{T}_{pa,m}^* &= \min_j \{\mathbb{T}_{pa,j}\}, \quad \mathbb{T}_{pst,m}^* = \min_j \{\mathbb{T}_{pst,j}\} \end{aligned} \quad (4.26)$$

$$\Lambda_1(b_1, b_2, t) \triangleq (b_1 - b_2 e^{-\lambda t}) \mu(t - t_{k,i} - T_{pst,i}), \quad (4.27)$$

with $\mu(t)$ the unit step function, $\mathbb{K}_i s$, $\hat{\mathbb{K}}_i s$ for $i = 1, 2, 3, 4$ positive constants (see [59] for the expressions of $\mathbb{K}_i s$ and $\hat{\mathbb{K}}_i s$), and

$$\alpha < \min | -\operatorname{Re}(z_{s,i}(\Sigma))|, \quad \beta < \min |\operatorname{Re}(z_{us,i}(\Sigma))|,$$

where $z_{s,i}(\Sigma)$ and $z_{us,i}(\Sigma)$ are the minimum phase and nonminimum-phase zeros of system (4.1), respectively, and $\operatorname{Re}(z)$ denotes the real part of a complex number z .

The above Theorem 4 shows that the tracking error caused by the finite pre- and post-actuation times at all previous decomposition instants, although accumulates along with the output tracking course, exponentially decays with the increase of the length of pre- and post-actuation times at each decomposition instant, and thereby, can be rendered arbitrarily small by having a large enough pre- and post-actuation times at all decomposition instants (see Eqs. (4.24), (4.25)). Note in practice, there virtually is no limit on the length of post-actuation time (the allowable post-actuation time is only limited by the memory size of the control hardware), while the length of the pre-actuation time is limited by the available preview time. Thus, we assume, with no loss of generality, that the length of the preview time is larger than the pre-actuation time throughout the tracking course, i.e.,

$$T_p \geq T_{pa,m}^*, \quad \text{for } m = 1, 2, \dots \quad (4.28)$$

Note the requirement of large enough preview time in (4.28) is not the constraint of the BSD technique, but arises from the non-minimum phase nature of the system dynamics [3].

We further quantify the tracking precision by accounting for noise and other disturbances existing in practical implementations. We consider that the practically achievable desired input element, $u_{i,k}^a(\cdot)$, will track output element in the library, \mathcal{L}_e , with the tracking error bounded by a known constant ϵ_e , i.e., for $\forall k = 1, \dots, q$, and $i = 1, \dots, N_L$,

$$\|y_{k,i}^a(\cdot) - y_{k,i}^*(\cdot)\|_2 \leq \epsilon_e, \quad (4.29)$$

where $y_{k,i}^a(\cdot)$ is the output obtained by using $u_{i,k}^a(\cdot)$, and $\|y(\cdot)\|_2$ is the standard 2-norm of $y(\cdot) : \mathbb{R} \rightarrow \mathbb{R}$. Furthermore, with the use of uniform B-spline elements, there are at most $s + 1$ number of input elements summed together at any given time instant. Thus, the tracking precision of the BSD technique in practical implementations can be quantified.

Lemma 7 *Let conditions in Theorem (4) be satisfied, and the practically achievable desired input element be specified by (4). Also, let the pre- and post-actuation times $\mathbb{T}_{pa,1}$ and \mathbb{T}_{pst,N_k} be as in Theorem (4). Then at any given time instant t_c , the tracking error of using the synthesized input is bounded as*

$$\begin{aligned} \|E_y^a(t)\|_2 &\leq \|E_y(t)\|_2 + \left(\sum_{k=1}^q \|e_{y,k}^a(t)\|_2^2 \right)^{1/2}, \quad \text{with} \\ \|e_{y,k}^a(t)\|_2 &\leq \sum_{j=1}^{s+1} |p_{k,j}| \epsilon_e, \end{aligned} \quad (4.30)$$

where $p_{k,j}$ are the coefficients of the output elements used in the decomposition of the previewed desired output in the k^{th} output channel at time instant t .

4.3 Nanomanipulation Experimental Example

In this section, we implement the BSD technique to the output tracking involved in nanomanipulation applications in experiment using a SPM system (manufactured by Dimension Icon, Bruker Inc.). The objective of the experiments is to demonstrate that by using the BSD technique, precision tracking with preview at much higher speeds than that by using feedback control alone can be achieved.

4.3.1 Experiment Scheme

Preview-based output tracking is needed in nanomanipulation, where a micro-machined cantilever probe driven by piezoelectric actuators is utilized to manipulate nanoscale subjects, both horizontally and perpendicularly, for example, to build integrated circuit using nanotubes [40]. As the desired output trajectory during nanomanipulation usually is not pre-specified but online generated instead (by the user via, e.g., a haptic device), preview-based approach becomes a nature choice to output tracking, particularly at high-speed. Similar precision output tracking with preview also exists in areas such as nanofabrication. We focus, in the following, on x - y axes precision tracking in planar nanomanipulation.

The SPM hardware has been modified so that the PID controller of the SPM system was by-passed and all x - y - z axes displacement sensors and corresponding driven signals can be directly accessed. All the control inputs were generated by using the MATLAB-xPC-target (Mathworks, Inc.), and sent through a data acquisition system to drive the corresponding piezo-tube actuators (via a high-voltage amplifier).

Two English letters “RU” were chosen as the desired pattern to track. Output tracking of three different pattern-tracking rates (1.1 Hz, 11 Hz and 55 Hz) and two different pattern sizes (5 μm and 80 μm) were examined in the experiments, where the pattern-tracking rate was defined as the frequency to traverse the whole pattern once, and the pattern size was the larger displacement range among the x -, y -axes. The preview time of 0.1s, 0.01s, and 0.002s for the pattern-tracking rate of 1.1 Hz, 11 Hz, and 55 Hz, respectively, were selected to ensure that the amount of preview time with respect to the total tracking time (i.e., remained the same the ratio of the preview time to the total tracking time) remained the same. Such a choice of preview time reflected that in practical implementations, often it is the length of previewed path or contour, not the length of preview time, that is fixed (for example, the sensor performance). In the experiment, a different library was constructed for the output tracking of each pattern-tracking rate, so that the previewed output trajectory can be decomposed by the same number of output elements (seven output elements) to attain the same decomposition precision at each decomposition instant. Alternatively, a library constructed by using fast-enough output elements (e.g.,

the fastest library among the three) can be used for the output tracking of all the three pattern-tracking rates, i.e., a larger number of output elements were involved in the tracking of lower rates—for the tracking at the pattern-tracking rate of 1.1 Hz and 11 Hz, when using the library constructed for the pattern-tracking rate of 55 Hz, the number of output elements needed at each decomposition instant was at 203 and 23, respectively. The desired pattern for the pattern-tracking rate of 1.1 Hz and pattern size of $5\ \mu\text{m}$, and the corresponding desired x - and y -axis trajectories are shown in Fig. 4.3 (a), (b), (c), respectively.

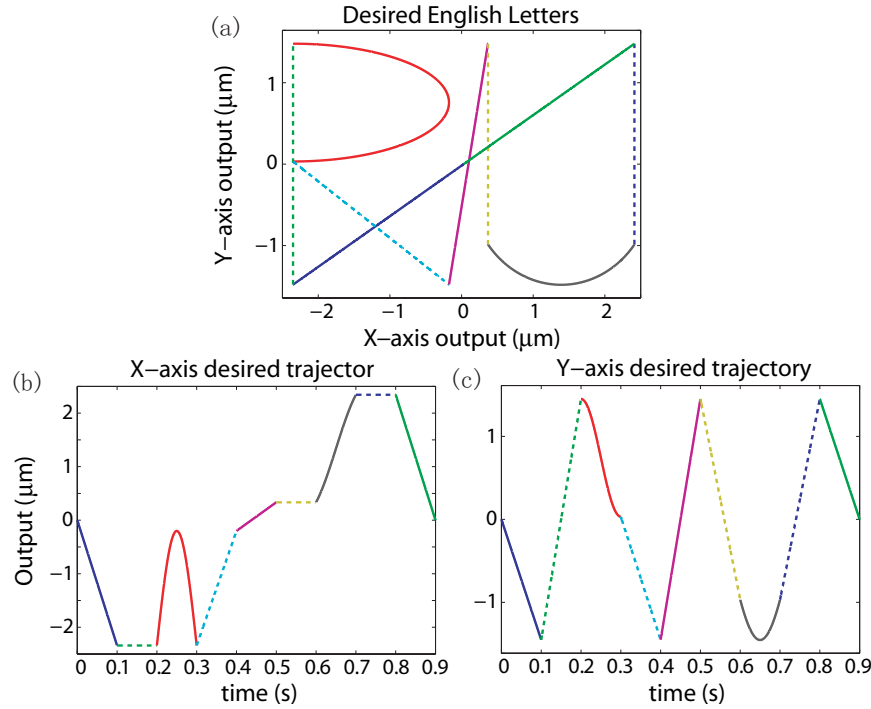


Figure 4.3: (a) The desired pattern to track in the nanomanipulation experiment, and the corresponding (b) x -axis and (c) y -axis desired trajectory, where the colors and types of the line mark the decomposition instant (beginning point of each line segment) and the portion of the previewed output trajectory to be decomposed at that instant.

4.3.2 Implementation of the Trajectory-Decomposition-Based Output Tracking

Library Construction

The 3^{rd} degree uniform B-splines were used to construct the library, and the total knots number was chosen at $m = 5$. To obtain the corresponding input element to track each output element

in the library \mathcal{L}_e , the MAIIC control technique below was employed [56],

$$\hat{U}_k(j\omega) = \hat{U}_{k-1}(j\omega) + \rho(j\omega)G_{I,md}^{-1}(j\omega)(\hat{Y}_d(j\omega) - \hat{Y}_{k-1}(j\omega)) \quad (4.31)$$

for $k \geq 1$, and $\hat{U}_0(j\omega) = 0$ initially, where $G_{I,md}$ is a diagonal matrix with diagonal elements being the model of the diagonal subsystems of system $G(j\omega)$,

$$G_{I,md}(j\omega) = \text{diag} [G_{11,md}(j\omega), G_{22,md}(j\omega)], \quad (4.32)$$

$$\rho(j\omega) = \text{diag} [\rho_1(j\omega), \rho_2(j\omega)] \quad (4.33)$$

with $\rho_1(j\omega)$ and $\rho_2(j\omega) \in \mathbb{R}^+$, and,

$$\begin{aligned} \hat{U}_k(j\omega) &= [\hat{u}_{1,k}(j\omega), \hat{u}_{2,k}(j\omega)]^T, \\ \hat{Y}_k(j\omega) &= [\hat{y}_{1,k}(j\omega), \hat{y}_{2,k}(j\omega)]^T. \end{aligned} \quad (4.34)$$

To implement the MAIIC technique (to obtain the input elements), the two diagonal subdynamics (x -to- x and y -to- y direction) along with the other two cross-axis coupling dynamics (y -to- x and x -to- y direction) were experimentally measured, as shown in Fig. 4.4 (a), (b), respectively. To quantify the dynamics uncertainty, frequency responses under different conditions (different driven input levels, 40 mV, 60 mV, and 80 mV, respectively) were acquired for the frequency range of $\omega \in [50 \ 4000]$ Hz for the x - and y -axis, respectively.

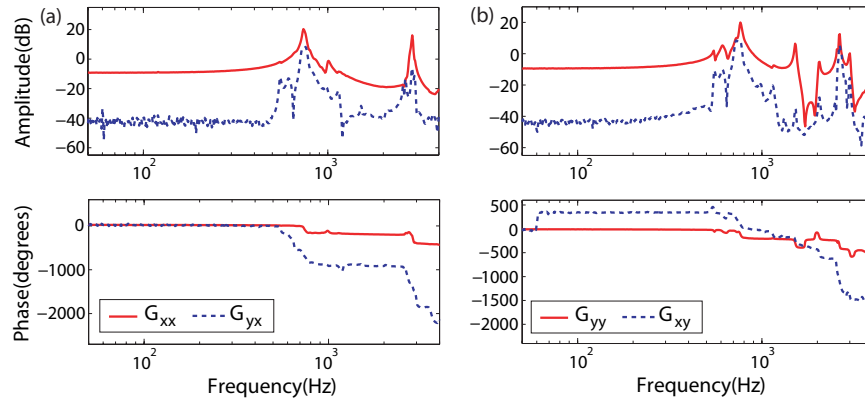


Figure 4.4: Comparison of the frequency responses of the (a) x -axis and (b) y -axis piezo actuator dynamics and the related coupling dynamics.

As shown in Fig. 4.4, both the x -axis and the y -axis dynamics were minimum-phase system. Thus, no pre-actuation time was needed when implementing the BSD technique. Thus, only the effect of finite post-actuation time was evaluated in the experiments. Note that as the effect

of the pre-actuation time is *dual* to that of the post-actuation time, the effect of the pre-actuation time on the tracking of nonminimum-phase system can be equally evaluated and appreciated from the post-actuation time effect demonstrated in the experiment results presented below.

As shown in Fig. 4.4, the cross-axis coupling effects were small between the x - y axes in the frequency range of $\omega < 700$ Hz. Thus, the lateral coupling caused disturbances between x - and y -axis were ignored in the experiments when designing the feedback controller for the x - and y -axis closed-loop. (Note that the MAIIC technique, however, can account for the coupling-dynamics without using the cross-coupling dynamics (see Eq. (5.5))). Output tracking of two of the seven output elements of the library \mathcal{L}_e are shown in Fig. 4.5.

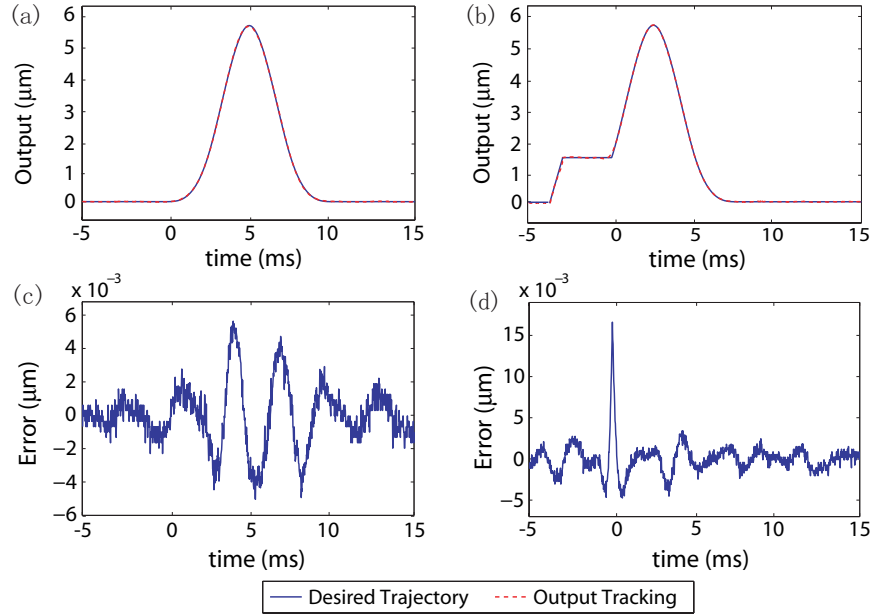


Figure 4.5: (a, b) Tracking of two of the output elements in the library \mathcal{L}_e and (c, d) the corresponding tracking error.

We note that the effect of hysteresis and creep effects of piezo actuators can be pronounced [9], particularly when the displacement range is large and/or the tracking time is long, i.e., the piezo actuators cannot be treated as a LTI system. Our experiment results obtained by directly implementing the BSD technique to the x - y axes piezo actuators showed that the hysteresis and creep caused tracking errors were significant. Thus, a feedback controller consisting of a proportional-integral (PI) controller followed by a notch filter was designed and applied to compensate for the hysteresis and creep effects. Particularly, the following notch filter was applied to account for the main resonant frequency of the x -axis and y -axis piezo actuators

(around 750 Hz), respectively,

$$\begin{aligned} G_{N_x}(s) &= \frac{s - 2\pi(-69.5 + 4633.3j)}{s - 2\pi(-1977.9 + 4532j)} \times \frac{s - 2\pi(-69.5 - 4633.3j)}{s - 2\pi(-1977.9 - 4532j)}, \\ G_{N_y}(s) &= \frac{s - 2\pi(-74.0 + 4934.3j)}{s - 2\pi(-2229.3 + 5107.9j)} \times \frac{s - 2\pi(-74.0 - 4934.3j)}{s - 2\pi(-2229.3 - 5107.9j)}. \end{aligned} \quad (4.35)$$

and the following PI controllers were implemented for the x - and y -axes feedback control loop, respectively,

$$G_{c_x}(s) = 0.5 - \frac{4000}{s}, \quad G_{c_y}(s) = 0.5 - \frac{4000}{s} \quad (4.36)$$

where the gain of the PI controller were experimentally tuned. The Bode-plots of the closed-loop system (consisting of the PI-Notch filter controller) for the x -axis and that for the y -axis are shown in Figs. 4.6 and 4.7, respectively.

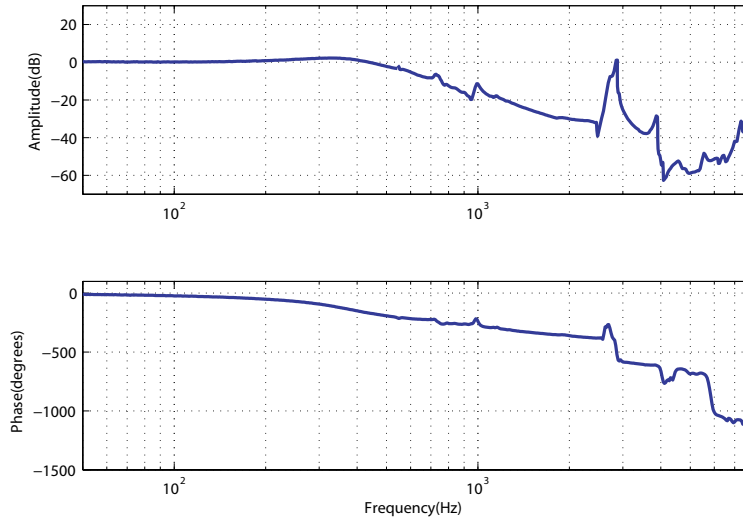


Figure 4.6: The Bode-plot of the x -axis closed-loop feedback control system consisting of the PI-Notch-filter controller.

Once the PI-Notch-filter feedback loop was formed, the BSD approach was applied to the closed-loop system in the pattern tracking with preview (see Fig. 4.8).

Desired Trajectory Decomposition

At each decomposition instant, the output elements in the Library (obtained in 4.3.2) were used to decompose the previewed desired trajectory. Particularly, five equispaced knots were used in

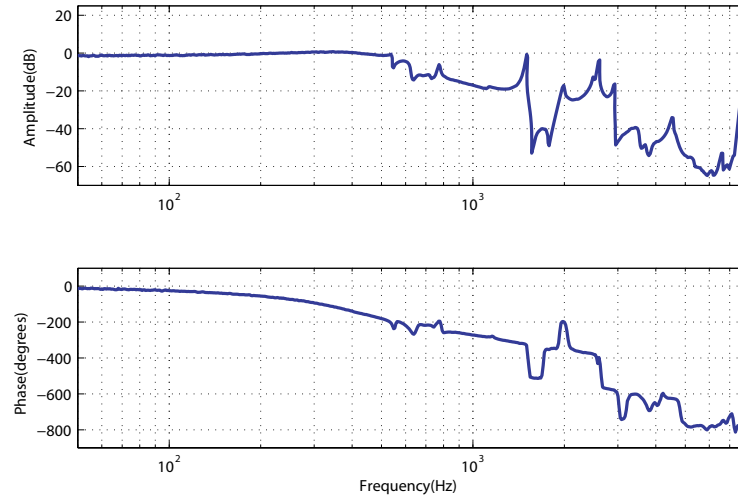


Figure 4.7: The Bode-plot of the y -axis closed-loop feedback control system consisting of the PI-Notch-filter controller.

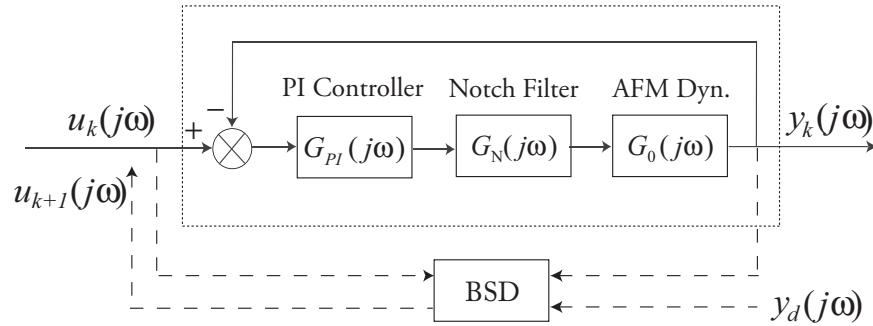


Figure 4.8: Block diagram of the implementation of the BSD technique on a PI-Notch-Filter feedback system.

decomposing each previewed desired trajectory. The x - y axes desired trajectories for the English letters (See Fig. 4.3 (b), (c)) were decomposed by using the 7 different output elements. The relative RMS error of the decomposition was below 0.001%, over 500 times smaller than the measured noise level.

Online Input Synthesis

At each decomposition instant, the control input for tracking the decomposed desired trajectory was synthesized by adding together the input elements corresponding to the output elements employed in the decomposition at that instant (see Eq. (4.21)), and truncated with the chosen post-actuation time. To simplify the presentation, the same post-actuation times across all

decomposition instants were used in the experiments. Two different post-actuation times ($T_{pst} = 1$ ms and $T_{pst} = 50$ ms) were used in the experiments to demonstrate and evaluate the effect of the finite post-actuation time on the tracking performance. Finally, the control input was updated according to Eq. (4.23).

4.3.3 Experimental Tracking Results and Discussion

First, to demonstrate the compensation for the hysteresis and creep effects, the BSD techniques was applied to the x -axis output tracking with and without the PI-notch-filter feedback, respectively. The tracking results for the pattern tracking rate of 11 Hz are compared in Fig. 4.9.

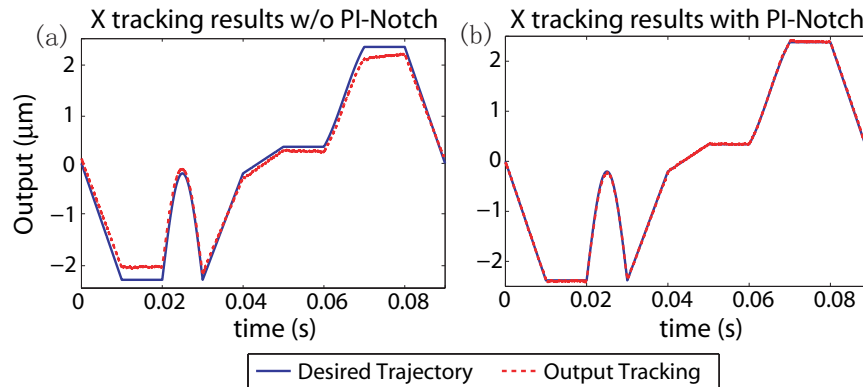


Figure 4.9: x -axis output tracking (a) without and (b) with the PI-Notch filter.

Then, to evaluate and demonstrate the efficacy of the BSD technique over feedback control alone, the BSD technique was applied to the PI-notch-filter feedback system of the x axis and y -axis, respectively, with a long enough post actuation time ($T_{pst} = 50$ ms). For comparison, the desired “RU” pattern was also tracked by using the PI feedback control alone, i.e., the desired trajectory of x -axis and that of y -axis was applied as the input to the respective PI-feedback closed-loop directly, respectively.

The tracking results of both the x -axis and the y -axis obtained by using the above two methods were acquired and compared. In Figs. 4.10 and 4.11, the lateral x - y axes and composed “RU” pattern tracking results obtained by using the two methods are compared for the three pattern tracking rates, respectively. The tracking error by using the two control methods are also compared in Table 4.1 in 2-norm and infinity-norm. Furthermore, in order to demonstrate the compensation effects for the drift and system nonlinearity, the tracking results for the lateral

x-y axes and composed RU pattern at at large size ($80 \mu\text{m}$) by using the two methods were also compared in Figs. 4.12 and 4.13 and Table 4.2.

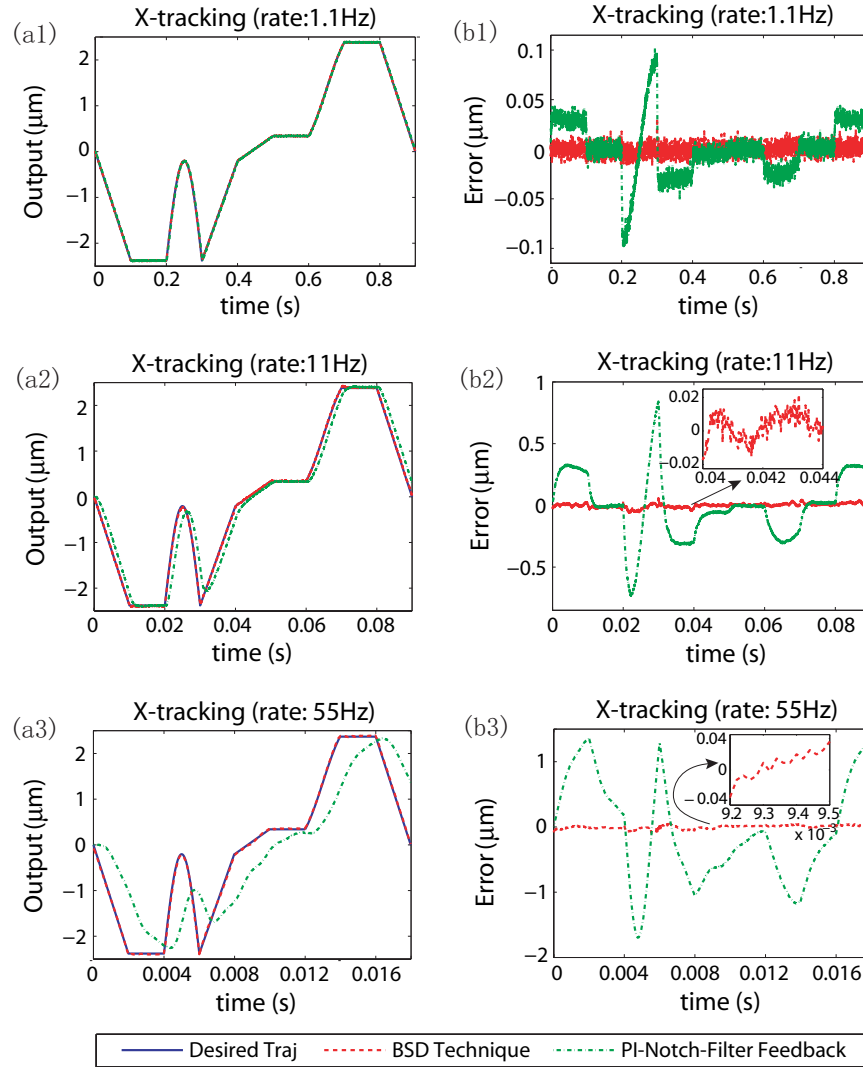


Figure 4.10: Comparison of the x -axis ($5 \mu\text{m}$) output tracking results obtained by using the BSD technique with those by using the PI control method at (a1) 1.1 Hz, (a2) 11 Hz, and (a3) 55 Hz, and comparison of the corresponding tracking errors at (b1) 1.1 Hz, (b2) 11 Hz, and (b3) 55 Hz, respectively.

The x -axis tracking results of pattern size $5 \mu\text{m}$ obtained with the two chosen post-actuation times $T_{pst,j} = 1 \text{ ms}$ and 50 ms are compared in Fig. 4.14. Moreover, the tracking of the “RU” pattern are also compared in Fig. 4.15 for the post-actuation times of $T_{pst,j} = 1 \text{ ms}$ and 50 ms , respectively.

The experimental results show that by using the BSD technique, precision output tracking

Table 4.1: Comparison of x -axis output tracking error by using the BSD and the PI feedback methods, where $E_2(\%)$ and $E_\infty(\%)$ denote the in 2-norm error $E_2(\%)$ and infinity-norm $E_\infty(\%)$.

$5\mu\text{m}$	1.1 Hz		11 Hz		55 Hz	
	BSD	PI	BSD	PI	BSD	PI
$E_2(\%)$	0.354	1.881	1.111	17.109	1.783	56.371
$E_\infty(\%)$	1.485	4.362	3.037	34.997	3.865	72.707

Table 4.2: Comparison of X -axis output tracking error by using the BSD and the PI feedback methods, where $E_2(\%)$ and $E_\infty(\%)$ denote the in 2-norm error $E_2(\%)$ and infinity-norm $E_\infty(\%)$.

$80\mu\text{m}$	1.1 Hz		11 Hz		55 Hz	
	BSD	PI	BSD	PI	BSD	PI
$E_2(\%)$	0.431	1.256	3.164	12.387	9.654	54.944
$E_\infty(\%)$	1.301	3.559	10.488	26.003	18.713	67.684

can be maintained throughout the entire output tracking course. Although when the pattern-tracking rate was low (1.1 Hz), relatively good tracking can be obtained by using the feedback control alone, the tracking precision of using the BSD technique was substantially higher than that of using feedback alone (see Fig. 4.10 (a1), (b1)). The x -axis relative RMS tracking error $E_2(\%)$ of the BSD technique at 0.35% was over 5 times smaller than that of using the feedback alone at 1.88%. Even when the pattern-tracking rate became much higher at 55 Hz, almost the same tracking precision (with $E_2(\%) < 2\%$) can still be maintained by using the BSD technique, whereas the output tracking using PI feedback control was completely lost (see Fig. 4.10 (a3), (b3)). For example, the x -axis relative tracking error of the BSD technique in 2-norm was over 30 times smaller than that of the feedback alone. The improvement achieved by using the BSD technique over feedback alone was more evident in the “RU” pattern generated (see Fig. 4.11), particularly when the tracking rate (speed) was high (see Fig. 4.11 (a3), (b3) for the pattern-tracking rate of 55 Hz). Therefore, the experimental results demonstrate the superior tracking performance of the BSD technique over feedback, particularly during high-speed tracking.

The experimental results also demonstrated that the efficacy of the BSD technique in achieving high-speed precision trajectory tracking during large-range nanopositioning application. When the pattern size became much larger at $80\mu\text{m}$, the tracking performance of the BSD technique can be maintained as that during the small size tracking (e.g. $5\mu\text{m}$)—at the pattern

tracking rate of 11 Hz, the relative RMS tracking error $E_2(\%)$ in x axis was about 3.16% for 80 μm pattern size, comparable to that at the pattern size of 5 μm at 1.11% (see Fig. 4.10 (a2), (b2) and 4.12 (a2), (b2)). We note that the tracking error increased as the pattern tracking rate increased (See Fig. 4.12 and Table 4.2), even though the same tracking precision of the output elements was maintained (as that in the 5 μm pattern size). Such an increase of the tracking error reflected the hysteresis and other random effects—As the displacement range increased by 16 times, the hysteresis effect was much more pronounced, and as a result, the closed-loop feedback control system was less “linear”. However, the tracking performance was still substantially improved by using the BSD technique over feedback alone: The tracking error (in $E_2(\%)$) at the pattern tracking rate of 55 Hz was 6 times smaller than that by using feedback alone (as shown Fig. 4.12 and Table 4.2). Therefore, our experiments showed that by using the BSD technique along with feedback, both hysteresis and creep effects can be effectively compensated for in large-range, high-speed nanomanipulation applications.

The effect of the post-actuation time on the tracking performance is also evident from the experimental results. The tracking error was small when the post-actuation time was long enough. As shown in Figs. 4.10 to 4.13, precision tracking was maintained at all three pattern tracking rates when the post-actuation time was large at $T_{pst} = 50$ ms, whereas the output tracking error increased substantially when the post-actuation time was shortened to $T_{pst} = 1$ ms (see Fig. 4.14 (a), (c) and Fig. 4.15 (a), (c)). Therefore, by the *dual* effect of the post-actuation time for minimum-phase systems to that of the pre-actuation time for nonminimum-phase systems, the experimental results demonstrated that precision output tracking of nonminimum-phase systems can be achieved by using the BSD technique with a sufficiently large pre-actuation time.

4.4 Conclusions

In this chapter, a B-spline-decomposition-based (BSD) control approach was implemented to achieve precision output tracking in high-speed nanomanipulation. A PI-notch-filter feedback controller was employed to compensate for the hysteresis and creep effects and improved the

linearity of the control system, and then the BSD technique was utilized to enhance the tracking performance. The experimental results demonstrated that by using the BSD technique, the tracking precision during high-speed output tracking can be substantially improved over feedback control alone, even in the presence of significant hysteresis effect. The effect of finite post-actuation time on the tracking performance was also investigated and illustrated in the experiments.

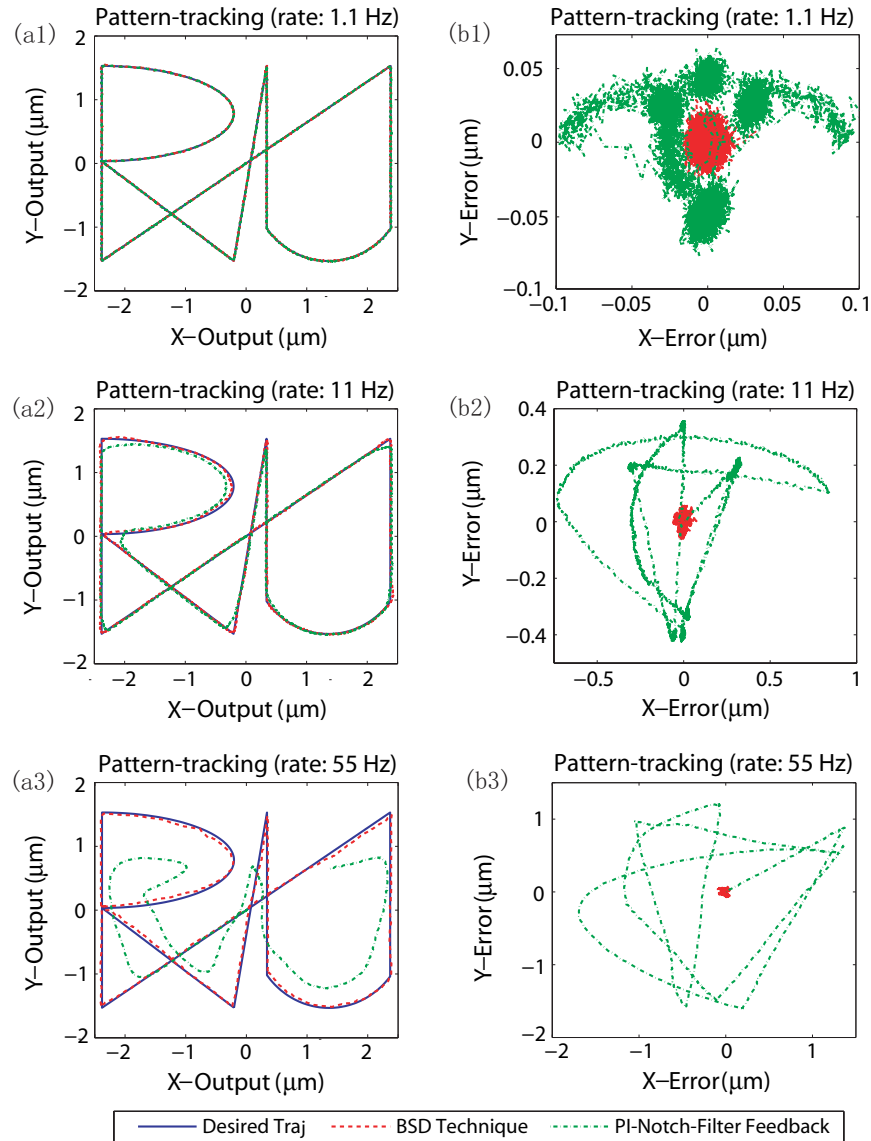


Figure 4.11: Comparison of the RU pattern ($5 \mu\text{m}$) tracking results obtained by using BSD method with those by using the PI control method at (a1) 1.1 Hz, (a2) 11 Hz, and (a3) 55 Hz, and comparison of the corresponding tracking errors at (b1) 1.1 Hz, (b2) 11 Hz, and (b3) 55 Hz, respectively.

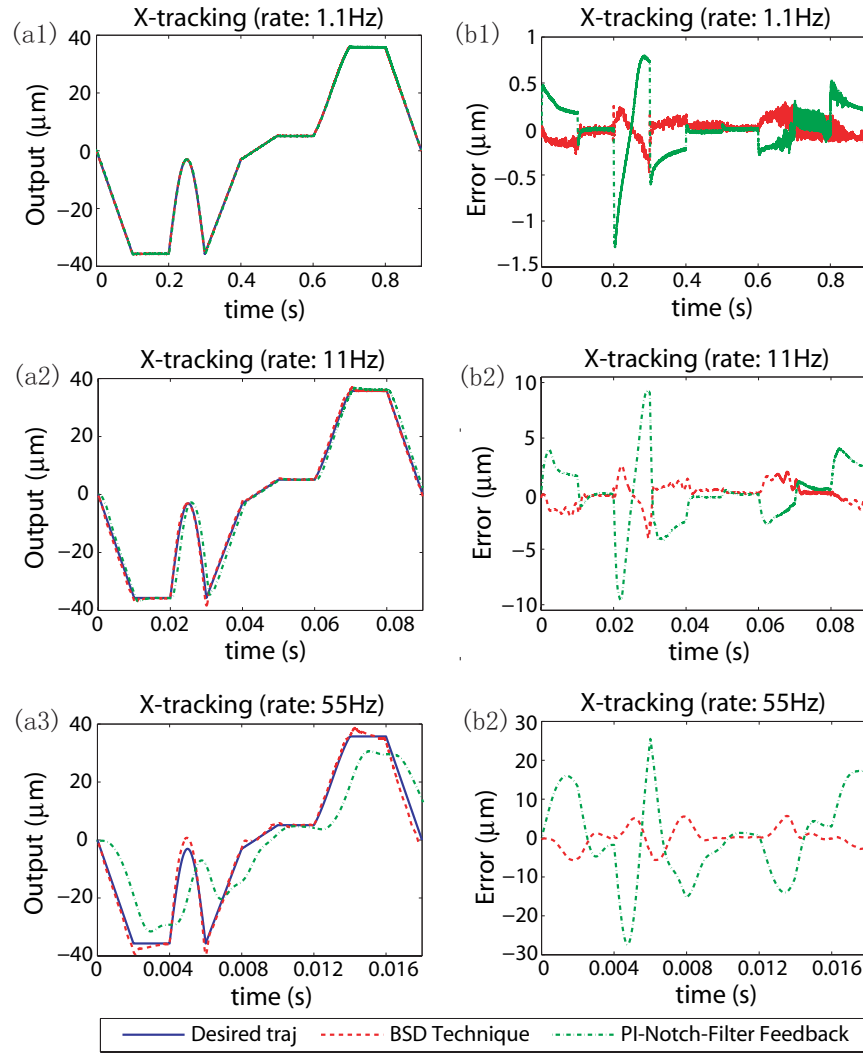


Figure 4.12: Comparison of the x -axis ($80 \mu\text{m}$) output tracking results obtained by using BSD method with those by using the PI control method at (a1) 1.1 Hz, (a2) 11 Hz, and (a3) 55 Hz, and comparison of the corresponding tracking errors at (b1) 1.1 Hz, (b2) 11 Hz, and (b3) 55 Hz, respectively.

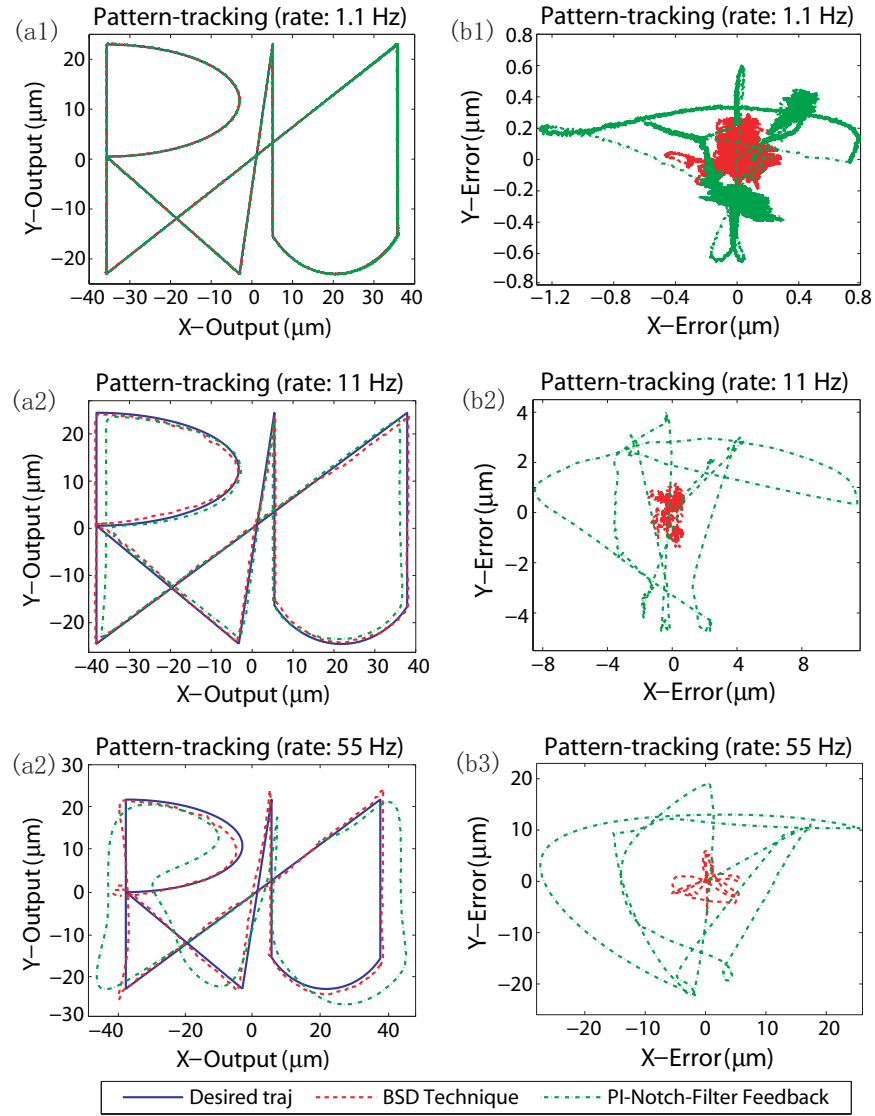


Figure 4.13: Comparison of the RU pattern (80 μm) tracking results obtained by using BSD method with those by using the PI control method at (a1) 1.1 Hz, (a2) 11 Hz, and (a3) 55 Hz, and comparison of the corresponding tracking errors at (b1) 1.1 Hz, (b2) 11 Hz, and (b3) 55 Hz, respectively.

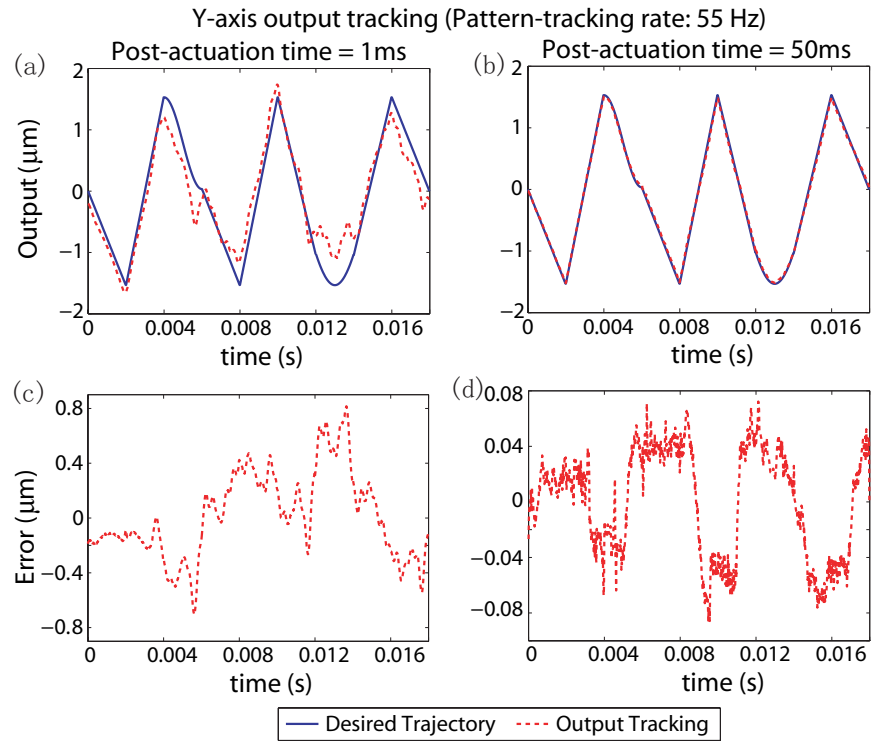


Figure 4.14: Comparison of (upper row) the y -axis output tracking and (lower row) the tracking error obtained by using the proposed technique with post-actuation time of (left column) $T_{pst} = 1$ ms and (right column) $T_{pst} = 50$ ms.

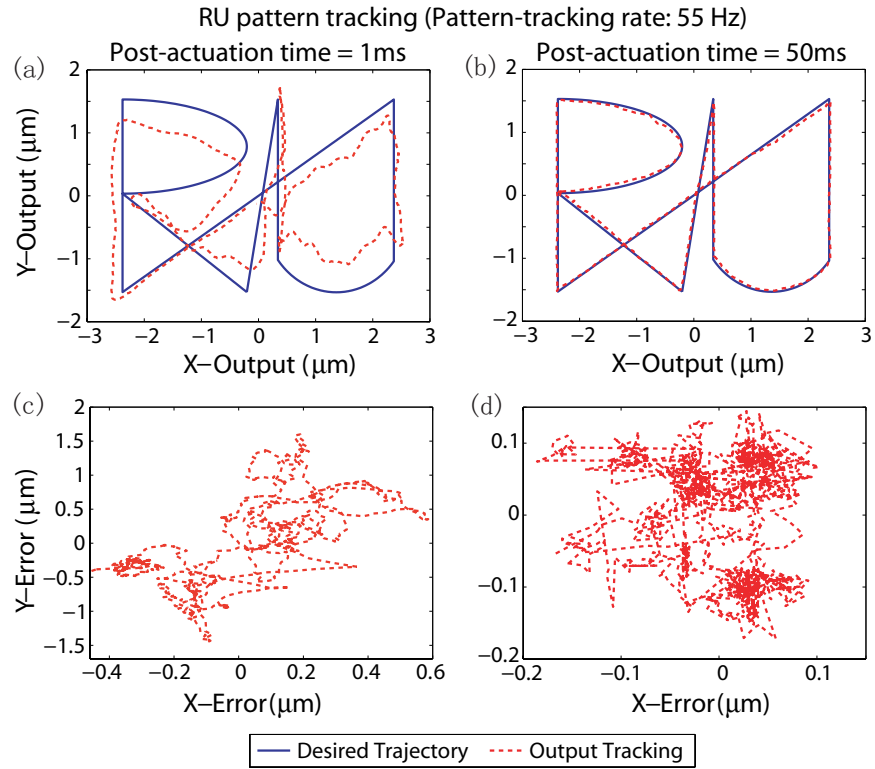


Figure 4.15: Comparison of (upper row) the pattern tracking and (lower row) the tracking error obtained by using the proposed technique with post-actuation time of (left column) $T_{pst} = 1$ ms and (right column) $T_{pst} = 50$ ms.

Chapter 5

High-speed Probe-based Nanofabrication via an Iterative Control Approach for Multi-axis Precision Tracking

Abstract

In this chapter, the multi-axis inversion-based iterative control (MAIIC) approach is utilized to achieve high-speed, large-range probe-based nanofabrication. Probe-based nanofabrication has attracted great interests recently. This technique, however, is still limited by its low throughput, due to the challenges in compensating for the existing adverse effects. These adverse effects include the nonlinear hysteresis as well as the vibrational dynamics of piezoactuators used to position the probe in 3-D axes, and the dynamics coupling in multi-axis motion during high-speed nanofabrication. The main contribution of this chapter is the utilization of the recently developed multi-axis inversion-based iterative control (MAIIC) technique to overcome these challenges in probe-based nanofabrication. By using this advanced control technique, precision position control of the probe with respect to the sample substrate can be achieved during high-speed, large-range multi-axis nanofabrication. Particularly, the cross-axis dynamics coupling effect on the output tracking can be compensated for during the iterative learning process with no additional steps to learn the cross-coupling effect separately. The proposed approach is illustrated through experiments by implementing it to fabricate two Chinese characters pattern via mechanical scratching on a gold-coated silicon sample surface at high speed. The efficacy of the proposed technique is demonstrated through the experimental results that precision tracking in all 3-D axes can be achieved in the presence of pronounced cross-axis dynamics coupling effect.

5.1 Introduction

This chapter illustrates and demonstrates the multi-axis inversion-based iterative control (MAIIC) approach to achieve high speed and large range in probe-based nanofabrication. Currently, one of the main challenges in probe-based nanofabrication technology is its low throughput. Efforts to increase the throughput of probe-based nanofabrication can be categorized into two groups—the parallel-probe approach and the increase of operation speed [72, 73, 74]. For parallel-probe approach, the increase of system complexity inevitably results in issues related to the increase of the cost, the uniformity and the robustness. Moreover, the throughput of the parallel system is eventually limited by the low-speed operation [64]. On the other hand, large positioning errors can be generated during high-speed, large-range fabrication, and the cross-axis dynamics coupling of piezoactuators can become large, resulting in large fabrication distortions as well. The contribution of this chapter is the utilization of a recently developed multi-axis inversion-based iterative control (MAIIC) approach [56] to compensate for the adverse hardware effects, arriving at high-speed probe-based nanofabrication.

Precision positioning during high-speed large-range motion is very critical in probe-based nanofabrication (PBN). Probe-based fabrication of nanoscale structures and devices is very promising because of the low cost and significant technical potential [62]. Although the underline mechanisms in various PBN methods can be different [56, 64, 72, 73, 74, 75], these methods all require precision positioning of the probe relative to the sample and thereby, are confronted by the same challenge in maintaining precision (probe-to-sample) positioning during high-speed, large-range operation. Large (probe-to-sample) positioning errors not only lead to large defects in the fabricated structures or devices, but also result in damage of the probe (when the sample is hard), the sample (when the sample is soft), or both. Moreover, unlike the motion control in other probe-based nano-applications (such as SPM imaging) where one axis motion is substantially slower than that in other axes, the motion control in PBN can be very demanding in all x - y - z 3-D axes. Positioning errors in different axes can be accumulated and induce large distortions in the fabricated structure/device. Additional fabrication distortion is generated due to the cross-axis dynamics coupling of the piezo-actuators when the fabrication speed is high and/or the operation range is large. Therefore, it is essential to maintain the

precision positioning of the probe relative to the sample in all x - y - z axes during high-speed, large-size nanofabrication.

It is a challenge to maintain precision probe-sample positioning during high-speed, large range probe-based nanofabrication operations. Although nano- to atomic- level positioning precision can be achieved with the use of piezo-actuators, the vibration dynamics of the piezo-actuators can be excited during high-speed operations, resulting in large vibration-induced positioning errors. Moreover, when the displacement range becomes large, the effect of nonlinear hysteresis of piezo-actuators becomes pronounced, resulting in large positioning errors as well. During high-speed, large-range probe-based nanofabrication, these two effects are coupled and lead to even larger positioning errors [9, 62, 64, 75, 76]. Additional fabrication distortion can also be produced due to the cross-axis dynamics coupling between piezo-actuators in different axes when the fabrication speed is high and/or the operation range is large [11]. Therefore, control techniques are needed to effectively account for all these adverse effects to achieve high-speed probe-based nanofabrication with no loss of fabrication quality.

Advanced control techniques such as the inversion-based iterative control (IIC) techniques [9, 11, 34] can be utilized to achieve precision positioning during high-speed, large-range PBN operations. The IIC approach is ideal for PBN operations where the desired trajectory is usually specified a priori and the environment tends to be well maintained. These conditions allow the noncausality gained from the repetitive nature of the operation to be fully exploited in the IIC framework, particularly for nonminimum-phase systems such as the piezoactuators used in PBN applications [48]. It has been shown recently that the IIC approach can compensate for both hysteresis and dynamics effects of piezoactuators [9]. The multi-axis IIC (MAIIC) technique utilized in this chapter further extends the IIC approach [11] from single-axis positioning to multi-axis positioning. Such an extension of the MAIIC technique eliminates the additional procedure to identify and compensate for the coupling-caused positioning error separately that is needed in the previous work of using the IIC technique first [11, 77, 78]. The efficacy of the MAIIC algorithm for precision positioning has been demonstrated through experiments [56]. Therefore, it is advantageous to utilize iterative control techniques such as MIIC in probe-based nanofabrication.

The main contribution of this chapter is the implementation of the MAIIC technique to

the probe-based nanofabrication using SPM. Particularly, the MAIIC technique is utilized to achieve precision tracking of the desired trajectory in all x - y - z axes simultaneously, arriving at precision fabrication of the given pattern at high-speed. Particularly, two Chinese characteristics (“Na Mi”, meaning nanometer) were fabricated via mechanical scratching on a gold-coated silicon sample as an illustrative example. The experimental results show that the desired pattern can be accurately fabricated by using the proposed approach at high-speed (~ 1.3 mm/s) and over a relatively large fabrication size (~ 55 μ m by ~ 55 μ m), thereby, demonstrating the efficacy of the proposed approach for high-speed large-range PBN applications.

5.2 MAIIC approach to probe-based nanofabrication

In this section, the MAIIC control technique [56] is presented for PBN applications.

5.2.1 Cross-axis Coupling Effect on PBN Applications

The central idea of PBN technique is the precision positioning of a micro-machined probe is precisely on (or closely above) the same surface during the motion (see Fig. 5.1) to locally induce surface modification along the path, resulting in nanoscale features on the sample surface (such as lines or dots). Such a surface modification can be achieved, for example, through mechanical scratching followed by an etching process [79, 80], or, through thermal effects as exemplified in the IBM Millipede system [81]. Alternatively, probe-based nanofabrication can also be achieved by introducing external effects such as electrical fields [82], laser beams [83], and chemical compounds (via probe coating) [84].

We note that cross-axis dynamics-coupling effect generally exists in multi-axis motion control, including nanopositioning control [85, 11, 77] in PBN applications. Such cross-axis coupling arises due to factors such as the inevitable misalignment (albeit small) between the two lateral x - and y -axes, and/or the “bowing” effect between the lateral and the vertical axes (when piezoelectrical tube actuators are used) [77]. Such cross coupling effect becomes more pronounced during high-speed motion as the resonance of the actuators can be excited. In PBN

applications, the cross-axis dynamics coupling effect directly results in distortions in the fabricated patterns/devices— the lateral x - y coupling results in shape distortions, and the lateral-to-vertical coupling results in the depth and width irregularities. The effect of cross-axes coupling becomes even more serious when fabricating 3-D nano-structures, as the motions in all x - y - z axes can be complicated and high-speed. Therefore, the cross-axis coupling effect needs to be compensated for in PBN process.

5.2.2 Multi-axis Inversion based Iterative Control (MAIIC) Technique

The MAIIC approach [56] provides a straightforward and effective framework to compensate for the cross-axis dynamics coupling effect during high-speed PBN process. The cross-axis coupling effect can be compensated for by modeling the PBN system as a multi-input-multi-output (MIMO) system, and then design a MIMO controller accordingly by using, for example, the robust-control theory [86]. Such an approach, however, can be challenging to implement as the complexity of the controller can increase rapidly with the increase of the order of the system. Moreover, the performance of the general MIMO controller to compensate for the coupling effect is also limited by the inevitable compromise between the performance and the robustness upon dynamics uncertainties of the system [87]. Such a robustness-performance trade-off in cross-coupling compensation is avoided in [77, 78] — as the operation of PBN is repetitive, the coupling-caused motion is also, however, to remove the dynamics-coupling effect during high-speed PBN applications, the coupling-caused motion needs to be identified separately and tracked through an additional iteration process (in addition to the iteration process to track the desired trajectory). Such additional process is eliminated by using the MAIIC approach.

Next, we model the dynamics of a PBN system as a multi-input-multi-output (MIMO) system in the transfer function form, $G(j\omega) : \mathbb{C} \rightarrow \mathbb{C}^{n \times n}$,

$$\hat{Y}(j\omega) = G(j\omega)\hat{U}(j\omega), \quad (5.1)$$

with the number of inputs equals to the number of outputs, i.e.,

$$G(j\omega) = \begin{bmatrix} G_{11}(j\omega) & G_{12}(j\omega) & \cdots & G_{1n}(j\omega) \\ G_{21}(j\omega) & G_{22}(j\omega) & \cdots & \vdots \\ \cdots & \cdots & \ddots & \vdots \\ G_{n1}(j\omega) & \cdots & \cdots & G_{nn}(j\omega) \end{bmatrix} \quad (5.2)$$

and

$$\begin{aligned} \hat{Y}(j\omega) &= [\hat{y}_1(j\omega), \hat{y}_2(j\omega), \cdots, \hat{y}_n(j\omega)]^T, \\ \hat{U}(j\omega) &= [\hat{u}_1(j\omega), \hat{u}_2(j\omega), \cdots, \hat{u}_n(j\omega)]^T, \end{aligned} \quad (5.3)$$

Then, the MAIIC law is given in frequency domain as follows,

$$\begin{aligned} \hat{U}_0(j\omega) &= 0 \\ \hat{U}_k(j\omega) &= \hat{U}_{k-1}(j\omega) + \rho(j\omega) G_{I,k}^{-1}(j\omega) (\hat{Y}_d(j\omega) - \hat{Y}_{k-1}(j\omega)) \end{aligned} \quad (5.4)$$

for $k = 1, 2, \cdots$, where $G_{I,m}^{-1}(j\omega)$ is a diagonal matrix with the diagonal elements being the model of the diagonal subsystems of system $G(j\omega)$,

$$G_{I,m}(j\omega) = \text{diag} [G_{11,m}(j\omega), G_{22,m}(j\omega), \cdots, G_{nn,m}(j\omega)], \quad (5.5)$$

and

$$\rho(j\omega) = \text{diag} [\rho_1(j\omega), \rho_2(j\omega), \cdots, \rho_n(j\omega)] \quad (5.6)$$

is the frequency-dependent iteration coefficient matrix where the diagonal element $\rho_p(j\omega) \in \mathbb{R}^+$ for each $p = 1, 2, \cdots, n$. In (5.4), $\hat{U}_k(j\omega)$ and $\hat{Y}_k(j\omega)$ denote the input and the output of the system in the k^{th} iteration, respectively (see Fig. 5.1),

$$\begin{aligned} \hat{Y}_k(j\omega) &= [\hat{y}_{1,k}(j\omega), \hat{y}_{2,k}(j\omega), \cdots, \hat{y}_{n,k}(j\omega)]^T, \\ \hat{U}_k(j\omega) &= [\hat{u}_{1,k}(j\omega), \hat{u}_{2,k}(j\omega), \cdots, \hat{u}_{n,k}(j\omega)]^T. \end{aligned} \quad (5.7)$$

5.2.3 Design of the MAIIC Law

The design of the MAIIC law (5.4) involves the selection of the iterative coefficient matrix $\rho(j\omega)$ (5.6) to guarantee the convergence of the iteration process at given frequency ω , and

consequently, identify and quantify the frequency range over which the convergence can be guaranteed.

$$\rho_p(j\omega) \in \begin{cases} (0, \kappa_p(j\omega)], & \omega \in \Omega_T \\ \{0\}, & \text{Otherwise.} \end{cases} \quad (5.8)$$
$$\Omega_T = \bigcap_{p=1}^n \Omega_p \quad (5.9)$$
$$\Omega_p \triangleq \{\omega \mid \mathbf{C}_{p,\text{sup}}(j\omega) < 1, \text{ and} \quad \angle \Delta\theta_{pp,\text{sup}}(j\omega) < \arccos(\mathbf{C}_{p,\text{sup}}(j\omega))\}, \quad (5.10)$$

and the upper bound of the iterative coefficient, $\kappa_p(j\omega)$ is

$$\kappa_p(j\omega) = \frac{2}{\Delta r_{pp,\sup}(j\omega)} \frac{\cos \Delta \theta_{pp,\sup}(j\omega) - \mathbf{C}_{p,\sup}(j\omega)}{1 - \mathbf{C}_{p,\inf}(j\omega)^2}. \quad (5.11)$$

where $\Delta r_{pp,\sup}(j\omega)$, $\Delta \theta_{pp,\sup}(j\omega)$, $\mathbf{C}_{p,\sup}(j\omega)$, and $\mathbf{C}_{p,\inf}(j\omega)$ are the constants that quantify the dynamics uncertainty and the cross-axis coupling effect in each p -axis, respectively,

$$\begin{aligned} \Delta r_{pp,\sup}(j\omega) &\triangleq \sup_{r,k \in \mathbb{N}} \left\{ \left| \frac{G_{pp,r}(j\omega)}{G_{pp,k}(j\omega)} \right| \right\} \\ \Delta \theta_{pp,\sup}(j\omega) &\triangleq \sup_{r,k \in \mathbb{N}} \left\{ \left| \angle \left(\frac{G_{pp,r}(j\omega)}{G_{pp,k}(j\omega)} \right) \right| \right\} \end{aligned} \quad (5.12)$$

and correspondingly, the infimum for the magnitude difference among the models is given by

$$\Delta r_{pq,\inf}(j\omega) \triangleq \frac{1}{\Delta r_{pq,\sup}(j\omega)} \quad (5.13)$$

With the above definitions, it is reasonable to assume that the “true” system dynamics uncertainty can be bounded as

$$\begin{aligned} \Delta r_{pq,\inf}(j\omega) &\leq |\Delta G_{pq}(j\omega)| \leq \Delta r_{pq,\sup}(j\omega), \\ |\angle \Delta G_{pq}(j\omega)| &\leq \Delta \theta_{pq,\sup}(j\omega). \end{aligned} \quad (5.14)$$

Accordingly, the bound (5.14) implies that the total cross-axis coupling dynamics effect on the p^{th} axis can be bounded as

$$\mathbf{C}_{p,\inf}(j\omega) \leq \mathbf{C}_p(j\omega) \leq \mathbf{C}_{p,\sup}(j\omega), \quad (5.15)$$

where,

$$\begin{aligned} \mathbf{C}_{p,\inf}(j\omega) &\triangleq \Delta r_{pp,\inf}(j\omega) \sum_{\substack{q=1, \\ q \neq p}}^n \Delta r_{pq,\inf}(j\omega) \inf_{\mathbf{s}_{pq}, \mathbf{s}_{pp}} \frac{|G_{pq,r}(j\omega)|}{|G_{pp,k}(j\omega)|} \\ \mathbf{C}_{p,\sup}(j\omega) &\triangleq \Delta r_{pp,\sup}(j\omega) \sum_{\substack{q=1, \\ q \neq p}}^n \Delta r_{pq,\sup}(j\omega) \sup_{\mathbf{s}_{pq}, \mathbf{s}_{pp}} \frac{|G_{pq,r}(j\omega)|}{|G_{pp,k}(j\omega)|} \end{aligned} \quad (5.16)$$

where $G_{pp,r}(j\omega)$ and $G_{pp,k}(j\omega)$ denote two acceptable models of the subdynamics $G_{pp}(j\omega)$ obtained in two different modeling processes.

Note that the model of the subdynamics $G_{pq}(j\omega)$ (see Eq. (5.2)) can be obtained through experiments, for example, by applying input to the p -axis input only and measuring the output response of the q -axis, and the obtained dynamics model can be different in different modeling

processes. The variation of the dynamics model for PBN system is caused by several issues. Due to the nonlinear hysteresis behavior existing in the piezoelectric actuators used in PBN systems, the subdynamics model $G_{pq,k}(j\omega)$ varies under different measurement conditions (e.g., with different input amplitudes and/or different offset of the initial position), i.e., the hysteresis effect on the vibrational dynamics of the piezoactuators is considered as the variation to the frequency response of the linear time invariant dynamics model. Additionally, the dynamics of the PBN system can also vary due to the operations, the changes of environment conditions, and other disturbances such as noises. Therefore, the constants given by Eq. (5.11) are introduced to account for these issues in the MAIIC framework.

5.3 Experimental Example

We illustrate the implementation of the MAIIC approach to probe-based nanofabrication through experiments. It is demonstrated that by using the MAIIC approach, high-speed nanofabrication of large size can be achieved. We start with briefly describing the nanofabrication process based on mechanical scratching.

5.3.1 PBN Experiment via Mechanical Scratching

The experiments were carried out under ambient conditions on a SPM system (Dimension 3100, Veeco Instruments Inc.) with a rectangular-shape cantilever coated with wear-resistant material. The nominal stiffness of the probe is 40 N/m (stiffer probes like the stainless steel cantilever with diamond tip can be used to further reduce wear and increase the smoothness of the fabricated pattern). By applying a relatively large loading force to the SPM probe on the sample surface, and dragging the probe to track the desired geometry path, patterns of nanoscale features can be fabricated. The fabricated pattern can be examined by imaging the sample surface using the same SPM system with a substantially lower loading force.

The SPM system utilized in this chapter uses piezotube actuators to position the SPM probe with respect to the sample in all x - y - z axes. All the control inputs were generated by using MATLAB-xPC-target (Mathworks, Inc.), and sent through a data acquisition card to drive the

high-voltage amplifiers for the corresponding piezotube actuators. In the following experiments, two Chinese characters “Na Mi” (meaning “nanometer”) were chosen as the desired pattern to be fabricated. During the fabrication process, the z -axis feedback control of the SPM system was turned off, and the vertical position of the z -axis piezo actuator was controlled by applying the feedforward input obtained from the MAIIC technique to track the desired z -axis trajectory. The fabrication of the chosen Chinese characters required the up-and-down vertical motion of the probe. Thus, such an experiment evaluated the MAIIC algorithm for fabricating 3-D structures. The desired pattern (size: $\sim 55 \mu\text{m}$ by $\sim 55 \mu\text{m}$) and the corresponding desired trajectories for z , x , and y axes are shown in Fig. 5.2 (a), (b), (c), and (d), respectively. Particularly, an isosceles trapezoidal wave was chosen as the desired z -axis waveform. The use of the isosceles trapezoidal wave rather than square wave was to reduce the oscillations after the up-down transitions (Fig. 5.2 (b)).

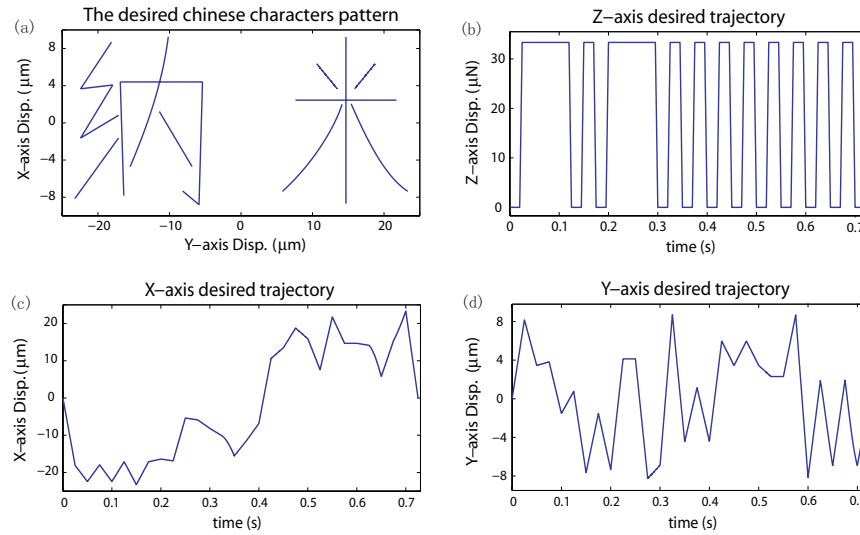


Figure 5.2: The desired trajectories of the Chinese characters pattern: (a) the entire trajectory, (b) the z -axis trajectory, (c) the x -axis trajectory, and (d) the y -axis trajectory.

5.3.2 SPM Dynamics Modeling and Uncertainty Quantification

The three diagonal subdynamics of the SPM system in $G_{11}(j\omega)$, $G_{22}(j\omega)$, and $G_{33}(j\omega)$ (i.e., the dynamics from the x -, y -, and z - axis input to the corresponding x -, y -, and z - axis output, respectively), were experimentally measured along with the six cross-axis coupling dynamics (the coupling dynamics in y -to- x , z -to- x , x -to- y , z -to- y , x -to- z and y -to- z directions). For

example, the diagonal subdynamics for the lateral x -axis measured by applying the input to the x -axis piezo actuator only, and measuring the corresponding output of the three axes, respectively, by using a dynamic signal analyzer (DSA, Hewlett Packard 356653A). The dynamics uncertainty was also experimentally quantified by measuring the frequency responses under different driven input levels (20 mV, 40 mV, and 60 mV), as shown in Fig. 5.3, 5.4, and 5.5 for the frequency range of $\omega \in [0, 3]$ KHz and $\omega \in [0, 5]$ KHz for the lateral axes and the vertical axis, respectively. Then the supremum and the infimum of the magnitude uncertainty and the phase uncertainty were estimated according to (5.12), and the upper bound of the iteration coefficient for each axis ($\kappa_x(j\omega)$, $\kappa_y(j\omega)$, $\kappa_z(j\omega)$) were quantified according to (5.11). The obtained upper bounds of the iteration coefficients for x , y and z axes and the iteration coefficients used in the experiments are shown in Fig. 5.6.

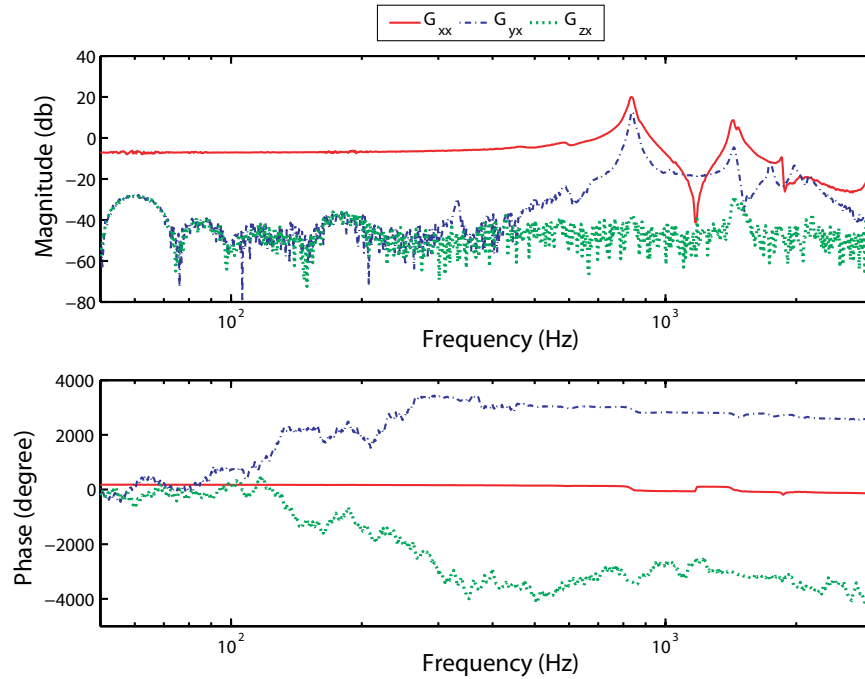


Figure 5.3: Comparison of the frequency responses of the x -axis piezo actuator dynamics and the related coupling dynamics.

Experimental results show that significant cross-axis coupling effect exists in the piezo actuators used in this experiment. The lateral to vertical x - y -to- z coupling effects were pronounced. Particularly, the gain of the x -to- z coupling dynamics in low frequency range was substantially larger (about 10 times) than the gain of other cross-axis coupling dynamics (see

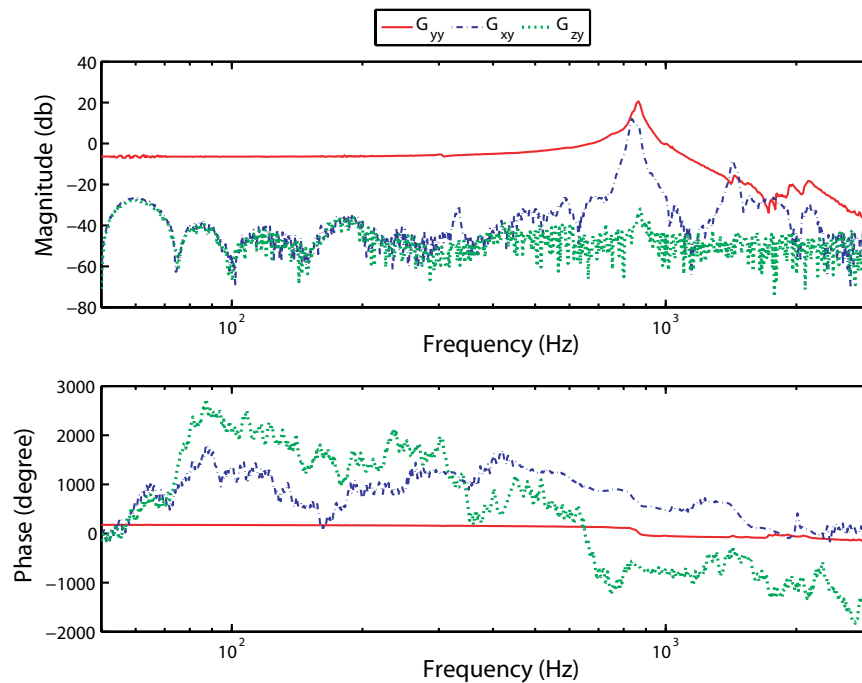


Figure 5.4: Comparison of the frequency responses of the y -axis piezo actuator dynamics and the related coupling dynamics.

Figs. 5.3 to 5.5). As a result, the lateral to vertical coupling caused displacement was expected to be more pronounced than other coupling disturbance. Such a relatively large coupling effect might be caused by the slightly misalignment of the z -axis displacement sensor. Moreover, the vertical to lateral coupling effect can be ignored, and the cross-axis coupling effects were small among all three axes in the low frequency range (for $\omega < \sim 655$ Hz). Therefore, the coupling effect can be safely ignored in usual low-speed SPM operations. In this experiment, the lateral trajectories for the desired Chinese character pattern were relatively slow compared to the coupling dynamics between x - and y -axes (i.e., the significant frequency components of the lateral trajectory were substantially lower than the resonant peaks of the lateral coupling dynamics around 800 Hz). Thus, the lateral coupling caused disturbances between x - and y -axes were expected to be small and negligible in the experiments (as verified by our experimental results). Thus, the experiment results presented next are focused on the compensation for the lateral to vertical coupling effect.

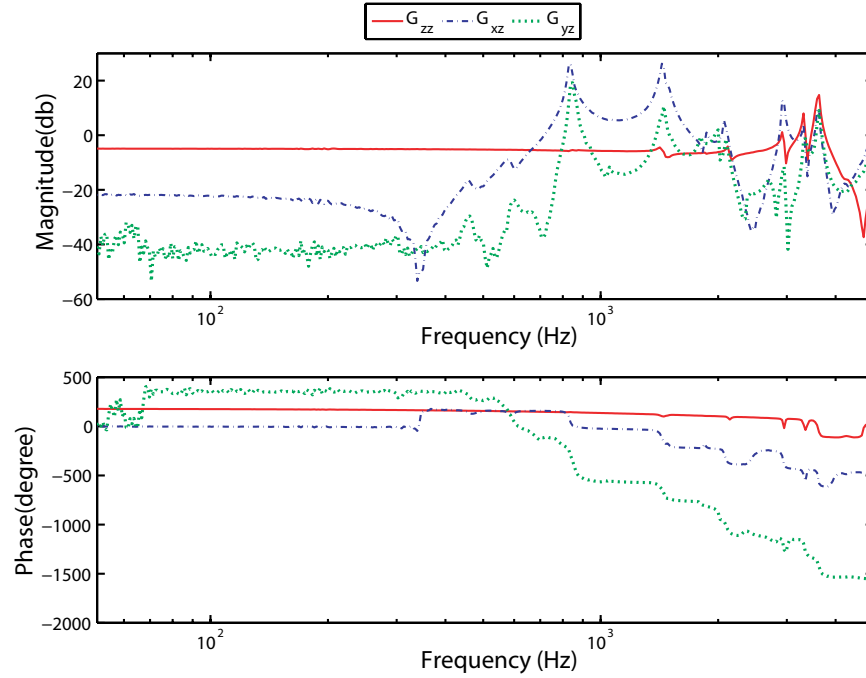


Figure 5.5: Comparison of the frequency responses of the z -axis piezo actuator dynamics and the related coupling dynamics.

5.3.3 Experimental Tracking Results and Discussion

In the experiments, the MAIIC technique was applied to achieve precision tracking in all x - y - z axes simultaneously, and then, the converged inputs were used to fabricate the pattern by applying a large load force ($\sim 22 \mu\text{N}$) to the cantilever. For comparison, we also used the DC-gain method and the MIIC method [48] to fabricate the two Chinese characters. When using the DC-gain method, the control input was generated by scaling the desired output with the DC-gain of the piezo-actuator—The DC-gain method did not account for the hysteresis, the vibration dynamics effects in each axis positioning, as well as the cross-axis coupling effects. The hysteresis and the vibration effects in each axis positioning were compensated by using the MIIC technique, where the control input for each axis was obtained by applying the MIIC technique to the tracking of each axis individually, and then then applying the control inputs of the three axes simultaneously during the fabrication process. The cross-axis dynamics coupling effect, however, was not compensated for by the MIIC technique. Therefore, the patterns fabricated by using these two methods demonstrated the above adverse effects on the fabrication quality.

The experimental tracking results by using the above three methods in all x - y - z axes were

acquired and compared. Three different fabrication rates (0.4 Hz, 1.6 Hz, and 8 Hz) were tested in the experiment, where the fabrication rate was defined as the rate to finish the fabrication of the entire pattern once. The corresponding average lateral speed for the three fabrication rates were at ~ 0.065 mm/sec, ~ 0.26 mm/sec, and ~ 1.3 mm/sec, respectively. At these three fabrication rates, the corresponding z -axis waveform frequency was around at 4, 16, and 80 Hz, respectively. In Figs. 5.7, 5.8, and 5.9, the lateral x -axis, y -axis and the vertical z -axis tracking results obtained by using the three methods are compared for the low and the high fabrication rates (0.065 mm/sec. and 1.3 mm/sec.) respectively.

The tracking performance was also evaluated by quantifying the relative RMS tracking error and the relative maximum tracking error, where the relative maximum tracking error $E_M(\%)$, and the relative RMS tracking error $E_{RMS}(\%)$ are defined as

$$\begin{aligned} E_M(\%) &\triangleq \|x_d(\cdot) - x_k(\cdot)\|_\infty \times 100, \\ E_{RMS}(\%) &\triangleq \frac{E_{RMS}}{\|x_d(\cdot)\|_2} \times 100. \end{aligned} \quad (5.17)$$

Discussion

The experimental results demonstrate that precision positioning in lateral x - y axes motion can be achieved by using the MAIIC algorithm during large-range, high-speed nanofabrication. As the lateral displacement range was large ($\sim 55 \mu\text{m}$), the hysteresis effect was pronounced, and large positioning errors were generated. As shown in Fig. 5.7 (a) and (c), with the DC-gain method, the hysteresis-caused relative maximum error $E_M(\%)$ was over 10% of the total displacement range when the fabrication rate was slow (4 Hz). Such a large positioning error was substantially reduced by using the MAIIC algorithm — the relative RMS error $E_{RMS}(\%)$ and the relative maximum error $E_M(\%)$ were reduced to 0.99% and 1.88%, respectively. As the fabrication rate was increased to 16 Hz, the vibrational dynamics effect was augmented to the hysteresis effect, resulting in even larger tracking errors. However, precision tracking was still maintained when using the MAIIC approach — $E_{RMS}(\%)$ and $E_M(\%)$ were only 1.14% and 2.30%, respectively (see Fig. 5.7 (b), (d)). Since the lateral to lateral and vertical to lateral coupling effects can be ignored, precision tracking is also obtained by using MIIC technique for x -axis. We note that for nanofabrication application, precision tracking in x and y axes are equally crucial, because even if the tracking error in each individual axis is small, a relatively

large distortion can still be generated in the final fabricated pattern. Such an “amplification” of the positioning error is caused by the superposition of the errors in different axes. In the experiment, precision tracking in y axis was also achieved by using the MAIIC technique. The simultaneous precision tracking in both x and y axes led to the precision fabrication of the continuous Chinese characters pattern.

When fabricating the Chinese characters pattern, the frequency of the isosceles trapezoidal wave was much higher (20 times higher) than that in the lateral x - y axes. As a result, large probe oscillations in the vertical z -axis not only increased the roughness of the sample surface, but can also further damaged the probe, the sample, or both. By using the MAIIC algorithm, however, even at the fabrication rate of 25 Hz, precision vertical z -axis tracking was still achieved — the $E_{RMS}(\%)$ was only 2% of that by using the MIIC method. Thus, the MAIIC algorithm can effectively account for adverse effects during high-speed, large-size nanofabrication in both lateral and vertical directions.

The experimental results also showed that coupling-caused disturbance in multi-axis motion can also be effectively removed by using the proposed method in see Sec. 5.2. Comparing z -axis tracking performance using MAIIC with using the MIIC technique (in Fig. 5.9), we can see that the x - y -to- z coupling effect was substantial. The coupling-caused z -axis displacement was $\sim 40\%$ of the (original) desired trajectory when the lateral x - y axes displacement was large ($\sim 55 \mu\text{m}$) and the velocity was at high-speed (1.3 mm/sec). Such a large coupling-caused disturbance was augmented to the vibrational dynamics effect when all 3-D inputs were applied simultaneously during the nanofabrication of the Chinese characters, resulting in much larger tracking error (than that if there were no coupling effect). This is evident by comparing with the DC-gain and the MIIC tracking results in Fig. 5.9. Large coupling-caused disturbance was eliminated by using the proposed MAIIC technique. In addition, precision tracking of the original z -axis desired trajectory was achieved during the 3-D nanofabrication. Note that in Fig. 5.9, the small oscillations at the top and the bottom of the isosceles waves were generated as the SPM cantilever needed to be pulled out and pushed onto the sample surface during the fabrication. Therefore, the experimental results demonstrate that the proposed approach can achieve high-speed precision positioning in 3-D probe-based nanofabrication at large-size.

5.3.4 Nanofabrication Results and Discussion

Next, the converged MAIIC inputs for all the x - y - z axes were applied to the x , y , and z axes respectively at the same time (the z -axis feedback control was turned off), and the Chinese characters pattern was fabricated. Then the fabricated sample area was imaged immediately afterwards on the same SPM. The SPM images of the fabricated patterns obtained by using the MAIIC technique are compared with those obtained by using the MIIC and DC-gain methods (applied to all 3-D axes) in Fig. 5.10 for the three fabrication rates (0.065 mm/s, 0.26 mm/s and 1.3 mm/s). We also examined the indentation depth through the cross-section plot shown in Fig. 5.11 — the indentation depth was ~ 20 nm.

The experimental results demonstrated the efficacy of the proposed approach in achieving 3-D precision positioning during high-speed probe-based nanofabrication. When the fabrication rate was at 0.065 mm/s, the distortions caused by nonlinear hysteresis, vibrational dynamics effects and cross-axis dynamics coupling were already pronounced. As shown in Fig. 5.10 (a2) and (a3), the Chinese characters in the pattern obtained by using the MIIC method and the DC-gain methods were curved (rather than straight) and varied in length and depth. However, such large fabrication errors in the Chinese characters were significantly reduced by using the MAIIC method: the Chinese characters were uniform in length and width, close to the desired ones (see Fig. 5.10 (a1)). When the rate was increased to 0.26 mm/s and 1.3 mm/s, the hysteresis and dynamics caused pattern distortions became much more severe. As shown in Fig. 5.10 (b2, b3, c2, c3), the Chinese characters were more curved and largely varied in length and depth. Such large pattern distortions were reduced substantially by using the proposed method. As a result, the Chinese characters patterns were close to the desired one (see Fig. 5.10 (b1), (c1)). The experimental results demonstrate that the MAIIC approach can be effectively utilized for high-speed nanofabrication of large-size 3-D patterns.

5.4 Conclusions

In this chapter, a multi-axis inversion-based iterative control (MAIIC) approach to achieve probe-based high-speed nanofabrication at large range is proposed. It was shown that the implementation of the MAIIC technique to SPM probe-based nanofabrication can effectively

compensate for the nonlinear hysteresis and vibrational dynamics effects of the piezotube actuator as well as the dynamic coupling effect, thereby improving the fabrication throughput. The approach is illustrated by implementing it to fabricate a Chinese character pattern via mechanical scratching on a gold-coated silicon sample surface. The experimental results show that Chinese character pattern of $\sim 55 \mu\text{m}$ size can be accurately fabricated at an average line speed as high as 1.3 mm/s. The experimental results demonstrated that precision position control can be achieved in high-speed large-range multi-axes nanofabrication.

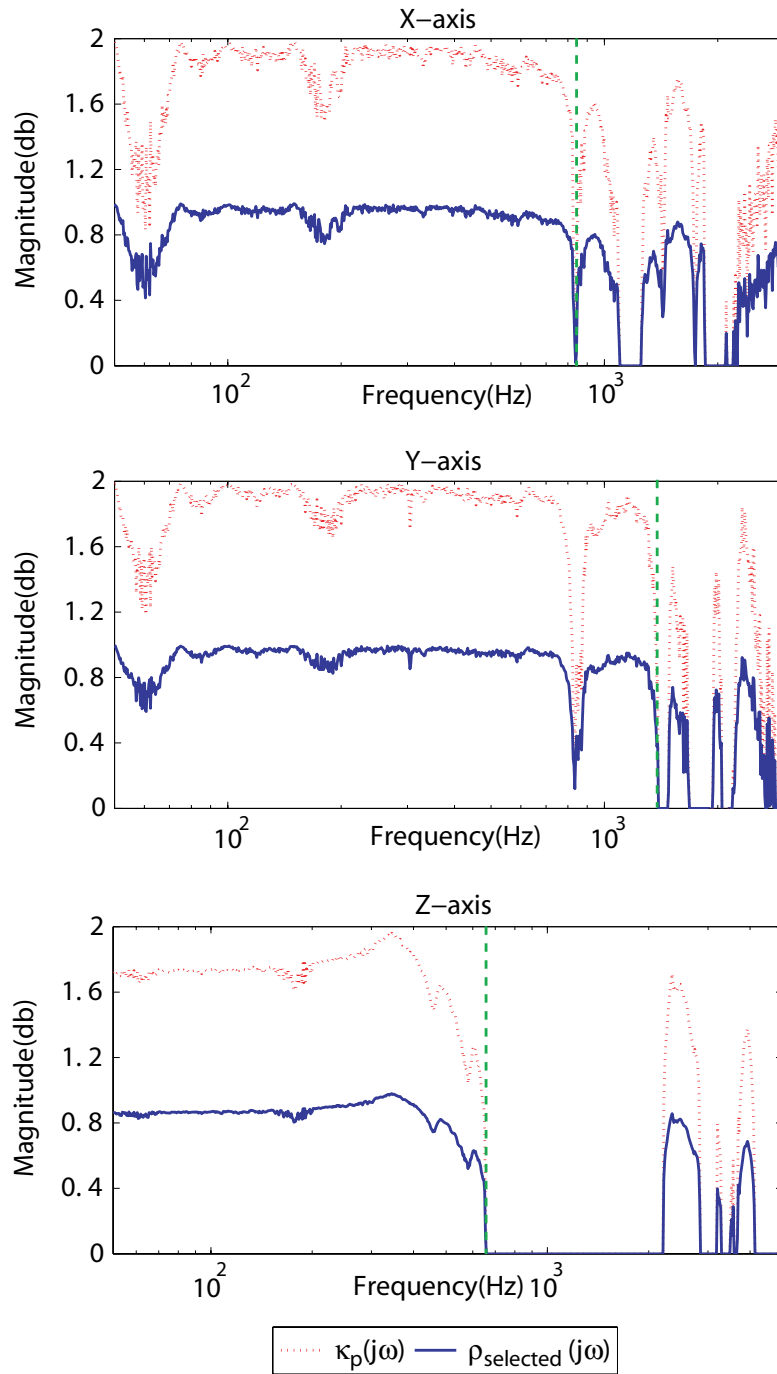


Figure 5.6: The upper bounds of the iteration coefficients $\kappa_p(j\omega)$ and the iteration coefficients $\rho_{selected}(j\omega)$ used in the experiments for x -, y - and z -axes, respectively, where the vertical green-dashed line marked the upper bound of the practically tractable set Ω_G .

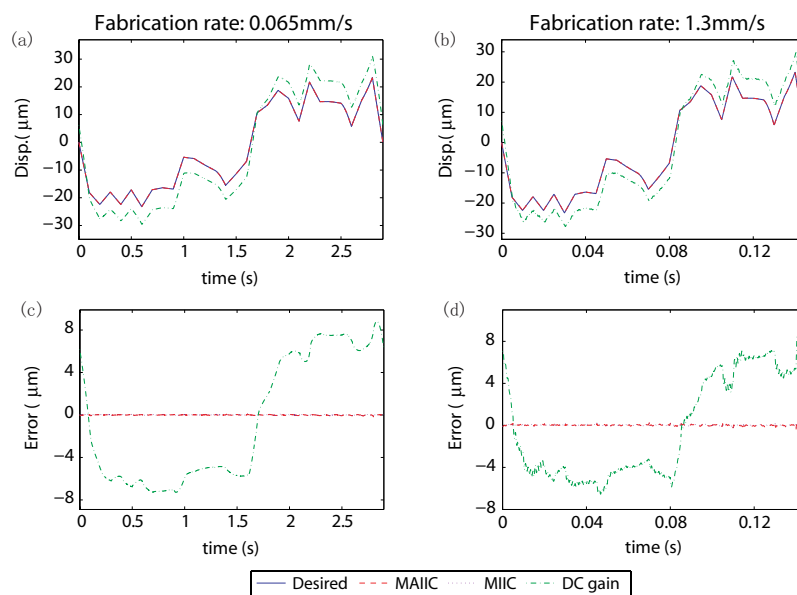


Figure 5.7: Comparison of the lateral x tracking results obtained by using the MAIIC, MIIC and DC-gain methods with the original desired trajectory at (a) low speed, (b) high speed, and comparison of the corresponding tracking errors at (c) low speed, (d) high speed, respectively.

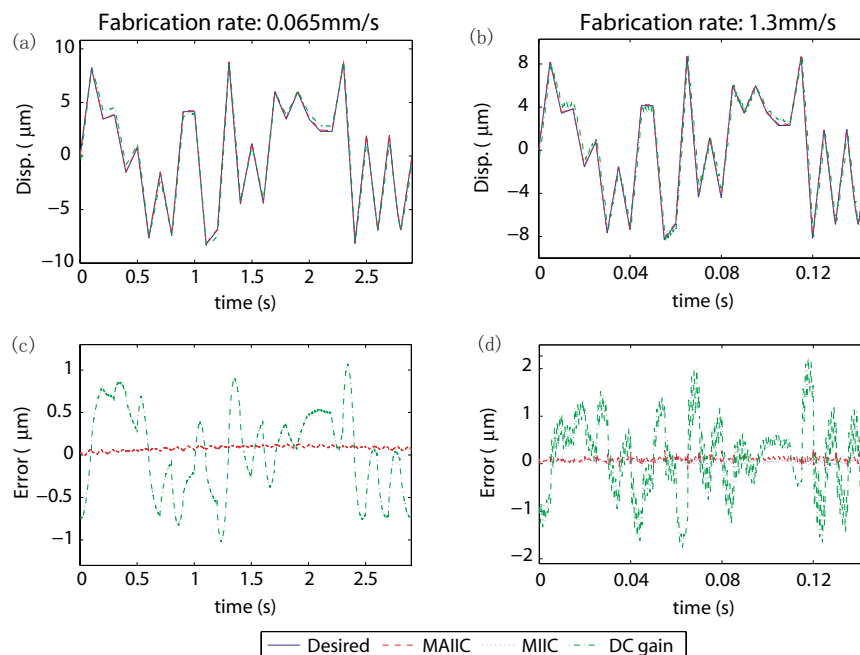


Figure 5.8: Comparison of the lateral y tracking results obtained by using the MAIIC, MIIC and DC-gain methods with the original desired trajectory at (a) low speed, (b) high speed, and comparison of the corresponding tracking errors at (c) low speed, (d) high speed, respectively.

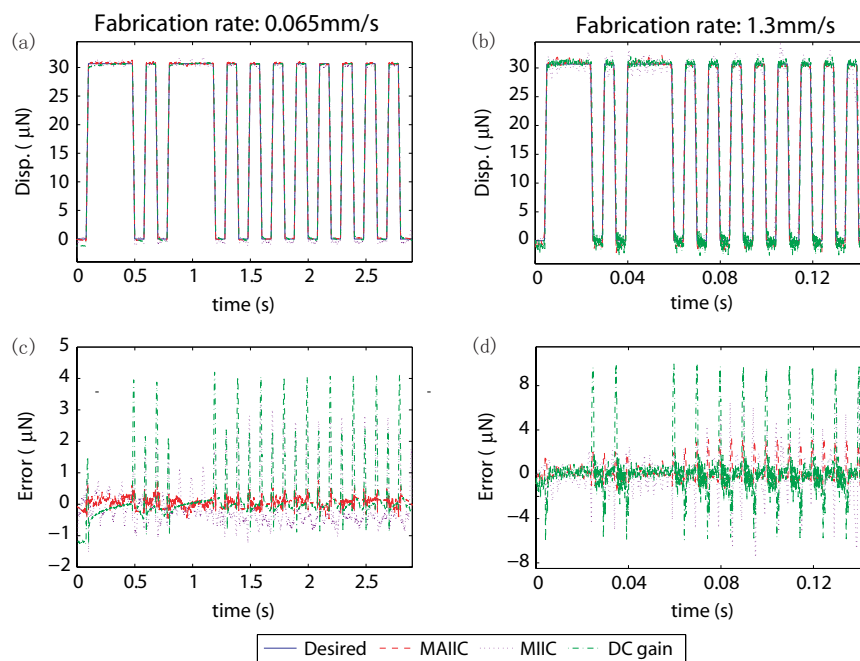


Figure 5.9: Comparison of the vertical z tracking results obtained by using the MAIIC, MIIC and DC-gain methods with the original desired trajectory at (a) low speed, (b) high speed, and comparison of the corresponding tracking errors at (c) low speed, (d) high speed, respectively

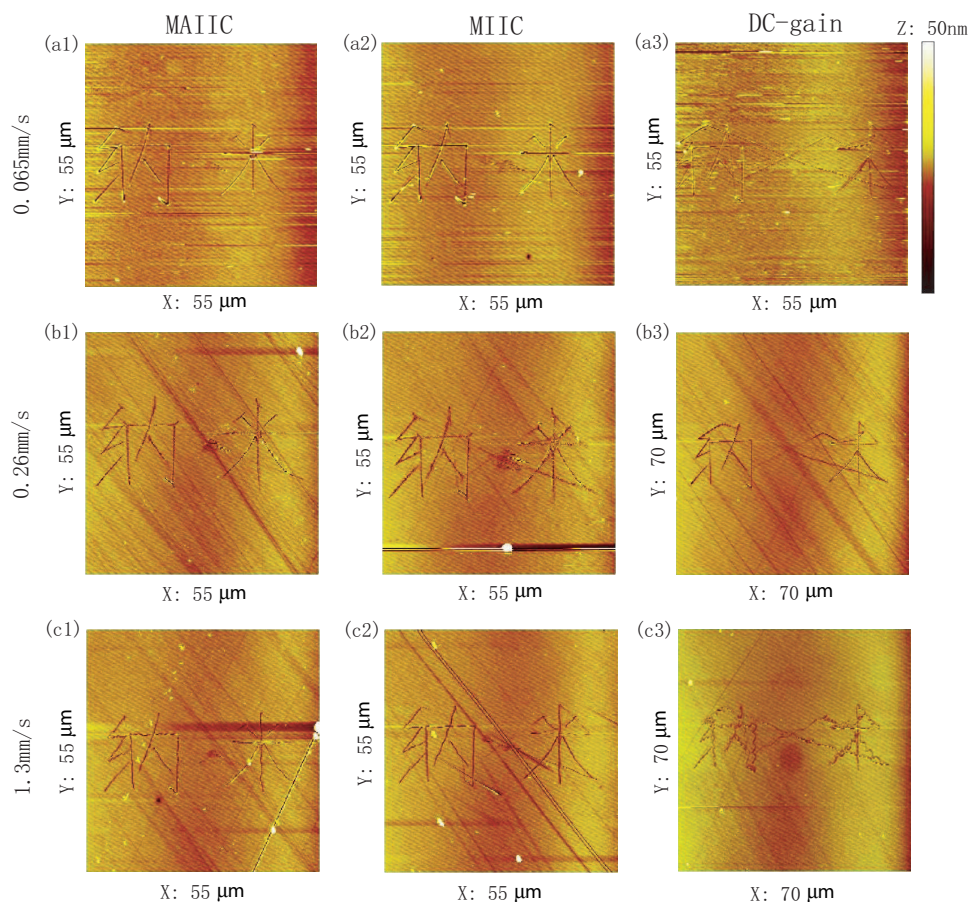


Figure 5.10: Comparison of the nanofabrication images of the Chinese characters pattern obtained by (left column) using the MAIIC technique, by (middle column) using the MIIC method, and with (right column) those obtained by using the DC-gain method at (a1, a2, a3) 0.065 mm/s, (b1, b2, b3) 0.26 mm/s, and (c1, c2, c3) 1.3 mm/s, respectively.

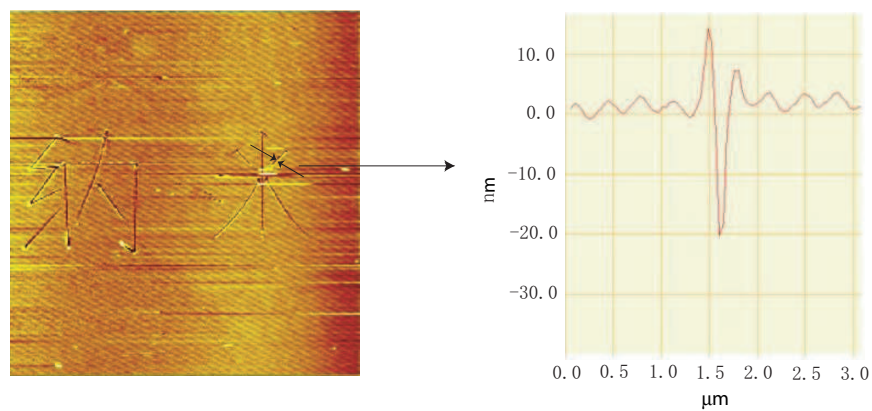


Figure 5.11: The cross section image of the Chinese characters. The right image shows the depth of the fabricated groove

Chapter 6

Conclusion

In this dissertation, a suite of inversion-based control tools have been developed for high-speed precision output tracking/transition in challenging applications in practices. The main contributions of this dissertation are as follows,

1. A preview-based optimal output tracking-transition (POOTT) control approach has been developed to achieve precision tracking in nonperiodic tracking-transition switching with preview. During the transition sections, the optimal desired output trajectory was designed by directly minimizing the output energy, and the required control input for tracking and transition sections was obtained by using a preview-based stable-inversion approach. The POOTT approach maintained the smoothness of system state across the tracking-transition switching, and minimized the output energy. Also, the required preview time has been quantified in terms of the system internal dynamics. The preview time was further minimized by incorporating with the recently-developed optimal preview-based inversion approach. The POOTT approach was demonstrated by implementing it to a nanomanipulation application using a piezoelectric actuator model in simulation.
2. A B-spline-decomposition-based (BSD) control approach to achieve precision output tracking with finite pre- and post-actuation times has been proposed. The BSD technique avoids the system dynamics uncertainties and demanding online computation by decomposing the previewed desired trajectory into a finite number of output elements based on B-splines, obtaining the corresponding desired input elements by using iterative learning control approach, and synthesizing the control input by using the corresponding input elements via the superposition principle. Furthermore, the pre-actuation and post-actuation times of the combined input for given tracking precision was quantified by

using the stable-inversion theory. The BSD control method was demonstrated and illustrated by a nanomanipulation simulation study with a nonminimum-phase piezo actuator model. Furthermore, the BSD control approach was also implemented to achieve precision tracking of online generated desired trajectory for high-speed nanomanipulation in experiments. Specifically, the BSD technique was implemented along with a PI-notch-filter feedback. The experimental results demonstrated that by using the BSD technique, the tracking precision during high-speed output tracking can be substantially improved over feedback control only, even in the presence of significant hysteresis effect. The effect of finite post-actuation time on the tracking performance was also investigated in the experiments.

3. A multi-axis inversion-based iterative control (MAIIC) approach was utilized to achieve probe-based high-speed nanofabrication at large range in SPM. The implementation of the MAIIC technique to SPM probe-based nanofabrication can effectively compensate for the nonlinear hysteresis and vibrational dynamics effects of the piezotube actuator as well as the dynamic coupling effect, thereby improving the fabrication throughput. The approach has been illustrated by implementing it to fabricate a Chinese character pattern via mechanical scratching on a gold-coated silicon sample surface. The experimental results showed that the large-range Chinese character pattern can be accurately fabricated at a high-speed. Therefore, the experimental results demonstrated that by using the MAIIC approach, precision position control can be achieved in high-speed large-range multi-axes nanofabrication.

The most promising area of future research on high-speed precision output tracking/transition based on inversion-based control tools is the study of that in the nonlinear case. Because of the large nonlinear hysteresis effect of piezotube actuators, particularly for large range displacement, future work would extend the proposed POOTT and BSD approach from linear time invariant (LTI) case to nonlinear case.

References

- [1] L. Qiu and E. J. Davison. Performance limitations of non-minimum phase systems in the servomechanism problem. *Automatica*, 29:337–349, March 1993.
- [2] J. Chen, Z. Ren, S. Hara, and L. Qiu. Optimal tracking performance: preview control and exponential signals. *IEEE Trans. on Automatic Control*, 46(10):1647–1651, 2001.
- [3] S. Devasia, D. Chen, and B. Paden. Nonlinear inversion-based output tracking. *IEEE Trans. on Automatic Control*, 41(7):930–942, 1996.
- [4] L. R. Hunt and G. Meyer. Stable inversion for nonlinear systems. *Automatica*, 33(8):1549–1554, 1997.
- [5] Q. Zou and S. Devasia. Preview-based stable-inversion for output tracking of linear systems. *ASME Journal of Dynamic Systems, Measurement and Control*, 121(1):625–630, Dec. 1999.
- [6] Q. Zou and S. Devasia. Preview-based optimal inversion for output tracking: Application to scanning tunneling microscopy. *IEEE Trans. on Control Systems Technology*, 12(3):375–386, May 2004.
- [7] Q. Zou and S. Devasia. Preview-based stable-inversion for output tracking of nonlinear nonminimum-phase systems: The VTOL example. *Automatica*, 43(1):117–127, 2007.
- [8] Q. Zou. Optimal preview-based stable-inversion for output tracking of nonminimum-phase linear systems. *Automatica*, 45:230–237, 2009.
- [9] D. Croft, G. Shedd, and S. Devasia. Creep, hysteresis, and vibration compensation for piezoactuators: Atomic force microscopy application. *ASME Journal of Dynamic Systems, Measurement and Control*, 123(1):35–43, March, 2001.
- [10] K. K. Leang and S. Devasia. Design of hysteresis-compensating iterative learning control for atomic force microscopes. *Mechatronics*, 16:141–158, 2005.
- [11] S. Tien, Q. Zou, and S. Devasia. Control of dynamics-coupling effects in piezo-actuator for high-speed AFM operation. *IEEE Trans. on Control Systems Technology*, 13(6):921–931, 2005.
- [12] H.J. Butt, B. Cappella, and M. Kappl. Force measurements with the atomic force microscope: Technique, interpretation and applications. *Surface Science Reports*, 59:1–152, 2005.
- [13] H. Numasato and M. Tomizuka. Settling control and performance of a dual-actuator system for hard-disk drives. *IEEE/ASME Transactions on Mechatronics*, 8(4):431–438, 2003.

- [14] D. Iamratanakul, B. Jordan, K. K. Leang, and S. Devasia. Optimal output transitions for dual-stage systems. *IEEE Trans. on Control Systems Technology*, 16(5):869–881, 2008.
- [15] A. Cavalcanti. Assembly automation with evolutionary nanorobots and sensor-based control applied to nanomedicine. *IEEE Trans. on Nanotechnology*, 2(2):82–87, 2003.
- [16] R. M. Murray, Z. Li, and S. S. Sastry. *A mathematical Introduction to Robotic Manipulation*. CRC Press, 1994.
- [17] S. Devasia. Should model-based inverse input be used as feedforward under plant uncertainty? *IEEE Trans. on Automatic Control*, 47(11):1865–1871, Nov. 2002.
- [18] Y. Wu and Q. Zou. Robust inversion-based 2-DOF control design for output tracking: Piezoelectric-actuator example. *IEEE Trans. on Control Systems Technology*, 17:1069–1082, 2009.
- [19] J. S. Dewey, K. K. Leang, and S. Devasia. Experimental and theoretical results in output-trajectory redesign for flexible structures. *ASME Journal of Dynamic Systems, Measurement and Control*, 120:456–461, December 1998.
- [20] G. Marro, D. Prattichizzo, and E. Zattoni. Convolution profiles for right-inversion of multivariable non-minimum phase discrete-time systems. *Automatica*, 38(10):1695–1703, 2002.
- [21] Aurelio Piazzzi and Antonio Visioli. Using stable inputoutput inversion for minimum-time feedforward constrained regulation of scalar systems. *Automatica*, 41:305–313, 2005.
- [22] T. Sogo. On the equivalence between stable inversion for nonminimum phase systems and reciprocal transfer functions defined by the two-sided laplace transform. *Automatica*, 46(1):122–126, 2010.
- [23] S. Devasia. Nonlinear minimum-time control with pre- and post-actuation. *Automatica*, 47:1379–1387, 2011.
- [24] A. Piazzzi and A. Visioli. Using stable input-output inversion for minimum-time feedforward constrained regulation of scalar systems. *Automatica*, 41(2):305–313, 2005.
- [25] K. Graichen, V. Hagenmeyer, and M. Zeitz. A new approach to inversion-based feedforward control design for nonlinear systems. *Automatica*, 41(12):2033–2041, 2005.
- [26] H. Perez and S. Devasia. Optimal output-transitions for linear system. *Automatica*, 39:181–192, 2003.
- [27] W. E. Singhose, A. K. Banerjee, and W. P. Seering. Slewing flexible spacecraft with detection-limiting input shaping. *Journal of Guidance, Control, and Dynamics*, 20(2):291–297, 1997.
- [28] M. A. Lau and L. Y. Pao. Input shaping and time-optimal control of flexible structures. *Automatica*, 39:893–900, 2003.
- [29] H. Perez, Q. Zou, and S. Devasia. Design and control of optimal scan trajectories: Scanning tunneling microscope example. *ASME Journal of Dynamic Systems, Measurement and Control*, 126(1):187–197, March 2004.

- [30] F. L. Lewis and V. L. Syrmos. *Optimal Control*. John Wiley and Sons, New York, second edition, 1995.
- [31] N. C. Singer and W. P. Seering. Preshaping command inputs to reduce system vibration. *ASME Journal of Dynamic Systems, Measurement and Control*, 112:76–82, March 1990.
- [32] L. Y. Pao. Multi-input shaping design for vibration reduction. *Automatica*, 35:81–89, 1999.
- [33] J. Vaughan, A. Yano, and W. Singhose. Comparison of robust input shapers. 315:797–815, April 1999.
- [34] K. Kim, Q. Zou, and C. Su. A new approach to scan-trajectory design and track: AFM force measurement example. *ASME Journal of Dynamic Systems, Measurement and Control*, 130:051005–1 to 051005–10, 2008.
- [35] T. C. Waite, Q. Zou, and A. Kelkar. Inversion-based feedforward approach to broadband acoustic noise reduction. In *Proceedings of American Control Conference*, pages 3795–3800, New York, NY, July 2007.
- [36] Alberto Isidori. *Nonlinear Control Systems*. Springer-Verlag, London, 3rd edition, 1995.
- [37] C. T. Chen. *Linear System Theory and Design*. Oxford University Press, 198 Madison Avenue, New York, NY 10016, New York, 3 edition, 1999.
- [38] Y. Yan, Q. Zou, and Z. Lin. A control approach to high-speed probe-based nanofabrication. *Nanotechnology*, 20(17):175301, April 2009.
- [39] W. Rudin. *Real and Complex Analysis*. McGraw-Hill, New York, third edition, 1966.
- [40] J. Lefebvre, J. F. Lynch, M. Llaguno, M. Radosavljevic, and A. T. Johnson. Single-wall carbon nanotube circuits assembled with an atomic force microscope. *Applied Physics Letters*, 75(19):844–849, August 1999.
- [41] J. Brufau, M. Puig-Vidal, J. Lopez-Sanchez, and J. Samitier. Micron: Small autonomous robot for cell manipulation applications. *IEEE Journal of Robotics and Automation*, pages 844–849, April 2005.
- [42] Y. Wu and Q. Zou. Robust inversion-based 2-dof control design for output tracking: Piezoelectric-actuator example. *IEEE Trans. on Control Systems Technology*, 17(5):1069–1082, September 2009.
- [43] G. Marro and E. Zattoni. h_2 -optimal rejection with preview in the continuous-time domain. *Automatica*, 41(5):815–821, 2005.
- [44] A. Cohen and U. Shaked. Linear discrete-time h_∞ -optimal tracking with preview. *Automatic Control, IEEE Transactions on*, 42(2):270–276, 1997.
- [45] D. N. Hoover, R. Longchamp, and J. Rosenthal. Two-degree-of-freedom l_2 -optimal tracking with preview. *Automatica*, 40(1):155–162, 2004.
- [46] M.E. Halpern. Preview tracking for discrete-time siso systems. *IEEE Trans. on Automatic Control*, 39(3):589–592, 1994.

- [47] K. L. Moore and J.-X. Xu. Special issue on iterative learning control. *International Journal of Control*, 73(10):819–823, 2000.
- [48] K.-S. Kim and Q. Zou. A model-less inversion-based iterative control technique for output tracking: Piezo actuator example. In *Proceedings of American Control Conference*, pages 2710–2715, Seattle, WA, June 2008.
- [49] K. Takayama and H. Kano. A new approach to synthesizing free motions of robotic manipulators based on a concept of unit motions. *IEEE Trans. on Systems, Man, and Cybernetics-Part C: Applications and Reviews*, 25(3):453–463, March 1995.
- [50] D. J. Hoelzle, A. G. Alleyne, and A. J. W. Johnson. Basis task approach to iterative learning control with applications to micro-robotic deposition. *IEEE Trans. on Control Systems Technology*, 19(5):1138–1148, September 2011.
- [51] M.J.D.Powell. *Approximation Theory and Methods*. Cambridge University Press, 1981.
- [52] A. Ude, C.G. Atkeson, and M. Riley. Planning of joint trajectories for humanoid robots using b-spline wavelets. In *IEEE Journal of Robotics and Automation*, pages 2223–2228, San Francisco, CA, USA, April, 2000.
- [53] H. Kano, M. Egerstedt, H. Nakata, and C. F. Martin. B-splines and control theory. *Applied Mathematics and Computation*, 145:263–288, 2003.
- [54] G. Basset, Y. Xu, and N. Li. Fast trajectory planning via the b-spline augmented virtual motion camouflage approach. In *IEEE conference on Decision and Control*, pages 273–277, Orlando, FL, USA, December 2011.
- [55] H. Kano, H. Nakata, and C. F. Martin. Optimal curve fitting and smoothing using normalized uniform b-splines: a tool for study complex systems. *Applied Mathematics and Computation*, 169:96–128, 2005.
- [56] Y. Yan, H. Wang, and Q. Zou. A decoupled inversion-based iterative control approach to multi-axis precision positioning: 3-d nanopositioning example. *Automatica*, 48(1):167176, January 2012.
- [57] D. A. Bristow, A. G. Alleyne, and M. Tharayil. Optimizing learning convergence speed and converged error for precision motion control. *ASME Journal of Dynamic Systems, Measurement and Control*, 130(5), December 2008.
- [58] Z. Sun and T.-C. Tsao. Process feedback control of the noncircular turning process for camshaft machining. *ASME Journal of Dynamic Systems, Measurement and Control*, 130(3), May. 2008.
- [59] H. Wang, K. Kim, and Q. Zou. B-spline-decomposition-based output tracking with preview for nonminimum-phase linear systems. *Automatica*, March 2013. In Press.
- [60] G. M. Clayton, S. Tien, K. K. Leang, Q. Zou, and S. Devasia. A review of feedforward control approaches in nanopositioning for high-speed spm. 131(6):61101, November 2009.
- [61] A. Sebastian and S. Salapaka. Design methodologies for robust nano-positioning. *IEEE Trans. on Control Systems Technology*, 13(6):868–876, 2005.

- [62] S. Devasia, E. Eleftheriou, and S. O. R. Moheimani. A survey of control issues in nanopositioning. *IEEE Trans. on Control Systems Technology*, 15:802–823, 2007.
- [63] C. Rotsch, K. Jacobson, and M. Radmacher. Dimensional and mechanical dynamics of active and stable edges in motile fibroblasts investigated by using atomic force microscopy. *Proc. Natl. Acad. Sci. USA*, 96:921–926, February 1999.
- [64] Y. Wu and Q. Zou. Iterative control approach to compensate for both the hysteresis and the dynamics effects of piezo actuators. *IEEE Trans. on Control Systems Technology*, 15:936–944, 2007.
- [65] C. Lee and S. M. Salapaka. Robust broadband nanopositioning: fundamental trade-offs, analysis, and design in a two-degree-of-freedom control framework. *Nanotechnology*, 20(3), 2009.
- [66] A. J. Fleming and K. K. Leang. Integrated strain and force feedback for high-performance control of piezoelectric actuators. 161:256–265, June 2010.
- [67] Y. Li and Q. Xu. Adaptive sliding mode control with perturbation estimation and pid sliding surface for motion tracking of a piezo-driven micromanipulator. *IEEE Trans. on Control Systems Technology*, 18(4):798–810, July 2010.
- [68] A. Bazaei, Y.K. Yong, S.O.R. Moheimani, and A. Sebastian. Tracking of triangular references using signal transformation for control of a novel afm scanner stage. *IEEE Trans. on Control Systems Technology*, 20(2):453–464, March 2012.
- [69] G. Schitter, P. Menold, H.F. Knapp, F. Allgower, and A. Stemmer. High performance feedback for fast scanning atomic force microscopes. *Review of Scientific Instruments*, 72(8):3320–3327, 2001.
- [70] K. Kim and Q. Zou. A modeling-free inversion-based iterative feedforward control for precision output tracking of linear time-invariant systems. *IEEE/ASME Transactions on Mechatronics*, pages 1–11, 2012.
- [71] D. A. Bristow and A. G. Alleyne. Monotonic convergence of iterative learning control for uncertain systems using a time-varying filter. *IEEE Trans. on Automatic Control*, 53(2):582–585, 2008.
- [72] A. A. Tseng, A. Notargiacomo, and T. P. Chen. Nanofabrication by scanning probe microscope lithography: A review. *Journal of Vacuum Science and Technology:B*, 23(3):877–894, 2005.
- [73] B. D. Gates, Q. Xu, M. S., D. Ryan, C. G. Willson, and G. M. Whitesides. New approaches to nanofabrication: Molding, printing, and other techniques. *Chemical Reviews*, 105(4):1171–1196, 2005.
- [74] X. Xie, H. Chung, C. Sow, and A. Wee. Nanoscale materials patterning and engineering by atomic force microscopy nanolithography. *Chemical Reviews*, 54:1–48, 2006.
- [75] D. Abramovitch, S. Andersson, L. Pao, and G. Schitter. A tutorial on the control of atomic force microscope. In *Proceedings of American Control Conference*, pages 3499–3502, New York City, NY, July 2007.

- [76] S. O. Reza Moheimani. Invited review article: Accurate and fast nanopositioning with piezoelectric tube scanners: Emerging trends and future challenges. *Review of Scientific Instruments*, 79(7):071101, 2008.
- [77] Y. Wu, J. Shi, C. Su, and Q. Zou. A control approach to cross-coupling compensation of piezotube scanners in tapping-mode atomic force microscope imaging. *Review of Scientific Instruments*, 80(4):043709, 2009.
- [78] Y. Yan, Q. Zou, and Z. Lin. A control approach to high-speed probe-based nanofabrication. *Nanotechnology*, 20(17), April 2009.
- [79] R. Magno and B. R. Bennett. Nanostructure patterns written in iii-v semiconductors by an atomic force microscope. *Applied Physics Letters*, 70(14), May 1997.
- [80] J Michler, R Gassilloud, P Gasser, L Santinacci, and P Schmukib. Defect-free afm scratching at the si/sio₂ interface used for selective electrodeposition of nanowires. 7(3):A41–A43, January 2004.
- [81] P. Vettiger, G. Cross, M. Despont, U. Drechsler, U. Durig, B. Gotsmann, W. Haberle, M.A. Lantz, H.E. Rothuizen, R. Stutz, and G.K. Binnig. The “millipede” - nanotechnology entering data storage. *IEEE Trans. on Nanotechnology*, 1(1):39–55, 2002.
- [82] N. J. Curson, R. Nemetudi, N. J. Appleyard, M. Pepper, D. A. Ritchie, and G. A. C Jones. Ballistic transport in a gaas/al_xga_{1-x}as one-dimensional channel fabricated using an atomic force microscope. *Applied Physics Letters*, 78(22), May 2001.
- [83] A. Chimmalgi, C. P. Grigoropoulos, and K. Komvopoulos. Surface nanostructuring by nano-/femtosecond laser-assisted scanning force microscopy. *Journal of Applied Physics*, 97(10):104319, May 2005.
- [84] R. D. Piner, J. Zhu, F. Xu, S. Hong, and C. A. Mirkin. “dip-pen” nanolithography. *Science*, 283:661–663, January 1999.
- [85] B. E. Helfrich, C. Lee, D. A. Bristow, X. H. Xiao, J. Dong, A. G. Alleyne, S. M. Salapaka, and P. M. Ferreira. Combined h_∞ -feedback control and iterative learning control design with application to nanopositioning systems. *IEEE Trans. on Control Systems Technology*, 18(2):336–351, 2010.
- [86] J. Dong, S. M. Salapaka, and P. M. Ferreira. Robust control of a parallel-kinematic nanopositioner. *ASME Journal of Dynamic Systems, Measurement and Control*, 130(4), 2008.
- [87] S. Skogestad and I. Postlethwaite. *Multivariable Feedback control: Analysis and Design*. Wiley, New York, second edition, 2005.